

**ISTANBUL TECHNICAL UNIVERSITY ★ GRADUATE SCHOOL OF SCIENCE**  
**ENGINEERING AND TECHNOLOGY**

**MAGNESIUM BASED HYDROGEN STORAGE MATERIALS**

**M.Sc. THESIS**

**Merve ILIKSU**

**Department of Chemical Engineering**

**Chemical Engineering Programme**

**Anabilim Dalı : Herhangi Mühendislik, Bilim**

**Programı : Herhangi Program**

**JUNE 2012**



**ISTANBUL TECHNICAL UNIVERSITY ★ GRADUATE SCHOOL OF SCIENCE**  
**ENGINEERING AND TECHNOLOGY**

**MAGNESIUM BASED HYDROGEN STORAGE MATERIALS**

**M.Sc. THESIS**

**Merve ILIKSU**  
**(506101021)**

**Department of Chemical Engineering**

**Chemical Engineering Programme**

**Thesis Advisor: Prof. Dr. Reha YAVUZ**  
**Anabilim Dalı : Herhangi Mühendislik, Bilim**  
**Programı : Herhangi Program**

**JUNE 2012**



**İSTANBUL TEKNİK ÜNİVERSİTESİ ★ FEN BİLİMLERİ ENSTİTÜSÜ**

**MAGNEZYUM ESASLI HİDROJEN DEPOLAMA MALZEMELERİ**

**YÜKSEK LİSANS TEZİ**

**Merve ILIKSU  
(506101021)**

**Kimya Mühendisliği Anabilim Dalı**

**Kimya Mühendisliği Programı**

**Tez Danışmanı: Prof. Dr. Reha YAVUZ  
Anabilim Dalı : Herhangi Mühendislik, Bilim  
Programı : Herhangi Program**

**HAZİRAN 2012**



Merve ILIKSU, a M.Sc. student of ITU Graduate School of Science Engineering and Technology student ID 506101021, successfully defended the thesis entitled “MAGNESIUM BASED HYDROGEN STORAGE MATERIALS”, which she prepared after fulfilling the requirements specified in the associated legislations, before the jury whose signatures are below.

**Thesis Advisor :**      **Prof. Dr. Reha YAVUZ** .....  
İstanbul Technical University

**Jury Members:**      **Prof.Dr. Hale GÜRBÜZ** .....  
İstanbul Technical University

**Prof. Dr. İ. Servet TİMUR** .....  
İstanbul Technical University

**Date of Submission : 03 May 2012**  
**Date of Defense :     08 June 2012**





*To my family,*



## **FOREWORD**

This work concerns itself with the preparation and characterisation of magnesium based hydrogen storage materials.

I would like to thank my supervisor Professor Reha Yavuz for his guidance and advice and encouraging me to go abroad and participate in an ERASMUS collaboration.

Furthermore I would like to thank my Professor Peter Notten for providing valuable insights into specific aspects of the topic.

Also I would like to thank Thiru for his support of experimental study.

Finally, this work would not exist without the continuous support of my family, they always believe in me.

March 2012

Merve ILIKSU  
(Chemical Engineer)



## TABLE OF CONTENTS

	<u>Page</u>
<b>FOREWORD</b> .....	<b>ix</b>
<b>TABLE OF CONTENTS</b> .....	<b>xi</b>
<b>ABBREVIATIONS</b> .....	<b>xiii</b>
<b>LIST OF TABLES</b> .....	<b>xv</b>
<b>LIST OF FIGURES</b> .....	<b>xvii</b>
<b>1 INTRODUCTION</b> .....	<b>1</b>
1.1 The Hydrogen Economy .....	1
1.2 Other Applications of Metal Hydrides .....	5
1.2.1 Rechargeable batteries .....	5
1.2.2 Gas purification and (isotope) separation & reversible gettering .....	7
1.2.3 Electrochromic windows and hydrogen sensors .....	7
1.3 Scope .....	8
<b>2 MECHANICAL ALLOYING</b> .....	<b>9</b>
2.1 Mechanism of Alloying .....	9
2.1.1 Ductile-ductile components .....	11
2.1.2 Ductile-brittle components .....	12
2.1.3 Brittle-brittle components .....	13
2.2 The Process of Mechanical Alloying .....	15
2.2.1 Raw materials .....	15
2.2.2 Types of mills .....	16
2.2.2.1 SPEX shaker mills .....	16
2.2.2.2 Planetary ball mills .....	17
2.2.2.3 Attritor mills .....	18
2.3 Process Variables .....	19
2.3.1 Type of mill .....	20
2.3.2 Milling container .....	20
2.3.3 Milling speed .....	21
2.3.4 Milling time .....	21
2.3.5 Grinding medium .....	22
2.3.6 Ball-to-powder weight ratio .....	23
2.3.7 Extent of filling the vial .....	24
2.3.8 Milling atmosphere .....	24
2.3.9 Process control agents .....	25
2.3.10 Temperature of milling .....	27
<b>3 ELECTROCHEMICAL HYDROGEN STORAGE</b> .....	<b>29</b>
3.1 Electrochemical Hydrogen Storage .....	29
3.1.1 Relevant reactions .....	29
3.2 Constant-Current (CC) measurements .....	30
3.3 Galvanostatic Intermittent Titration Technique (GITT) .....	32
3.4 Electrochemical Impedance Spectroscopy (EIS) .....	34

<b>4</b>	<b>Mg BASED HYDROGEN STORAGE MATERIALS .....</b>	<b>39</b>
4.1	Existing AB <sub>5</sub> .....	39
4.2	Magnesium Based Binary Alloys.....	40
4.2.1	Magnesium Scandium alloys .....	42
4.2.2	Magnesium Titanium alloys.....	46
4.2.3	Mg-based ternary alloys .....	51
<b>5</b>	<b>EXPERIMENTAL WORK.....</b>	<b>53</b>
5.1	Alloy and Electrode Preparation and Characterisation .....	53
<b>6</b>	<b>RESULTS AND DISCUSSION.....</b>	<b>57</b>
6.1	Results .....	57
6.2	Comparisons of the Alloys with Their Hydrogen Storage Performance ...	82
<b>7</b>	<b>CONCLUSIONS AND RECOMMENDATIONS FOR FUTURE RESEARCH.....</b>	<b>95</b>
	<b>REFERENCES.....</b>	<b>99</b>

## **ABBREVIATIONS**

<b>MH</b>	: Metal hydride
<b>MA</b>	: Mechanical alloying
<b>ODS</b>	: oxide-dispersion strengthened
<b>dMA</b>	: double Mechanical alloying
<b>BPR</b>	: Ball-to-powder ratio
<b>CR</b>	: Charge ratio
<b>PCA</b>	: Process control agent
<b>CC</b>	: Constant Current
<b>GITT</b>	: Galvanostatic Intermittent Titration Technique
<b>SHE</b>	: Standard hydrogen electrode
<b>EIS</b>	: Electrochemical Impedance Spectroscopy
<b>TM</b>	: Transition metal
<b>XRD</b>	: X-ray diffraction
<b>HCP</b>	: Hexagonal closed packed
<b>FCC</b>	: Face centered cubic
<b>SEM</b>	: Scanning electron microscope
<b>at</b>	: Atomic
<b>wt</b>	: Weight
<b>HER</b>	: Hydrogen evolution reaction
<b>Rms</b>	: Root mean square
<b>WE</b>	: Working electrode
<b>RE</b>	: Reference electrode





**LIST OF TABLES**

	<b><u>Page</u></b>
<b>Table 1.1:</b> U.S. Department of Energy Technical Targets: On-Board Hydrogen Storage Systems. ....	3
<b>Table 2.1:</b> Typical capacities of the different types of mills.....	20



## LIST OF FIGURES

	<u>Page</u>
<b>Figure 1.1:</b> Fossil fuel reserves-to-production ratios at the end of 2006. ....	1
<b>Figure 1.2:</b> Periodic table of elements with per element the most common hydrides and corresponding gravimetric capacity in wt.% H. ....	4
<b>Figure 1.3:</b> Schematic overview of the chemistry of a rechargeable NiMH battery ..	5
<b>Figure 2.1:</b> Ball-powder-ball collision of powder mixture during mechanical alloying.....	10
<b>Figure 2.2:</b> Refinement of particle and grain sizes with milling time.....	11
<b>Figure 2.3:</b> Scanning electron micrograph depicting the convoluted lamellar structure obtained during milling of a ductile-ductile component system (Ag-Cu).....	12
<b>Figure 2.4:</b> Schematics of microstructural evolution during milling of a ductile-brittle combination of powders. ....	13
<b>Figure 2.5:</b> Scanning electron micrograph of the Si-Ge powder mix for 12 h. ....	14
<b>Figure 2.6:</b> Process flowsheet and the microstructures developed during double mechanical alloying (dMA) of an Al-5wt.% Fe-4wt.% Mn powder mixture....	16
<b>Figure 2.7:</b> (a) SPEX 8000 mixer/mill in the assembled condition. (b) Tungsten carbide vial set consisting of the vial, lid, gasket, and balls. ....	17
<b>Figure 2.8:</b> (a) Fritsch Pulverisette P-5 four station ball mill. (b) Schematic depicting the ball motion inside the ball mill.....	18
<b>Figure 2.9:</b> (a) Model 1-S attritor. (b) Arrangement of rotating arms on a shaft in the attrition ball mill.....	19
<b>Figure 3.1:</b> Schematic drawing of a planar MH electrode. ....	29
<b>Figure 3.2:</b> Schematic overview of the electrochemical experimental setup.....	31
<b>Figure 3.3:</b> An applied constant current starting at $t = 0$ (left) and a possible potential response of the working electrode during charge (right) .....	31
<b>Figure 3.4:</b> Alternately applied current pulses and resting periods (left) and the possible potential response of the working electrode (right) during a GITT measurement. ....	33
<b>Figure 3.5:</b> Equivalent circuit representing an electrode immersed in an electrolyte where a reaction takes place at the electrode/electrolyte interface and the resulting Nyquist plot.....	36
<b>Figure 3.6:</b> The Randles equivalent circuit and a typical Nyquist plot showing the Warburg impedance. ....	37
<b>Figure 4.1:</b> Rutile $\text{MgH}_2$ (a) and fluorite $\text{Mg}_x\text{TM}_{(1-x)}\text{H}_2$ .....	40
<b>Figure 4.2:</b> Comparison between (a) $\text{AB}_5$ type compound and (b) $\text{Mg}_{72}\text{Sc}_{28}(\text{Pd}_{0.012}\text{Rh}_{0.012})$ . ....	41
<b>Figure 4.3:</b> Galvanostatic discharge curves of: thin films (a) and bulk materials (b); the current density was 1000 mA/g for the thin films and 50 mA/g for the bulk materials [5]. ....	43

<b>Figure 4.4:</b> Neutron diffraction of $\text{Mg}_{65}\text{Sc}_{35}$ (a) before deuterium loading (b) after deuterium loading.....	44
<b>Figure 4.5:</b> Relaxation map showing rate $\omega H$ of H hopping as a function of reciprocal temperature in $\text{MgH}_2$ , $\text{ScH}_2$ , $\text{MgScH}_x$ , and $\text{LaNi}_5\text{H}_{6.8}$ .....	45
<b>Figure 4.6:</b> Enthalpies of formation of $\text{Mg}_{1-y}\text{Sc}_y\text{H}_2$ . (a) Rutile (b) fluorite.....	46
<b>Figure 4.7:</b> Electrochemical determined reversible electrochemical capacity at room temperature as function of magnesium content in Mg-Ti thin film electrodes..	47
<b>Figure 4.8:</b> In-situ electrochemical XRD measurements of $\text{Mg}_{0.90}\text{Ti}_{0.10}$ (a) and $\text{Mg}_{0.70}\text{Ti}_{0.30}$ (b) during hydrogenation [130].....	50
<b>Figure 4.9:</b> Electrochemically determined dehydrogenation isotherms of 200 nm; (top a) $\text{Mg}_{0.69}\text{Ti}_{0.21}\text{Al}_{0.10}$ and (top b) $\text{Mg}_{0.80}\text{Ti}_{0.20}$ thin films with a 10 nm Pd top-coat (bottom a) $\text{Mg}_{0.55}\text{Ti}_{0.35}\text{Si}_{0.10}$ and (bottom b) $\text{Mg}_{0.69}\text{Ti}_{0.21}\text{Si}_{0.10}$ films capped with 10 nm Pd [140]......	52
<b>Figure 5.1:</b> A Spex 8000M shaker mill.....	54
<b>Figure 5.2:</b> The experimental setup used for electrochemical measurements .....	55
<b>Figure 6.1:</b> XRD patterns of $\text{Mg}_{0.70}\text{Ti}_{0.30}$ ( $\Delta$ indicates Mg, O indicates Ti).....	57
<b>Figure 6.2:</b> SEM micrographs of $\text{Mg}_{0.70}\text{Ti}_{0.30}$ milled for 28 hours.....	58
<b>Figure 6.3:</b> The electrochemical measurements of the $\text{Mg}_{0.70}\text{Ti}_{0.30}$ alloy. ....	59
<b>Figure 6.4:</b> XRD patterns of $(\text{Mg}_{70}\text{Ti}_{30})_{0.90}\text{Ni}_{10}$ ( $\Delta$ represent Mg and $\Theta$ present Ni) ..	61
<b>Figure 6.5:</b> SEM micrographs of $(\text{Mg}_{0.70}\text{Ti}_{0.30})_{0.90}\text{Ni}_{0.10}$ .....	61
<b>Figure 6.6:</b> The electrochemical charging and discharging graph of the $(\text{Mg}_{70}\text{Ti}_{30})_{0.90}\text{Ni}_{10}$ alloy.....	62
<b>Figure 6.7:</b> XRD patterns of $(\text{Mg}_{0.70}\text{Ti}_{0.30})_{0.90}\text{Ni}_{0.10}$ simultaneously ( $\Delta$ represent Mg, $\Theta$ present Ni and O present Ti) .....	63
<b>Figure 6.8:</b> The electrochemical charging and discharging graph of the $(\text{Mg}_{0.70}\text{Ti}_{0.30})_{0.90}\text{Ni}_{0.10}$ simultaneously alloy. ....	64
<b>Figure 6.9:</b> XRD pattern of $(\text{Mg}_{0.70}\text{Ti}_{0.30})_{0.80}\text{Ni}_{0.20}$ ( $\Delta$ represent Mg and $\Theta$ present Ni) .....	65
<b>Figure 6.10:</b> The electrochemical charging and discharging graph of the $(\text{Mg}_{70}\text{Ti}_{30})_{0.80}\text{Ni}_{20}$ alloy.....	66
<b>Figure 6.11:</b> XRD patterns of $(\text{Mg}_{0.65}\text{Ti}_{0.35})_{0.90}\text{Ni}_{0.10}$ ( $\Delta$ represent Mg).....	67
<b>Figure 6.12:</b> The electrochemical charging and discharging graph of the $(\text{Mg}_{0.65}\text{Ti}_{0.35})_{0.90}\text{Ni}_{0.10}$ alloy.....	68
<b>Figure 6.13:</b> XRD patterns of $\text{Mg}_2\text{Ni}$ ( $\Delta$ represent Mg, $\Theta$ present Ni and $\diamond$ $\text{Mg}_2\text{Ni}$ ) ..	69
<b>Figure 6.14:</b> SEM micrographs of $\text{Mg}_2\text{Ni}$ .....	70
<b>Figure 6.15:</b> The SEM micrograph of $\text{Mg}_2\text{Ni}$ after 4 (a) and 10 (b) hours of milling. ....	71
<b>Figure 6.16:</b> The electrochemical charging and discharging graph of the $\text{Mg}_2\text{Ni}$ alloy.....	72
<b>Figure 6.17:</b> XRD patterns of $\text{Mg}_2\text{Ni}$ and $(\text{Mg}_2\text{Ni})_{0.90}\text{Ti}_{0.10}$ .....	73
<b>Figure 6.18:</b> SEM micrograph of $(\text{Mg}_2\text{Ni})_{0.90}\text{Ti}_{0.10}$ .....	73
<b>Figure 6.19:</b> The electrochemical charging and discharging graph of the $(\text{Mg}_2\text{Ni})_{0.90}\text{Ti}_{0.10}$ alloy.....	74
<b>Figure 6.20:</b> XRD patterns of $(\text{Mg}_2\text{Ni})_{0.80}\text{Ti}_{0.20}$ .....	75
<b>Figure 6.21:</b> SEM micrographs of $(\text{Mg}_2\text{Ni})_{0.80}\text{Ti}_{0.20}$ .....	75
<b>Figure 6.22:</b> The electrochemical charging and discharging graph of the $(\text{Mg}_2\text{Ni})_{0.80}\text{Ti}_{0.20}$ alloy.....	76
<b>Figure 6.23:</b> XRD patterns of $\text{Mg}_{0.70}\text{Ti}_{0.30}$ and $(\text{Mg}_{0.70}\text{Ti}_{0.30})_{0.90}\text{Si}_{0.10}$ .....	77

<b>Figure 6.24:</b> XRD patterns of samples of: (a) mechanically alloyed $\text{Mg}_{0.60}\text{Ti}_{0.10}\text{Si}_{0.30}$ and $\text{Mg}_{0.88}\text{Ti}_{0.05}\text{Si}_{0.07}$ ; (b) heat-treated (i) $\text{Mg}_{0.60}\text{Ti}_{0.10}\text{Si}_{0.30}$ and (ii) $\text{Mg}_{0.88}\text{Ti}_{0.05}\text{Si}_{0.07}$ [143].....	78
<b>Figure 6.25:</b> SEM micrographs of $(\text{Mg}_{0.70}\text{Ti}_{0.30})_{0.90}\text{Si}_{0.10}$ .....	79
<b>Figure 6.26:</b> The electrochemical charging and discharging graph of the $(\text{Mg}_2\text{Ni})_{0.90}\text{Si}_{0.10}$ alloy. ....	79
<b>Figure 6.27:</b> XRD patterns of $\text{Mg}_2\text{Si}$ .....	80
<b>Figure 6.28:</b> SEM micrographs for $\text{Mg}_2\text{Si}$ .....	81
<b>Figure 6.29:</b> SEM micrograph of a general view of mechanically alloyed $\text{Mg}_2\text{Si}$ powder (23 hr alloyed) .....	81
<b>Figure 6.30:</b> The electrochemical charging and discharging graph of the $\text{Mg}_2\text{Si}$ alloy.....	82
<b>Figure 6.31:</b> The electrochemical charging and discharging graph of the $\text{Mg}_{0.70}\text{Ti}_{0.30}$ is compared with $(\text{Mg}_{0.70}\text{Ti}_{0.30})_{0.90}\text{Ni}_{0.10}$ and $(\text{Mg}_{0.70}\text{Ti}_{0.30})_{0.80}\text{Ni}_{0.20}$ alloy. ....	83
<b>Figure 6.32:</b> The electrochemical charging and discharging graph of the $\text{Mg}_{0.70}\text{Ti}_{0.30}$ is compared with $(\text{Mg}_{0.70}\text{Ti}_{0.30})_{0.90}\text{Si}_{0.10}$ alloy. ....	84
<b>Figure 6.33:</b> The electrochemical charging and discharging graph of the $(\text{Mg}_{0.70}\text{Ti}_{0.30})_{0.90}\text{Ni}_{0.10}$ is compared with $(\text{Mg}_{0.70}\text{Ti}_{0.30})_{0.90}\text{Ni}_{0.10}$ simultaneously alloy.....	85
<b>Figure 6.34:</b> The electrochemical de-hydrogenation graph of the $(\text{Mg}_{0.70}\text{Ti}_{0.30})_{0.90}\text{Ni}_{0.10}$ is compared with $(\text{Mg}_{0.70}\text{Ti}_{0.30})_{0.90}\text{Si}_{0.10}$ alloy. ....	86
<b>Figure 6.35:</b> The electrochemical de-hydrogenation graph of the $\text{Mg}_2\text{Ni}$ is compared with $(\text{Mg}_2\text{Ni})_{0.90}\text{Ti}_{0.10}$ and $(\text{Mg}_2\text{Ni})_{0.80}\text{Ti}_{0.20}$ alloy. ....	87
<b>Figure 6.36:</b> The electrochemical charging and discharging graph of the $(\text{Mg}_2\text{Ni})_{0.90}\text{Ti}_{0.10}$ .....	88
<b>Figure 6.37:</b> GITT graph for $(\text{Mg}_{0.70}\text{Ti}_{0.30})_{0.90}\text{Ni}_{0.10}$ .....	89
<b>Figure 6.38:</b> GITT graph of $(\text{Mg}_{0.70}\text{Ti}_{0.30})_{0.80}\text{Ni}_{0.20}$ .....	90
<b>Figure 6.39:</b> GITT graph of $(\text{Mg}_{0.70}\text{Ti}_{0.30})_{0.90}\text{Si}_{0.10}$ .....	90
<b>Figure 6.40:</b> Impedance measurement of $(\text{Mg}_{0.70}\text{Ti}_{0.30})_{0.90}\text{Ni}_{0.10}$ .....	92
<b>Figure 6.41:</b> Impedance measurement of $(\text{Mg}_{0.70}\text{Ti}_{0.30})_{0.80}\text{Ni}_{0.20}$ .....	93
<b>Figure 6.42:</b> Impedance measurement of $(\text{Mg}_{0.70}\text{Ti}_{0.30})_{0.90}\text{Si}_{0.10}$ .....	94



## **MAGNESIUM BASED HYDROGEN STORAGE MATERIALS**

### **SUMMARY**

Nowadays sustainable energy is becoming more important issue, according to depleting fossil fuel reserves. The primary energy sources must not depend on the fossil fuels. Moreover, fossil fuels cause several damage to environment. In order to meet the future energy demands, the new and renewable energy sources must be investigated to cope up energy needs. It is more preferable if the sources are renewable in the nature; such as solar, wind, biomass, water and geothermal. The renewable sources which are mentioned above cannot be used in mobile applications directly. The usage of portable electronic devices is increasing rapidly. With the increasing level of technology, batteries are considered as a vital equipment in supporting the energy needs of the high-tech devices. The cycle life time of the batteries plays also an important role in this technology. At this point hydrogen is expected to play a dominant role. One of the important aspects of hydrogen is only environmental friendly products are emitted in the exothermic reaction of hydrogen with oxygen in a fuel cell. But the problems related with the production and storage of hydrogen cause a debate in the usage of hydrogen in fuel cells.

Hydrogen is generally stored in high pressure cylinders. Some researches show that new light weight composite material cylinders can withstand the pressures up to 800 bars. But these cylinders have large volumes and energy required for compressing hydrogen inside them is also high. Such disadvantages limit the practical applicability of high pressure storage of hydrogen in cylinders. The other way for storing hydrogen is to store it atomically in metal hydride (MH). This method seems to be a solution for large volume problem of the storage. MHs provide a safe storage, and they do not need extensive safety precautions unlike compressed hydrogen gas.

The problem for atomically stored hydrogen is finding the metal-hydrogen system with a high gravimetric capacity. This problem can be solved with choosing the light-weight elements. Mg is one of the promising elements in light weight elements

which can store 7.7 wt.% H. Despite of its high capacity, it has a high desorption temperature (279°C) and slow hydrogen absorption-desorption kinetics. Thus, for improving the hydrogen storage capacity and also practical usage properties, Mg is going to be alloyed with the transition metals such as Sc, Ti, V and Cr. Magnesium Scandium alloys were investigated throughly for its hydrogen storage properties and it was suggested that Sc can be the good alloying element to Mg to achieve better hydrogen storage properties. Sc is expensive; thus this hinders it to be used in the practical application. Because of that Ti can be replaced instead of Sc to achieve the similar kind of hydrogen storage properties. In this research, Magnesium based alloy production, characterisation and hydrogen storage properties will be investigated.

For preparing Mg based alloys, mechanical alloying technique was used. Mechanical alloying is one of the best milling methods. This technique depends on some balls and some powder mixing in a vessel. Cold welding, fracturing, rewelding and flattening occurred during the milling process produce the proper alloy. Mechanical alloying is non equilibrium processing technique so the elements which cannot be alloyed in equilibrium conditions can be alloyed with this technique. The limiting conditions in the phase diagrams are not limiting properties for this technique. Mechanical alloying takes place completely in solid phase and since the Mg-Ti alloy is immiscible system, it is not possible to make an alloy through conventional melting. In this research, mechanical alloying technique is used for alloying Mg-Ti systems. XRD and SEM are used for characterization of the alloys. Second phase are not observed in the XRD patterns, that is taken as a proof of homogen alloys. The alloys that were planned at the beginning of the study were produced successfully. Mg-Ti-Si alloy was produced with a success in this study, that there was not a clear evidence for production of homogeneous Mg-Ti-Si alloy in literature. All the alloying process were performed in Argon gas glove box for avoiding the contaminations of metals.

Electrochemical methods were used to investigate the hydrogen storage properties of the alloys. Such as constant-current(CC) measurements, galvanostatic intermittent titration technique (GITT) and electrochemical impedance spectroscopy (EIS). The hydrogen storage capacities of all the alloys are evaluated and the hydrogen storage performances are compared with each other. Despite a significant improvement in 10



wt.% absorption-desorption kinetics in case of addition of Ni element to Mg-Ti alloy was obtained, the thermodynamic properties were not improved properly.

Addition of 20 wt.% Ni to Mg-Ti alloy can be considered as it showed almost the same improvement compared to the 10 wt.% Ni addition although the kinetic properties were slightly improved.

The best kinetical improvement among the alloys were prepared in this study was obtained for  $\text{Mg}_2\text{Ni}$  based alloys. Addition of Ti to  $\text{Mg}_2\text{Ni}$  alloy caused a considerable improvement in the kinetic properties of the alloy but the thermodynamic properties remained constant.

By keeping or more improving the kinetic properties of the 10 wt.% Ti  $\text{Mg}_2\text{Ni}$  alloy and improving the thermodynamic properties of it, it can be promising material for hydrogen storage. When the results of alloys containing Si element are compared with the other ternary alloys, it is observed the alloys containing Si are showed poor properties with respect to both in capacities and thermodynamic properties. Since the  $\text{Mg}_2\text{Si}$  binary alloy has low storage capacity, any comments on kinetic and thermodynamic properties of it does not need to be performed.

Mg-Ti-Si alloy that is produced in bulk form in this study was compared with the results are given in the literature for the alloys produced in thin film method and observed that the kinetic behaviour of bulk form is poor. This not an unexpected result when the production methods are considered.



## **MAGNEZYUM ESASLI HİDROJEN DEPOLAMA MALZEMELERİ**

### **ÖZET**

Yenilenebilir enerji, günümüzde fosil yakıtların tükenmeye başlamasıyla daha büyük bir önem kazanmıştır. Birincil enerji kaynakları tükenen fosil yakıtlara bağımlı olmamalıdır. Fosil yakıtların çevreye verdiği zararlar büyük boyutlardadır. Bu nedenlerden ötürü yeni ve yenilenebilir enerji kaynaklarının araştırılması zorunlu hale gelmiştir. Alternatif enerji kaynaklarının doğada yenilenebilir olarak bulunması tercih edilmektedir; güneş, rüzgar, biokütle ve jeotermal gibi. Bahsedilen bu kaynaklar, taşınabilir uygulamalar için doğrudan kullanılamamaktadır. Taşınabilir uygulamaların teknolojisi ve onlara olan talep gün geçtikçe artmaktadır. Teknolojinin gelişiminde, yüksek teknoloji kullanan cihazların enerji gereksinimlerinin karşılanmasında, piller önemli bir ekipman olarak göz önüne alınmalıdır. Pillerin dolum-boşalım ömürlerinin süresi bu teknolojiye önemli bir rol oynamaktadır. Bu noktada hidrojenin büyük rol oynaması beklenmektedir. Hidrojenin ve oksijenin yakıt hücresindeki ekzotermik reaksiyonunda açığa çıkan ürünler çevre dostudur. Ancak hidrojen üretimi ve depolanması ile ilgili sorunlar, hidrojenin yakıt pillerinde kullanılmasını tartışmalı hale getirmektedir.

Hidrojenin depolanması genellikle yüksek basınç tanklarında gerçekleştirilmektedir. Yapılan bazı çalışmalar, 800 bar basınca kadar dayanabilen kompozit malzemeden yapılmış tanklarda depolamanın yapılabileceğini göstermiştir. Fakat bu tanklar büyük hacime sahip olup, hidrojeni tanklara sıkıştırmak için yüksek enerji gerekmektedir. Bu gibi olumsuzluklar yüksek basınç altında depolama yöntemin uygulanabilirliğini kısıtlamaktadır. Hidrojenin depolanması için bir diğer yöntem de atomik olarak metal hidritlerde (MH) depolanmasıdır. Bu yöntem yüksek hacim problemine bir çözüm olabilir gibi gözükmektedir. Hidrojenin MH’de depolanması, emniyet açısından daha güvenilir bir yöntemdir.

Atomik seviyede hidrojen depolamanın olumsuz yanı, yeterince yüksek kapasitede depolama yapılabilecek MH’lerin günümüzde mevcut olmamasıdır. Bu olumsuzluk,

hidrojen depolanması için hafif elementlerin seçilmesi ile giderilebilir. Ağırlıkça %7.7 hidrojen depolayabilen magnezyum, hafif elementler arasında umut veren elementlerden birisidir. Magnezyum yüksek depolama kapasitesine karşın, hidrojen salım sıcaklığı (279 °C) yüksek olup, hidrojeni absorplama ve desorplama kinetiğini yavaştır. Bu nedenle Magnezyum; Sc, Ti, V ve Cr gibi geçiş metalleri ile alaşımlar oluşturularak, gerek depolama özelliği gerekse de pratik kullanım özellikleri geliştirilmeye çalışılmaktadır. Mg-Sc alaşımları, bunların hidrojen depolama özellikleri bakımından ayrıntılı olarak incelenmiş ve Sc elementinin, Mg elementine daha iyi hidrojen depolama özelliği kazandırabileceği ortaya konulmuştur. Sc pahalı bir elementtir, bu durum onun pratik uygulamalarda kullanımını kısıtlamaktadır. Bundan dolayı Mg ile olabilecek alaşımlarda Sc yerine Ti kullanılabilir. Bu çalışmada, Magnezyum esaslı alaşımların üretimi, karakterizasyonu ve hidrojen depolama özellikleri incelenecektir.

Mg esaslı alaşımların oluşturulması için; mekanik alaşımlama yöntemi kullanılmıştır. Mekanik alaşımlama, öğütme işlemleri arasında en başarılı yöntem olarak değerlendirilmektedir. İşlem, bir miktar bilye ve metal tozunun hazne içerisinde karıştırılması esasına dayanmaktadır. Karışma işlemi sırasında mikroskobik boyutta tekrarlanan çarpışma, soğuk kaynama ve kırılma işlemleri, istenilen alaşımın üretilmesini sağlamaktadır. Mekanik alaşımlama yönteminin en önemli avantajlarından birisi denge koşullarında alaşım yapılamayacak elementlerin alaşımlanabilmesidir. Mekanik alaşımlama tamamen katı fazda meydana gelir ve faz diyagramlarında belirtilen sınırlamalar bu yöntem için sınırlayıcı değildir. Mg-Ti alaşımı karışmaz bir sistem olması nedeniyle, metallerin eritilerek alaşım oluşturulması mümkün olmamaktadır. Bu çalışmada, Mg-Ti alaşımı için mekanik alaşımlama tekniği uygulanmıştır. Üretilen malzemelerin karakterizasyonu, XRD ve SEM ölçümleri aracılığıyla gerçekleştirilmiştir. XRD sonuçlarında ikinci faz oluşumu gözlenmemiş olup bu da homojenize alaşım elde edildiğinin kanıtı olarak değerlendirilmiştir. Çalışmada planlanan alaşımlar başarı ile elde edilmiştir. Literatürde homojen Mg-Ti-Si üçlü alaşımının başarılı bir şekilde elde edildiğine dair kesin vurgulara rastlanmamış olup, bu çalışmada homojen üçlü alaşım başarılı bir şekilde üretilmiştir. Metallerin ve elde edilecek alaşımların kontaminasyonundan kaçınmak için alaşımlama işlemleri Argon gazı atmosferinde el ile doğrudan temasın olmadığı kapalı bir ortamda gerçekleştirilmiştir.

Mg esaslı malzemelerin hidrojen depolama özellikleri Sabit Akım (CC), Galvanostatik Intermittent Titrasyon tekniği (GITT) ve Elektrokimyasal İmpedans Spektroskopisi (EIS) gibi elektrokimyasal yöntemlerle belirlenmiştir. Üretilen her bir alaşım için hidrojen depolama özellikleri değerlendirilmiş ve hidrojen depolama performansları karşılaştırılmıştır. Ağırlıkça %10 Nikel ilave edilen Mg-Ti alaşımında absorpsiyon-desorpsiyon kinetiği önemli bir gelişim göstermiş olup, termodinamik özellikler açısından ise bir gelişim gözlenmemiştir. %20 Ni ilave edilmesi durumunda ise kinetikte çok az bir gelişim olmakla birlikte, %10 Ni ilavesine yaklaşık olarak benzer bir gelişim gözlenmiştir.

Üretilen malzemeler içerisinde kinetik açıdan en olumlu sonuç  $Mg_2Ni$  esaslı alaşımlarda elde edilmiştir.  $Mg_2Ni$  alaşımına Ti ilave edilmesi malzemenin kinetik özelliklerinde belirgin bir iyileştirmeye neden olmuş olup termodinamik özelliklerinde herhangi bir gelişmeye neden olmamıştır. Bu alaşımın iyileştirilen kinetik özellikleri muhafaza edilerek veya daha fazla geliştirilerek, termodinamik özelliklerinin de geliştirilmesiyle gelecek vadede malzemeler üretilebilecektir. Si ile üretilen alaşımlara ait sonuçlar, diğer üretilen üçlü alaşımların performansları ile karşılaştırıldığında, Si esaslı alaşımların gerek kapasite gerekse de termodinamik bakımdan daha olumsuz sonuçlar verdiği gözlenmiştir.  $Mg_2Si$  ikili alaşımının depolama kapasitesinin düşük olması nedeniyle kinetik ve termodinamik özellikleri hakkında bir yorum yapılamamıştır. Bu çalışmada yığın formunda üretilen Mg-Ti-Si alaşımının kinetiği, literatürde ince film yöntemiyle üretilen alaşımına göre daha olumsuz bir durum göstermiştir. Bu da üretim yöntemleri dikkate alındığında beklenen bir durumdur.



# 1 INTRODUCTION

## 1.1 The Hydrogen Economy

In the foreseeable future, fossil fuel reserves will be largely exhausted. Man-made changes to the climate make a more sustainable society necessary [1]. The fossil fuel reserves-to-production ratio (results of the annual assessment by BP) is depicted in Figure 1.1 and it has been shown that the oil and natural gas reserves will run out in the following 50 years [2]. Although coal will be available for a slightly longer period of time, it will inevitably become scarce as well in the near future. Another important reason for decreasing our dependency on fossil fuels is that they have to be imported from politically unstable regions. Therefore we need to think about new ways to ensure energy needs are met. These new resources should be renewable in nature, e.g. wind, solar, biomass, water and geothermal, and should be used for stationary applications.

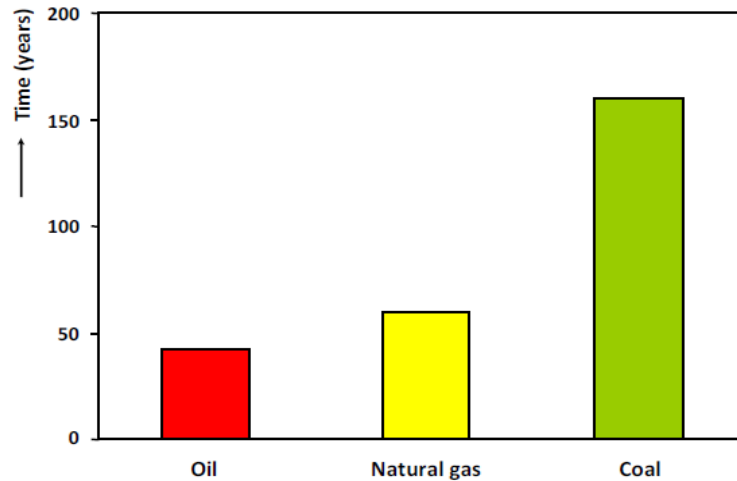


**Figure 1.1:** Fossil fuel reserves-to-production ratios at the end of 2006.

For mobile applications (e.g. fuel-cell driven vehicle), the use of an on-board energy system is indispensable. Hydrogen is going to play a dominant role in future energy scenarios [3,4]. So the other important point of view of hydrogen is that only environmentally friendly combustion products are emitted in the exothermic reaction of hydrogen with oxygen or when hydrogen is oxidized in a fuel cell. But the feasibility of hydrogen production, storage and the consumption are still under discussion.

Usually hydrogen is produced by steam reforming of fossil fuels, by partial oxidation of natural gas or by coal gasification. But these methods still rely on fossil fuels and they are not useful for solving the fossil fuel problems. There is an alternative method for generating the hydrogen with electrolysis of water, but it is considered to be not very efficient. Other techniques for producing hydrogen include high-temperature electrolysis, which can increase the efficiency and hydrogen generation by chemical reactions of certain algae for example *Scenedesmus* [5,6].

For increasing the density of hydrogen as much as possible, it is stored in high-pressure cylinders. Lightweight composite cylinders have been developed and they are able to stand up to 800 bars pressures. In the future, it is expected that hydrogen cylinders are withstand even higher pressures. But their large volumes and the energy for compressing the hydrogen will limit their practical applicability. The other way to increase the hydrogen density to  $70 \text{ kg/m}^3$  is to liquefy it under cryogenic conditions. A significant increase of the density and a strong reduction of the necessary volume for a certain amount of hydrogen can be achieved by storing hydrogen atomically in a metal, forming a metal hydride (MH). Metal hydrides procure safe storage as they can be handled without extensive safety precautions (e.g. compressed hydrogen gas).

The lists of the technical requirements for an on-board hydrogen storage system as determined by the U.S. Department of Energy are shown in Table 1.1. The primary problem of solid state storage is to find a metal-hydrogen system with a gravimetric capacity that exceeds 6 wt.% H and absorbs/desorbs hydrogen at atmospheric pressures at slightly elevated or ambient temperatures [7].



**Table 1.1:** U.S. Department of Energy Technical Targets: On-Board Hydrogen Storage Systems.

Storage Parameter	Deadline: 2010
Gravimetric capacity	At least 6 wt. %
Fill time (5 kg H <sub>2</sub> )	Within 3 minutes
Volumetric capacity	45 kg m <sup>-3</sup>
Equilibrium pressure	~1 bar @ 353 K
Cycle life	>1000
Storage System Cost	\$ 133

The most common hydrides of the elements are listed in Figure 1.2. This list can be found in the reports of Griessen et al. and Huheey [8,9]. The different colors signify the difference in the nature of the bond between the element and hydrogen going from a high degree of ionic bonding character for groups I and II (alkali metals and alkaline earth metals) to covalently bonding for the elements in groups XIV to XVII. The bond to hydrogen for the elements in groups III to X (transition metals, actinides and lanthanides) strongly depends on the element; however, many are interstitial in nature. Finally, the hydrogen bonding character to the elements in groups XI to XIII is covalent and these hydrides are enigmata species and some polymerize. The values below the hydride compositions in Figure 1.2 correspond to the gravimetric capacity.

	I																		XVIII	
1	H																	He		
	II												XIII	XIV	XV	XVI	XVII			
2	LiH 12.7	BeH <sub>2</sub> 18.3											BH <sub>3</sub> 21.9	CH <sub>4</sub> 25.1	NH <sub>3</sub> 17.8	H <sub>2</sub> O 11.2	HF 5.0	Ne		
3	NaH 4.2	MgH <sub>2</sub> 7.7											AlH <sub>3</sub> 10.1	SiH <sub>4</sub> 12.6	PH <sub>3</sub> 8.9	H <sub>2</sub> S 5.9	HCl 2.8	Ar		
			III	IV	V	VI	VII	VIII	IX	X	XI	XII								
4	KH 2.5	CaH <sub>2</sub> 4.8	ScH <sub>2</sub> 4.3	TiH <sub>2</sub> 4.0	VH <sub>0.5</sub> 1.0	CrH 1.9	MnH <sub>0.5</sub> 0.9	FeH <sub>0.5</sub> 0.9	CoH <sub>0.5</sub> 0.9	NiH <sub>0.5</sub> 0.9	CuH 1.6	ZnH <sub>2</sub> 3.0	GaH <sub>3</sub> 4.2	GeH <sub>4</sub> 5.3	AsH <sub>3</sub> 3.9	H <sub>2</sub> Se 2.5	HBr 1.2	Kr		
5	RbH 1.2	BaH <sub>2</sub> 1.4	YH <sub>3</sub> 3.3	ZrH <sub>2</sub> 2.2	NbH <sub>2</sub> 2.1	MoH <sub>0.5</sub> 0.5	TcH <sub>0.5</sub> 0.5	Ru	RhH <sub>0.5</sub> 0.5	PdH <sub>0.6</sub> 0.6	Ag	CdH <sub>2</sub> 1.8	InH <sub>3</sub> 2.6	SnH <sub>4</sub> 3.3	SbH <sub>3</sub> 2.4	H <sub>2</sub> Te 1.6	HI 0.8	Rn		
6	CsH 0.8	SrH <sub>2</sub> 2.2	*	LuH <sub>2</sub> 1.1	HfH <sub>2</sub> 1.1	TaH 0.6	W	Re	Os	Ir	Pt	AuH <sub>3</sub> 1.5	HgH <sub>2</sub> 1.0	TlH <sub>3</sub> 1.5	PbH <sub>4</sub> 1.9	BiH <sub>3</sub> 1.4	H <sub>2</sub> Po 1.0	HAt 0.5	Xe	
7	Fr	RaH <sub>2</sub> 0.9	**	Lr	Rf	Db	Sg	Bh	Hs	Mt	Ds	Rg	Uub	Uut	Uuq	Uup	Uuh	Uus	Uuo	
			*	LaH <sub>3</sub> 2.1	CeH <sub>2</sub> 1.4	PrH <sub>2</sub> 1.4	NdH <sub>2</sub> 1.4	Pm	SmH <sub>2</sub> 1.3	Eu	GdH <sub>2</sub> 1.3	TbH <sub>2</sub> 1.3	DyH <sub>2</sub> 1.2	HoH <sub>2</sub> 1.2	ErH <sub>2</sub> 1.2	TmH <sub>2</sub> 1.2	YbH <sub>2</sub> 1.2			
			**	AcH <sub>2</sub> 0.9	ThH <sub>2</sub> 0.9	PaH <sub>1.3</sub> 0.6	UH <sub>3</sub> 1.25	NpH <sub>2</sub> 0.8	PuH <sub>2</sub> 0.8	AmH <sub>2</sub> 0.8	Cm	Bk	Cf	Es	Fm	Md	No			

**Figure 1.2:** Periodic table of elements with per element the most common hydrides and corresponding gravimetric capacity in wt.% H.

Most of the elements presented in Figure 1.2, based on the weight constraints for on-board hydrogen storage systems, are not particularly suitable as effective hydrogen storage medium. Therefore, the lightweight elements that can store a significant amount of hydrogen are of prime interest. And, the hydride phase is important as it has a great effect on the volumetric capacity. CH<sub>4</sub> can be an example for this situation. It is gas at ambient temperatures, which has lower the volumetric capacity compared to storing hydrogen in a solid. According to this, Mg is one of the most promising elements as it exhibits a high gravimetric storage capacity of 7.7 wt.% of hydrogen and a high volumetric capacity of 110 kg/m<sup>3</sup> [10, 11]. Regardless of the fact that its excellent storage capacity, the high desorption temperature (279 °C), low plateau pressure and extremely slow hydrogen (de)sorption kinetics prevent Mg from being employed commercially [12]. It is generally accepted that the formation of a MgH<sub>2</sub> layer blocks further hydrogen diffusion, effectively decreasing the high storage capacity[13 -22].

Despite the fact that its apparent drawbacks, Mg is often a large constituent of new hydrogen storage materials as it increases the gravimetric capacity. These systems properties should not be influenced too much by the poor diffusion properties of Mg

and a fine line between blocked Mg-like behavior and improved properties is often found.

## 1.2 Other Applications of Metal Hydrides

Large scale application of metal hydrides as solid state hydrogen storage medium for the hydrogen economy is going to be shown in this chapter.

### 1.2.1 Rechargeable batteries

The reactions in a rechargeable battery, both the electrochemical reaction at the positive electrode and the negative electrode are reversible. Ions are transported through the electrolyte, while electrons move through the external circuit for example a mobile phone. Three types of rechargeable battery are in common use: NiMH, NiCd and Li-ion. But NiCd is going out of use because of the toxicity of Cd. The schematic view of a NiMH battery together with the basic electrode reactions depicted in Figure 1.3 [23]:

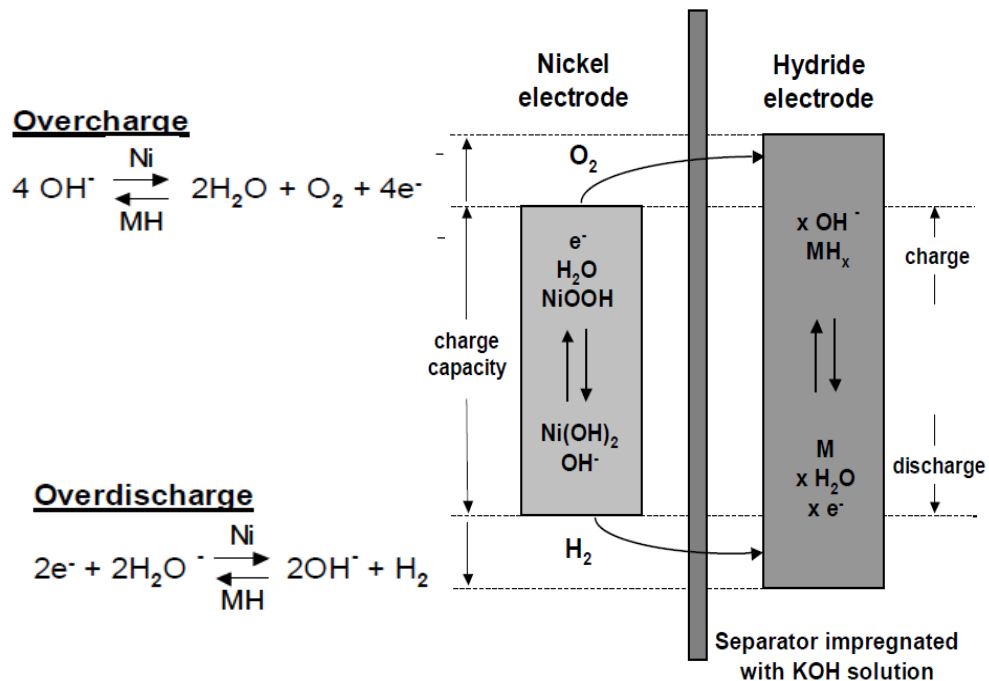
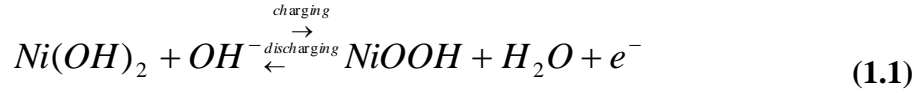


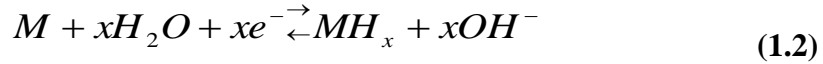
**Figure 1.3:** Schematic overview of the chemistry of a rechargeable NiMH battery.

The positive and negative electrodes are electrically insulated from each other by a separator and together are rolled into a cylinder-shaped stack. Both the electrodes and separator are impregnated with an electrolyte to facilitate the transport of ions

between the electrodes. NiCd and NiMH are alkaline batteries where the electrolyte is a concentrated aqueous solution of KOH and LiOH. The positive electrode reaction is:

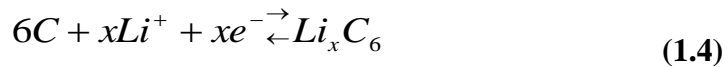
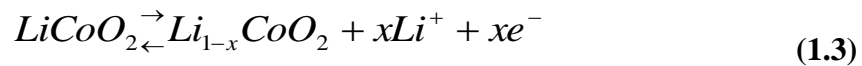


Negative electrode reaction for NiMH battery:



In Figure 1.3 it is shown that side reactions occur during overcharge and overdischarge. The hydrogen and oxygen gas that is generated and recombined at the MH electrode and in theory this is not harmful to the battery if the state of over(dis)charge does not persist for too long. An important disadvantage of Ni-MH batteries is that the use of an aqueous electrolyte limits the maximum battery voltage to ~1.4 V.

Another type of rechargeable battery is Li-ion battery that is nowadays in common use in portable electronics. Here, in Li-ion batteries, positive  $Li^+$  ions are transported through the electrolyte instead of negative  $OH^-$  ions. The electrolyte consists of a Li-salt,  $LiPF_6$  or  $LiClO_4$ , dissolved in an organic solvent at a concentration of ~1M. The positive electrode material is a layered oxide such as  $LiCoO_2$  and the negative electrode is graphite. The electrode reactions:



Opposite to the NiMH battery; in a Li-ion battery, the reaction products of electrolyte decomposition are not recombined at the other electrode. Overcharge and over discharge will result in irreversible damage.

Of course, all three types of rechargeable battery have their own advantages and disadvantages. Environmental concerns as well as a 30-50% lower energy density compared to NiMH have caused Ni-Cd batteries to be gradually replaced by either NiMH or Li-ion batteries. NiMH has the advantage of safety and low cost. The good resistance to overcharge and over discharge, especially compared to Li-ion, makes

them most suitable for applications where multiple cells need to be used in parallel or in series when higher voltages and currents are needed in (e.g. Hybrid Electric Vehicles). But, the aqueous electrolyte limits the voltage of an individual cell to 1.2-1.5 V. Li-Ion batteries contain organic electrolytes and have a much higher average discharge voltage of ~3.7 V. So the energy density in Wh/kg or Wh/L is higher for Li-ion than for Ni-MH [23], despite a lower storage capacity in mAh/g, that is the reason why portable electronics almost exclusively use Li-ion batteries.

### **1.2.2 Gas purification and (isotope) separation & reversible gettering**

Metal hydrides can be used as membranes to separate  $H_2$  from other gaseous compounds or to purify  $H_2$ . This can be achieved by, for example, employing PdAg alloy membranes, which is permeable to hydrogen, but not (in any reasonable length of time) to other gases. Metal hydrides do not only absorb hydrogen, but also deuterium (D) and tritium (T). The properties change according to the absorbing/desorbing species, which can effectively be exploited to separate the isotopes. Requirements for the MH system are fast kinetics, ease of activation, resistance to impurities, reaction efficiency, stability, durability and safety. Another application of metal hydrides is as reversible getter in vacuum systems, which can be employed to remove trace amounts of  $H_2$ . The foremost requirements for the metal hydrogen system in this application are a low pressure, fast kinetics, ease of activation, pumping speed and durability.

### **1.2.3 Electrochromic windows and hydrogen sensors**

The optical switching behavior of rare earth metals (Y and La) as a function of hydrogen content was first reported in 1996 [24]. Soon after this discovery it was realized that an interesting field of new futuristic applications could be exploited with these switchable mirrors, ranging from smart windows and optical shutters to active displays. In many cases gas phase switching is not the most attractive one, especially, when a highly reactive gas, such as hydrogen, is involved. It is therefore much more attractive to use devices that are electronically driven. The concept of electrochemical switching has been investigated thoroughly for so-called inorganic electrochromic electrode materials by Grundvist [25]. Notten et al. [26] investigated the electro-optical properties of rare earth (RE) thin films, which has the advantage over gas phase loading that the hydrogen concentration can be carefully controlled

by the electrical current. One of the disadvantages of these films is that their trihydrides are colored, while, from an application point-of view, transparent films are desirable. Van de Sluis et al. [27] reported that alloying Gd, Sm, Lu, Y with Mg allows one to control both the film transmission and reflectivity properties. The next generation of switchable mirrors started with the study of Richardson et al. on Mg-transition metal (TM) alloys, revealing that the optical switching behavior of alloys of Mg and Ni is similar as found for Mg-RE alloys [28-29]. Hereafter it was shown that alloys of Mg and Co, Fe, Mn and V also switch as a function of hydrogen content [30]. Recently, Niessen et al. [31] showed that alloys that consist of elements that are immiscible with Mg, like Ti, V and Cr, can be prepared via a thin film approach. These compounds are capable of absorbing a substantial amount of hydrogen. Moreover, the hydrogen content in these materials strongly affects the optical properties, which can, for instance, be exploited in hydrogen sensor applications, smart solar collectors or switchable mirrors [32 -36].

### 1.3 Scope

The general scope of this thesis is characterizing light weight Mg-based materials to find new opportunities in the field of bulk state hydrogen storage.

Theoretical introduction is given about the electrochemical methods, especially applied to hydrogen storage materials, used in present work. More specifically, constant-current charging and discharging, galvanostatic intermittent titration technique and impedance spectroscopy are introduced. Furthermore, the experimental details on alloy and electrode preparation and the experimental electrochemical setup will be described.

General overview of hydrogen storage materials are going to be given. The fifth class of materials that will be discussed are Magnesium-based alloys.  $\text{MgH}_2$  contains twice as much hydrogen (7.6 wt. %) as the Transition Metal-based hydrides. Unfortunately,  $\text{MgH}_2$  suffers from a number of shortcomings such as slow sorption kinetics and low equilibrium pressure that will also be discussed. Thin films of Mg alloyed with Rare-Earth metals exhibit interesting optical properties as well as improved hydrogenation kinetics.

## **2 MECHANICAL ALLOYING**

### **2.1 Mechanism of Alloying**

The powder particles, during high-energy milling, are repeatedly flattened, cold welded, fractured and rewelded.

While the two steel balls collide, some of the powder is pent up in between them. Approximately 1000 particles with an aggregate weight of about 0.2 mg are trapped during each collision, depicted in Figure 2.1. The impact's force plastically deforms the powder particles leading to work hardening and fracture. So the new surfaces created enable the particles for welding together and this ushers in increasing the particle size. From the early stages of milling, the particles are soft, does not matter either ductile-ductile or ductile-brittle material combination, their tendency to weld together and form large particles is high. Some of the particle sizes develop three times bigger than the starting particles. At this level composite particles at this stage have a characteristic layered structure composed several combinations of the starting constituents. As the deformation continued, the particles get work hardened and fracture by a fatigue failure mechanism and/or by the fragmentation of fragile flakes. Fragments which generated by this mechanism that has a possibility to continue reducing in size in the lack of strong agglomerating forces. At this stage, the tendency to fracture predominates over cold welding. On account of the continued dashing of grinding balls, the structure of the particles is steadily refined, but the particle sizes proceed to be the alike. Therefore, the inter-layer space decreases. The number of layers in a particle increase.

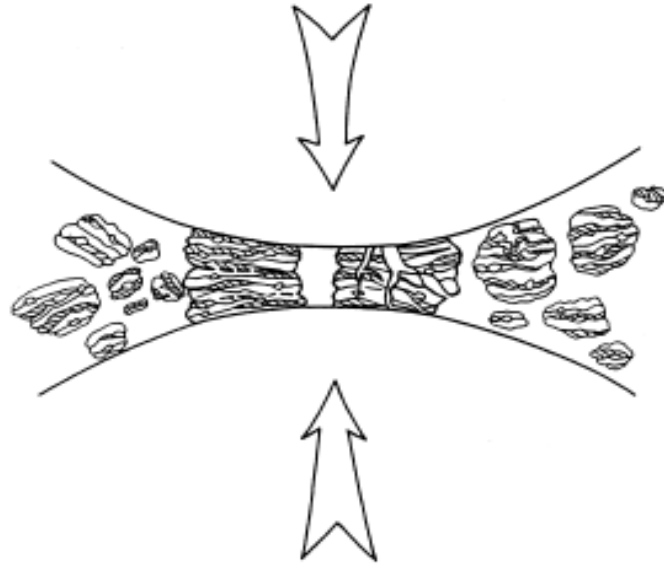


**Figure 2.1:** Ball-powder-ball collision of powder mixture during mechanical alloying.

The steady-state equilibrium is reached, after milling for a certain amount of time, when a balance is reached between the rate of welding, that tends to increase, the rate of fracturing, and the average particle size which is disposed to decrease the average composite particle size [37].

From the afore-mentioned it is obvious that during mechanical alloying (MA), heavy deformation is introduced into the particles. This is appeared by the occurrence of a variety of crystal defects for example; stacking faults, dislocations, vacancies, and increased number of grain boundaries. The presence of this defect structure improves the diffusivity of solute elements into the matrix. Yet another, the refined micro structural features decrease the diffusion spaces. In addition to that, the small rise in temperature while milling further aids the diffusion behavior, thus true alloying takes place in between the constituent elements. While this alloying generally occurs at the room temperature, sometimes it could be necessary to anneal the mechanically alloyed powder at an increased temperature for alloying to be achieved. This is especially true when formation of intermetallics is wanted.

Time that required for developing a given structure in any system is a function of the initial particle size and characteristics of the ingredients as well as the specific equipment used for conducting the MA operation and the operating parameters of the equipment. In many cases, the rate of refinement of the internal structure; for



example particle size, crystallite size, lamellar spacing, etc.; is roughly logarithmic with processing time and because of this, the size of the starting particles is comparatively unimportant. In a few minutes to an hour, the lamellar spacing generally becomes small and the crystallite (or grain size) is refined to nanometer dimensions ( $10 \text{ \AA}$  or  $1 \text{ nm} = 10^{-9} \text{ m}$ ) as shown in Figure 2.2. The ease with which nanostructured materials can be synthesized is one reason why MA has been extensively employed to produce nanocrystalline materials. Rate of refinement increases with higher milling energy, ball-to-powder weight ratio, lower temperature, etc. [38]. So, it is possible to carry out MA of three different combinations of metals and alloys: ductile-ductile, ductile-brittle, and brittle-brittle systems.

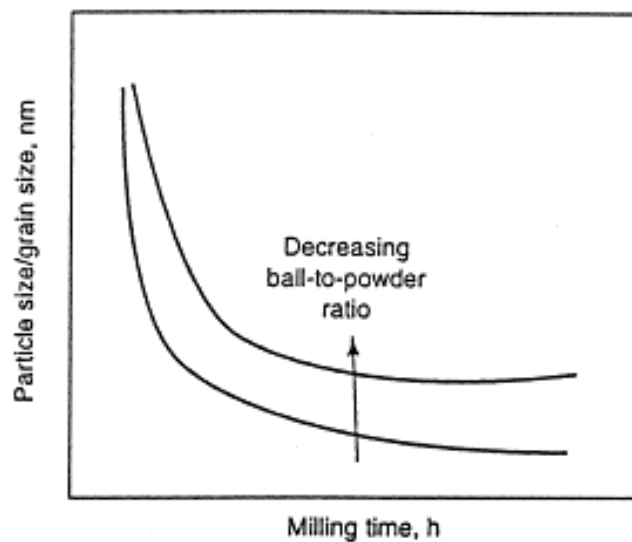


**Figure 2.2:** Refinement of particle and grain sizes with milling time.

### 2.1.1 Ductile-ductile components

For ductile-ductile components can be said the ideal combination of materials for MA. Benjamin [37] offered that it was necessary to have at least 15% of a ductile component for succeed alloying. The reason for this; true alloying occurs because of the repeated cold welding and fracturing of powder particles; if the particles are not ductile, cold welding cannot occur. At initial stages of milling the particles get flattened due to impact of the balls. The different flatted powder particles cold weld each other and form a composite lamalle structure. With longer milling, the elemental lamellae of the welded layer and both the coarse and fine powders become spiral rather than being linear, depicted in Figure 2.3. Alloying starts to take place in

this level because of the combination of decreased diffusion distances (interlamellar spacing), increased lattice defect density, and any heating that may have occurred during the milling operation. This stage called steady-state processing; the hardness and particle size are apt to reach a saturation value. With further milling, true alloying takes place at the atomic level resulting in the formation of solid solutions, intermetallics, or even amorphous phases. The layer spacing becomes so fine or disappears at this stage so that it is not visible at an optical microscope.

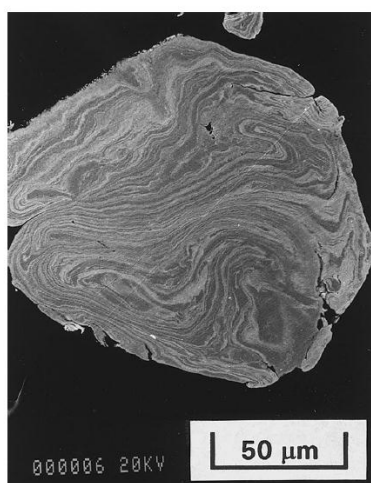


**Figure 2.3:** Scanning electron micrograph depicting the convoluted lamellar structure obtained during milling of a ductile-ductile component system (Ag-Cu).

### 2.1.2 Ductile-brittle components

As an example the oxide-dispersion strengthened (ODS) alloys are in ductile-brittle category because the brittle oxide particles are dispersed in a ductile matrix. Benjamin and others described the microstructural evolution in this type of system [39-40]. In the early stages of milling, the ball-powder-ball collisions making the ductile metal powder particles flattened, during the brittle oxide or intermetallic particles get fragmented/comminuted.

These fragmented brittle particles tend to become occluded by the ductile constituents and pent up in the ductile particles. As shown in Figure 2.4a, the brittle constituent is closely spaced along the interlamellar spacings. In Figure 2.4b, with longer amount of time milling, the ductile powder particles get work hardened, the lamellae get convoluted, and refined.

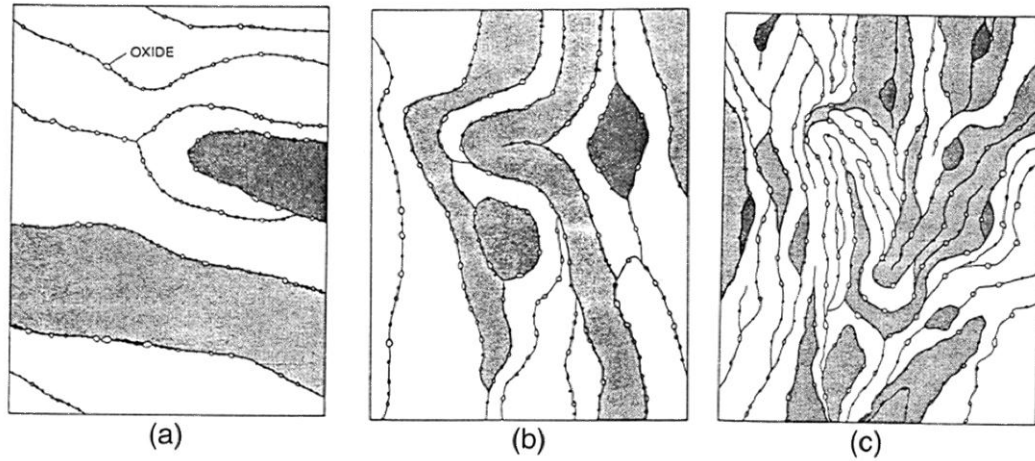


**Figure 2.4:** Schematics of microstructural evolution during milling of a ductile-brittle combination of powders.

The individual particles' composition converges on toward the overall composition of the starting powder blend. If milling is continued, the lamellae is going to get more refined, the interlamellar gap decreases, and the brittle particles get uniformly dispersed, so whether they are insoluble, in the ductile matrix, for example, as in an ODS alloy can be seen in Figure 2.4c.

On the other part, if the brittle phase is soluble, alloying takes place between the ductile and brittle components also and chemical homogeneity is reached. Formation of an amorphous phase on milling a mixture of pure Zr (ductile) and  $\text{NiZr}_2$  intermetallic (brittle) powder particles can be an example of this system [41]. If alloying occurs, that also depends on the solid solubility of the brittle component in the ductile matrix. If a component has a negligible solid solubility then alloying is unlikely to take place. Because of this, ductile-brittle alloys during MA do not only require fragmentation of brittle particles to facilitate short-range diffusion, but also reasonable solid solubility in the ductile matrix component.

### 2.1.3 Brittle-brittle components

It would be not easy to alloy in a system that contains two or more brittle components. The reason for this; the absence of a ductile component prevents any welding from occurring, and in its absence, alloying is not expected to take place. Nevertheless, it is reported that alloying occur in brittle-brittle component systems such as Si-Ge and Mn-Bi [42,43]. Milling of brittle intermetallics mixture produced amorphous phases[44]. The brittle components are getting fragmented during milling

and particle size decrease continuously. The powder particles (at very small particle sizes) act like ductile, and further reduction in size is not possible; that is called the limit of comminution [45]. During milling of brittle-brittle systems, it is seen that the harder, which means more brittle, component gets fragmented and gets embedded in the softer, which means less brittle, component. Because of this, as shown in Figure 2.5, the harder Si particles are embedded in the softer Ge matrix. The scanning electron micrograph showing that the harder Si particles are incorporated in a softer Ge matrix after mechanically alloying the Si-Ge powder mix for 12 h.

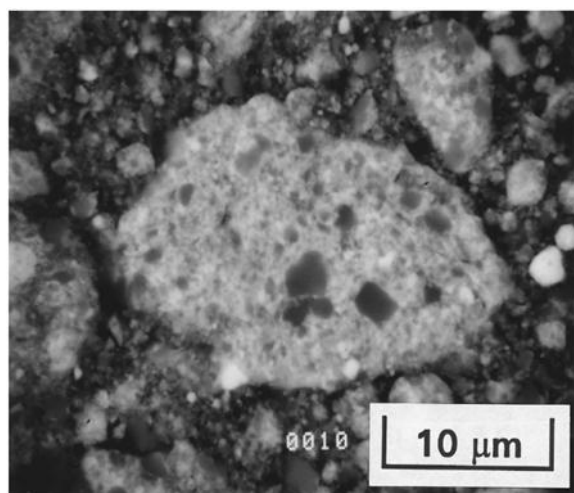


**Figure 2.5.** Scanning electron micrograph of the Si-Ge powder mix for 12 h.

Even though diffusion rises to be main property for alloying to occur in all types of systems, at very low temperatures (e.g., liquid nitrogen temperatures) the alloying did not occur in the brittle-brittle systems (Si-Ge), while alloying was found to occur at sub-ambient temperatures in the ductile-ductile and ductile-brittle systems. This may be because of the longer diffusion distances required in the brittle-brittle granular vs. ductile-ductile lamellar geometry, and/or the enhanced diffusion paths provided by severe plastic deformation in ductile-ductile systems. The mechanisms could be possible that may make a contribution to material transfer while milling of brittle components might include plastic deformation, which is made possible by (a) microdeformation in defect-free volumes, (b) local temperature rise, (c) surface deformation, and/or (d) hydrostatic stress state in the powders while milling [43].

## **2.2 The Process of Mechanical Alloying**

Mechanical alloying process starts with mixing the powders in right proportion after that loading the powder mix into the mill along with the grinding medium. Steel balls can be used. The mixture is going to be milled for the desired period of time until the system reaches steady state. The important components of the MA process are the mill, the raw materials, and the process variables.

### **2.2.1 Raw materials**

Commercially pure powders can be used as raw materials used for MA and the particle sizes should be in the range of 1-200  $\mu\text{m}$ . The reason is; the powder particle size decreases exponentially with time and reaches a small value of a few microns only after a few minutes of milling because of this reason the particle size of powder is not very critical but the powder's particle size should be smaller than the grinding ball size. In Figure 2.6 process flow sheet and the microstructures developed during double mechanical alloying (dMA) of an Al-5wt-Fe-4wt-Mn powder mixture can be seen.

Wet grinding is a process of the metal powders are milled with a liquid medium [46-48]; if this process contains no liquid, it is called dry grinding. The solvent molecules are adsorbed on the newly formed surfaces of the particles and lower their surface energy because of this wet grinding is more suitable method than dry grinding to get finer-ground products. Also the less-agglomerated condition of the powder particles can be taken into account for wet circumstance. Dolgin et al. [49] reported that the rate of amorphization is faster during wet grinding than during dry grinding. The minus side of the wet grinding is, increasing contamination of the powder. Because of this most of the MA operations have been implemented in dry conditions [50].

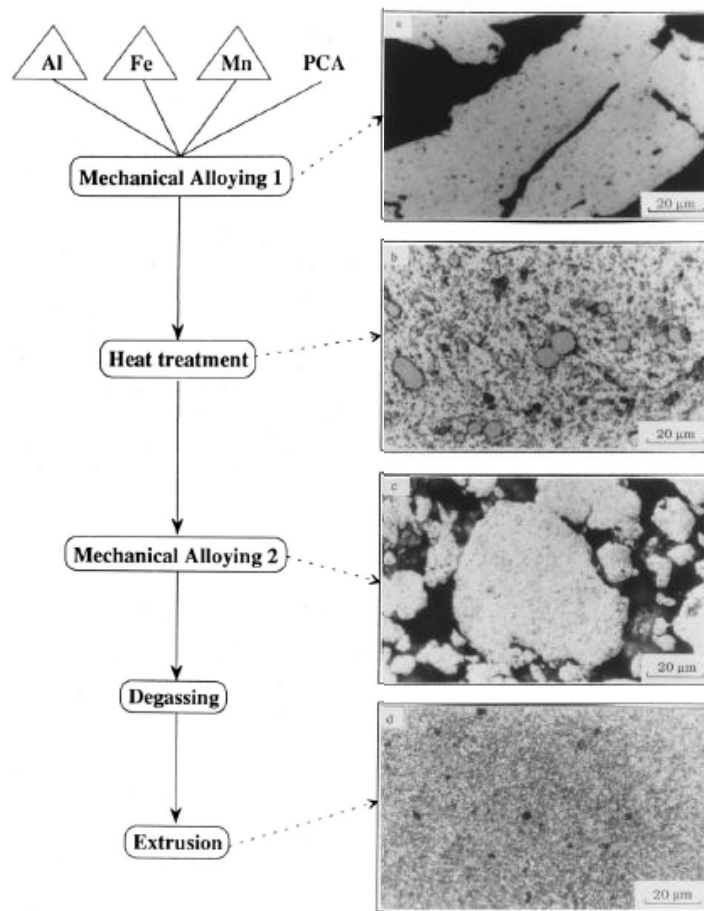


**Figure 2.6.** Process flowsheet and the microstructures developed during double mechanical alloying (dMA) of an Al-5wt.% Fe-4wt.% Mn powder mixture.

## 2.2.2 Types of mills

For produce mechanically alloyed powders, different types of high-energy milling equipment can be used. They show a change in their capacity, efficiency of milling and additional arrangements for cooling, heating, etc.

### 2.2.2.1 SPEX shaker mills

This type of mill is used for mechanical alloying in this study. It is common for laboratory investigations and for alloy screening purposes. They can mill about 10-20 g of the powder at a time. These mills are manufactured by SPEX CertPrep, Metuchen, NJ. Generally the mill has one vial, which includes the sample and grinding balls, secured in the clamp and swings back and forth also lateral movements several thousand times per minute. With the swing motion of the vial, the

balls impact against the sample and the end of the vial, so this causes milling and mixing the sample. In this machine the speeds of balls are high (5 m/s). Because of the amplitude (about 5 cm) and speed (about 1200 rpm) of the clamp motion, and consequently the force of the ball's impact is unusually great. So these mills can be considered as high-energy variety.

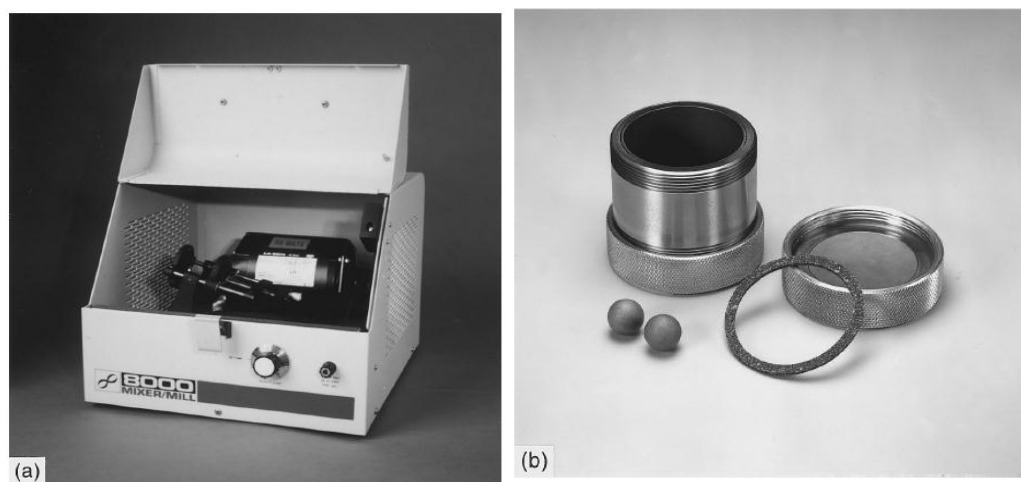


**Figure 2.7:** (a) SPEX 8000 mixer/mill in the assembled condition. (b) Tungsten carbide vial set consisting of the vial, lid, gasket, and balls.

#### 2.2.2.2 Planetary ball mills

Pulverisette is another popular mill for conducting MA, depicted in Figure 2.8a. Here, few hundred grams of the powder can be milled at a time. They are manufactured by Fritsch GmbH in Germany and marketed by Gilson Co., in the US and Canada. The name of the planetary ball mill comes from the planet like movement of the vials.

So the vials are located on a rotating support disk and a special drive mechanism let them to rotate around their own axes. Because of the vials rotating around their own axes, they produce centrifugal force and that produced by the rotating support disk both act on the vial contents, consisting of material to be ground and the grinding balls. Since the vials and the supporting disk are rotating in opposite directions, the centrifugal forces alternately act in like and opposite directions. This conduces to; the grinding balls to hit the inside wall of the vial –which has the friction effect, and that followed by the material being ground and grinding balls lifting off and moving

independently through the inner chamber of the vial and colliding against the opposing inside wall –which is the impact effect, it is depicted in Figure 2.8b.

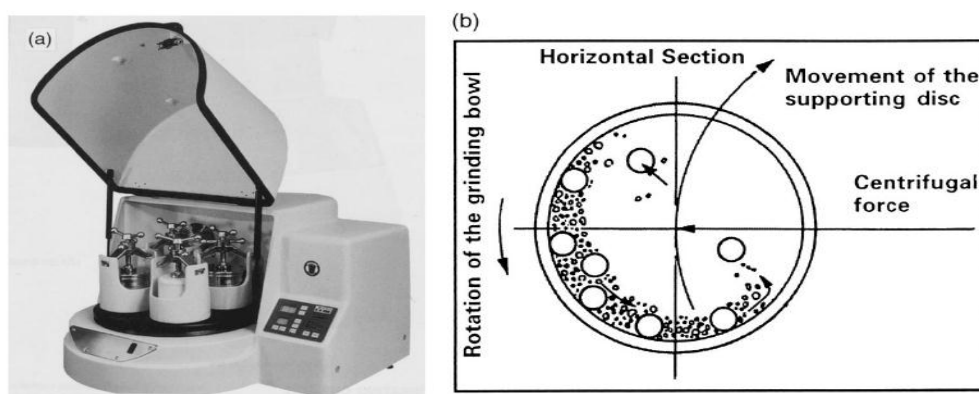


**Figure 2.8:** (a) Fritsch Pulverisette P-5 four station ball mill. (b) Schematic depicting the ball motion inside the ball mill.

In this type of mills, the linear velocity of the balls is higher than in the SPEX mills, the frequency of impacts is much more in the SPEX mills. Whence, comparing to SPEX mills, Fritsch Pulverisette can be considered as lower energy mills.

### 2.2.2.3 Attritor mills

A conventional ball mill contains of a rotating horizontal drum half-filled with small steel balls. The drum rotates the balls drop on the metal powder that is being ground; the rate of grinding increases with the speed of rotation. At high speeds, the centrifugal force acting on the steel balls exceeds the force of gravity, and the balls are pinned to the wall of the drum. So here, the grinding action stops. An attritor which a ball mill capable of generating higher energies: consists of a vertical drum with a series of impellers inside. Set progressively at right angles to each other, the impellers energize the ball charge that cause powder size reduction because of impact between balls, between balls and container wall, and between balls, agitator shaft, and impellers. Some size reduction appears to take place by interparticle collisions and by ball sliding. A powerful motor rotates the impellers, which in turn agitate the steel balls in the drum.

Attritors are the mills in which large quantities of powder e.g. from about 0.5 to 40 kg can be milled at a time, this depicted in Figure 2.9a. If the velocity is going to be



compared with the grinding medium is much lower (approximately 0.5 m/s) than in Fritsch or SPEX mills and so the energy of the attritors is low.

The attritor operation is simple. The powder to be milled is placed in a stationary tank with the grinding media. The mixture is then agitated by a shaft with arms, rotating at a high speed of ~250 rpm. This mechanism depicted in Figure 2.9b. That causes the media to exert both shearing and impact forces on the material. The laboratory attritor works approximately 10 times faster than conventional ball mills.

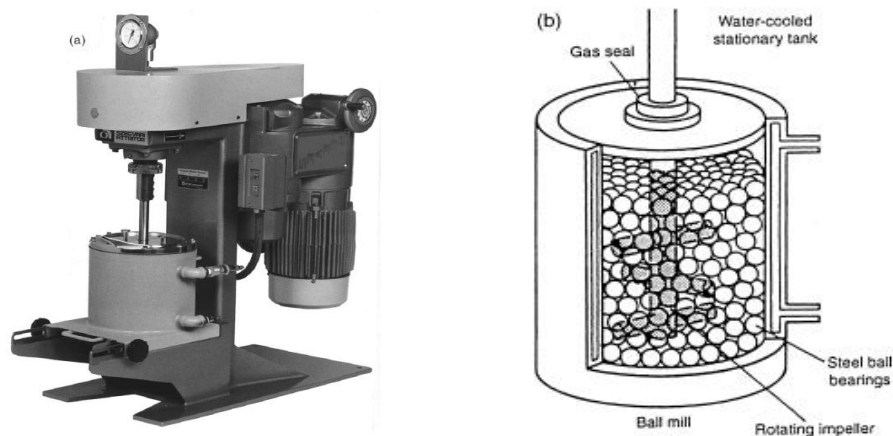


**Figure 2.9:** (a) Model 1-S attritor. (b) Arrangement of rotating arms on a shaft in the attrition ball mill.

### 2.3 Process Variables

Mechanical alloying is a complex process. For optimization of the process, we should take look at the variables that affect mechanical alloying. Some of the important parameters that have an effect on the final constitution of the powder are: milling time, milling speed, type of mill, milling container, type, size, and size distribution of the grinding medium, ball-to-powder weight ratio, extent of filling the vial, process control agent, temperature of milling, milling atmosphere.

But all the process variables that are written above are not completely independent. As an example, the optimum milling time depends on the temperature of milling, type of mill, size of the grinding medium, and ball-to-powder ratio.

### 2.3.1 Type of mill

As described in section 2.2.2, there are a number of different types of mills for conducting MA. These mills differ in their operation speed, capacity, and their ability to control the operation by changing the temperature of milling and the extent of minimizing the contamination of the powders. The suitable mill can be chosen according to the type of powder, the quantity of the powder, and the final constitution required. The SPEX shaker mills are used, more often, for alloy screening purposes. So for large quantities of the powder; Fritsch Pulverisette planetary ball mills or the attritors are used. Typical capacities of the different types of mills are shown in Table 2 [51].

**Table 2.1:** Typical capacities of the different types of mills.

Mill type	Sample weight
Mixer mills	Up to 2 x 20 g
Planetary mills	Up to 4 x 250 g
Attritors	0.5-100 kg
Uni-ball mill	Up to 4 x 2000 g

### 2.3.2 Milling container

One of the parameters in the milling process is the material used for the milling container. This is important by the reason of impact of the grinding medium on the inner walls of the container; some material will be dislodged and get incorporated into the powder. So this situation can contaminate the powder or change the chemistry of the powder. If the material of the grinding vessel is different from that of the powder, then the powder might be contaminated with the grinding vessel material. Or, in case of the materials are same, then the chemistry may be changed unless proper precautions are taken to compensate for the additional amount of the element incorporated into the powder. The grinding vessels' materials are; hardened steel, tool steel, hardened chromium steel, tempered steel, stainless steel, WC-Co, WC- lined steel[52], and bearing steel. Some specific materials are used for specialized purposes; like copper[53], titanium[54], sintered corundum, yttria-stabilized zirconia (YSZ)[55], partially stabilized zirconia + yttria [56, 57], sapphire[58, 59], agate[60-62], hard porcelain,  $\text{Si}_3\text{N}_4$ , [63] and Cu-Be [64 - 68].

Also container shape is an important parameter for milling, especially the internal design of the container. Both of the flat-ended and round-ended SPEX mill containers have been used. According to Beaudry's work, alloying took place at significantly higher rates in the flat-ended container than in the round-ended [69]. The time is needed to reach a constant intensity and shape of the (111) peak in the X-ray diffraction pattern of the Si-Ge mixture was 9 h for the flat-ended vial and 15 h in the round-ended vial.

### **2.3.3 Milling speed**

For obtaining the high energy, the mill rotates fast. So that the energy input would be higher into the powder. Because of the design of the mill, there are some limitations on the maximum speed that could be employed. As an example, in a conventional ball mill increasing the speed of rotation will increase the speed with which the balls move. Above a critical speed, the balls will be pinned to the inner walls of the vial and do not fall down to exert any impact force. Hence, the maximum speed should be below the critical value and the balls can fall down from the maximum height and they can produce the maximum collision energy. There is another limitation to the maximum speed is that at high speeds, the temperature of the vial can be really high. This can be an advantage in some cases where diffusion is required to promote homogenization and/or alloying in the powders. On the other hand, in some cases, increasing the temperature can be a disadvantage, this increased temperature can speed up the transformation process and results in the decomposition of supersaturated solid solutions or other metastable phases formed during milling [70]. Also the high temperatures that generated during the milling may also contaminate the powders. It has been reported that due to the enhanced dynamical recrystallization, while nanocrystal formation, the average crystal size increases and the internal strain decreases at higher milling intensities [71]. The maximum temperature achieved is varying types of mills and the values vary widely.

### **2.3.4 Milling time**

Milling time is one of the most important parameter for milling process. Time is important for reaching a steady state between the fracturing and cold welding of the powder particles. The times can vary with these parameters; the ball-to-powder ratio, the intensity of milling, the type of mill used, and the temperature of milling. These

times have to be decided for each combination of the above parameters and for the particular powder system. If the powder mills more than required then the contamination increases and some undesirable phases can form [72]. The powder should be milled for the required time and not more.

### **2.3.5 Grinding medium**

There are some materials which are generally used for the grinding medium generally such as stainless steel, hardened steel, tool steel, WC-Co, hardened chromium steel, tempered steel, and bearing steel. For getting the enough impact force on the powder from the balls, the density of the grinding medium should be high enough. However, as in the case of the grinding vessel, some special materials are used for the grinding medium and these include copper [53], titanium [73], niobium [74], zirconia ( $\text{ZrO}_2$ ) [75-76], agate [77-78], yttria stabilized zirconia (YSZ) [55], partially stabilized zirconia + yttria [79-80], sapphire [81], silicon nitride ( $\text{Si}_3\text{N}_4$ ) [82], and Cu-Be [83]. To avoid cross contamination, it is better to have the grinding vessel and the grinding medium which are made of the same material as the powder being milled. Another parameter affected on milling efficiency is the size of the grinding medium. Usually, a large size and high density of the grinding medium is useful because the larger weight of the balls will transfer more impact energy to the powder particles. Lu et al. [84] showed that the final character of the powder is dependent upon the size of the grinding medium. As an example, when balls of 15 mm diameter were used to mill the blended elemental Ti-Al powder mixture, a solid solution of aluminum in titanium was formed. Also, when 20 and 25 mm diameter balls were used, only the titanium and aluminum phases occurred, even after a long milling duration.

For promoting the amorphous phase formation, it was offered that using the smaller balls produced intense frictional action. It seems like the soft milling conditions which are: small ball sizes, lower energies, and lower ball-to-powder ratios; seem to favor amorphization or metastable phase formation [73,85-87]. Most of the researchers generally use one size of the grinding medium, there have been few examples when different sized balls have been used in the same investigation [88]. If balls with different diameters are used in the system, it has been predicted according to that the highest collision energy can be obtained [89].

Grinding balls of the same size usage in a round or a flat bottom vial showed to produce tracks. Instead of hitting the end surfaces randomly, the balls roll along a well-defined trajectory. Hence, it is necessary to use several balls, the combination of smaller and larger balls make the motion random [90].

### **2.3.6 Ball-to-powder weight ratio**

The ratio of the weight of the balls to the powder (BPR) may be referred to as charge ratio (CR), which is also an important parameter in the milling process. This variable has been changed by different researchers, in different values; from the lower ratio 1:1[91] to higher ratio 220:1 [92]. Most common ratio is 10:1 is used during the milling of the powder in a small capacity mill, for example SPEX mill. When the capacity changed from small to large, such as an attritor mill, a higher BPR of up to 50:1 or even 100:1 is used. The BPR has a great effect on the time required for reaching a particular phase in the powder that milled. Generally the higher the BPR, the shorter is the time required. For instance, formation of an amorphous phase was procured in a Ti- 33at%Al powder mixture milled in a SPEX mill in 7 h at a BPR of 10:1, in 2 h at a BPR of 50:1 and in 1 h at a BPR of 100:1 [91, 93]. The explanation for this faster milling is; at a high BPR, there is an increase in the weight proportion of the balls, this will increase the number of collisions per time, hence more energy is transferred to the powder particles. Another possibility for the higher energy is due to the fact that the more heat is generated in the mill and this could also affect the constitution of the powder. When the temperature increase becomes substantial, the amorphous phase formed may even crystallized.

In soft conditions (low BPR values, low speeds of rotation) of MA produce metastable phases whereas hard conditions produce the equilibrium phases. This situation was first clearly demonstrated in the Zr-Co system when an amorphous phase was obtained under soft milling conditions, when a mixture of the equilibrium crystalline phases was obtained under hard milling conditions [94]. Some other similar results were also reported for the other alloying systems [53, 85, 87]. For example, at low BPR a metastable cubic phase was formed, while the stable equilibrium tetragonal phase was formed at higher BPR in the mechanically alloyed Cu-In-Ga-Se powder system [53].

### **2.3.7 Extent of filling the vial**

It is necessary that there must be enough space for the balls and the powder particles to move around in the milling container because the alloying among the powder particles occurs due to the impact forces exerted on them. Therefore the vial filling is one of the important factor in MA process. If the quantity of the balls and the powder are loaded in small amounts, the production rate will be quite small. When the quantity is large, then there will not be enough space for the balls to move around and so the energy of the impact becomes less. An optimization for filling of the vial is required; generally about 50% of the vial space will be enough for MA process[72].

### **2.3.8 Milling atmosphere**

The milling atmosphere is also an important parameter for the contamination of the powder. Thus, the powders are milled in containers that have been either evacuated or filled with an inert gas such as helium or argon. Unless if interested in producing nitrides, nitrogen must not be used as an inert gas, because it has been found to react with metal powders, causing the contamination during milling, High- purity argon is the most common atmosphere to prevent oxidation and/or contamination of the powder. It has also been noted that oxidation can be generally prevented in the presence of nitrogen ambient. But as mentioned before, if the powder reactive with nitrogen, this preventing cannot be true the usage of the powders such as titanium or its alloy powders is milled. As an example; it is reported that a Ti-48Al-2W (at %) powder milled in an oxygen atmosphere (20 h of milling) picked up 1.5 wt% oxygen. The same powder milled for the same length of time, in a nitrogen atmosphere, picked up 4.7 wt% oxygen [95].

Also the loading and unloading of the powders into the vial is done in atmosphere-controlled glove boxes. Glove boxes are usually on and again evacuated and refilled with the argon gas. If there is a specific purpose, the different atmospheres can be used during milling. If nitrides are wanted to be produced, nitrogen or ammonia atmospheres have been used [96, 97], and for hydrides hydrogen atmosphere was used [98]. When the air exists in the vial, it has been observed thatt it produces oxides and nitrides in the powder, especially if the powders are reactive in nature.

This is the reason of an intense care has to be taken in the usage of inert atmosphere during milling.

The gaseous atmosphere has an effect on the nature of the final phase. When Cr-Fe powder mixtures were milled in different types of gaseous atmosphere, the constitution of the final powder became different [99]. When the powder was milled in an argon atmosphere, there was no amorphous phase formed and Cr peaks remained in the X-ray diffraction pattern. But when the powder was milled in either air containing argon or nitrogen atmosphere, the powder became amorphous completely. As like that, oxygen was shown to enhance the kinetics of amorphization in the Ni-Nb system [100].

### **2.3.9 Process control agents**

The true alloying among powder particles can take place when a balance is maintained between cold welding and fracturing of particles. The powder particles get cold-welded to each other, if they are ductile, due to the heavy plastic deformation experienced by them during milling. But, a process control agent (PCA) is added to the powder mixture during milling to reduce the effect of cold welding. This PCA can also be referred as lubricant or surfactant. The PCAs can be solids, liquids, or gases. They are mostly organic compounds, which behave as surface-active agents. The PCA adsorbs on the surface of the powder particles and minimizes cold welding between powder particles. So that hinders agglomeration. The surface-active agents adsorbed on particle surfaces interfere with cold welding and lower the surface tension of the solid material. A wide range of PCAs has been used in practice about 1-5 wt% of the total powder charge. The most important of the PCAs are stearic acid, hexane, methanol, and ethanol [101].

The greater parts of these compounds decompose during milling, interact with the powder and form compounds, and these get incorporated in the form of inclusions and/or dispersoids into the powder particles during milling. Because of this; carbohydrates (contains hydrogen, carbon, and oxygen) and hydrocarbons (contains hydrogen and carbon) are likely to introduce carbon and/or oxygen into the powder particles resulting in the formation of carbides and oxides which are uniformly dispersed in the matrix. These are not necessarily harmful to the alloy system since

they can contribute to dispersion strengthening of the material resulting in increased strength and higher hardness [102].

The PCAs affect the final phase formation, changing the solid solubility levels [103], modifying the glass-forming range [103-105], and altering the contamination levels.

Lee and Kwun [106] worked on the effects of the nature and quantity of PCA on the constitution of mechanically alloyed Ti-48at.%Al powders. They observed that an amorphous phase formed after milling for 300 h without a PCA, and a metastable FCC phase formed after milling for 500 h. On the other hand, if 0.3 wt% methanol was used as a PCA, a metastable disordered  $Ti_3Al$  phase formed after 300 h of milling and an amorphous phase after 1000 h. Also, when 3 ml of benzene was used as a PCA, a metastable FCC phase formed after milling for 1000 h. From these results they concluded that the formation of the metastable FCC phase is because of atomic penetration into the interstitial sites of the lattice. Also the activation energy for crystallization of the amorphous phase increases (from 281 kJ/mol without a PCA to 411 kJ/mol when 3 wt% methanol was used) as the number of impurity atoms, especially oxygen, in the PCA increases.

Choosing the suitable PCA for milling depends on the nature of the powder which is going to be being milled and the purity of the final product desired. The nature and amount of PCA used during milling determine the final powder particle size and powder yield. In point of fact, the way of how to determine the effectiveness of the PCA is to determine the powder yield after MA. Basically, if the powder yield is high, the PCA is effective. If the powder yield is not as high as desired, then either the amount of PCA used is not sufficient, or the PCA that used is not the right one. It has been shown that 50% of the powder after milling of 15 h, was only be recovered when the 2 wt % polyethylene glycol as a PCA was used, while 100% of the powder was almost be recovered when the steric acid was used [107].

There is not any universal PCA for every system. The amount of the PCA is related to the (a) cold welding characteristics of the powder particles, (b) amount of the powder and grinding medium, and (c) thermal and chemical stability of the PCA used. The powder particle size is liable to increase whether the weight proportion of the PCA to the powder is below a critical value, and the particle size tends to decrease above this value. While choosing the right PCA, the possible interactions between the metal and the components in the PCA have to be analysed. For more



information of the role of PCAs in the milling of Al-Cu powder mixtures is presented in Ref. [108].

### **2.3.10 Temperature of milling**

The temperature of milling is playing role in deciding the constitution of the milled powder. Diffusion processes are involved in the formation of alloy phases irrespective of if the final product phase is a solid solution, nanostructure, intermetallic, or an amorphous phase, it may be expected that the milling temperature has an effect in any alloy system.

There is not much investigations reported about the temperature of milling has been intentionally varied. This varying temperature was done by either dripping liquid nitrogen on the milling container to lower the temperature or electrically heating the milling vial to increase the temperature of milling. These investigations were studied the effect of milling temperature on the variation in solid solubility levels, and to determine if an amorphous phase or a nanocrystalline structure forms at different temperatures. During the formation of nanocrystals, it was shown that the root mean square (rms) strain in the material was lower and the grain size larger for materials milled at higher temperatures [109]. At higher milling temperatures; extent of solid solubility was reported to decrease. For instance, while the planetary ball milling of a Cu-37at%Ag powder mixture, it was noted that a mixture of an amorphous and crystalline (supersaturated solid solution) phases was obtained on milling at room temperature; instead, only a Cu-8at%Ag solid solution was obtained on milling the powder at 200°C [110]. Similar results were also reported by others in the Cu-Ag [111], Zr-Al [112], and Ni-Ag [113] alloy systems and were explained on the basis of the increased diffusivity and equilibration effects at higher temperatures of milling.



### 3 ELECTROCHEMICAL HYDROGEN STORAGE

A brief information about the electrochemical hydrogen storage will be mentioned in this chapter. The electrochemical characterization techniques which were used in the experimental part of this study such as Constant-Current (CC) measurements, Galvanostatic Intermittent Titration Technique (GITT) and Electrochemical Impedance Spectroscopy (EIS) will be introduced in this chapter. Here the details are going to be given about experimental electrochemical setup and the experimental details of alloy synthesis by casting and ball-milling and of electrode preparation for electrochemical measurements.

#### 3.1 Electrochemical Hydrogen Storage

##### 3.1.1 Relevant reactions

There are two ways to load hydrogen to the storage material: via the gas-phase, or electrochemical hydrogen storage, which takes place in a battery. The reactions are listed below and schematized in Figure 3.1. The relevant electrode reactions such as the charge transfer and hydrogen recombination reactions are indicated at their appropriate locations with the same labels as used in the text.

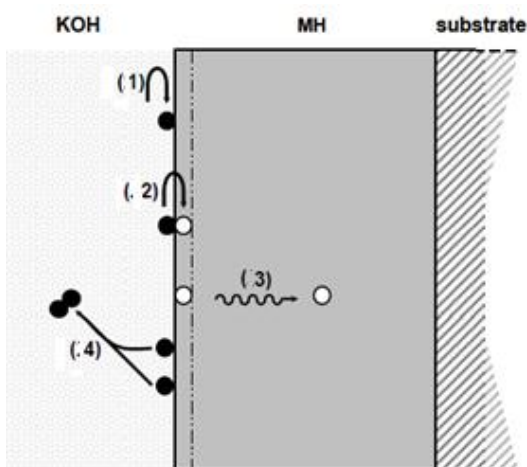
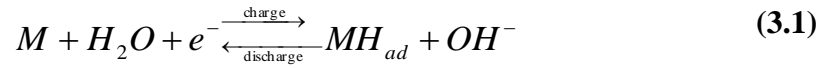


**Figure 3.1:** Schematic drawing of a planar MH electrode.

First step



This is called as Volmer reaction; here water is reduced to hydroxyl ions and hydrogen atoms that are adsorbed at the materials' surface. This adsorbed hydrogen is absorbed inside the material in the layer just below the surface, forming subsurface hydrogen or  $H_{ss}$



From the subsurface layer, the hydrogen then diffuses further into the bulk of the material, becoming absorbed hydrogen  $H_{abs}$

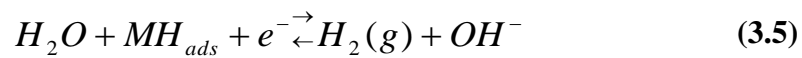


The adsorbed hydrogen atoms can also be recombined to form hydrogen gas in the so-called Tafel reaction



Hydrogen gas can also be formed in a reaction involving electron transfer, the so-called

Heyrovsky reaction



The contribution of this reaction is generally considered to be negligible compared to the Tafel mechanism [114].

### 3.2 Constant-Current (CC) measurements

In the galvanostatic experiment, a predetermined constant current is applied to the working electrode (WE) consisting of the material to be studied and the resulting potential of the WE versus a reference electrode (RE) is measured. A simplified scheme of the experimental setup is shown in Figure 3.2. This type of experiment is

also called chronopotentiometry as it records the potential over time. Figure 3.3 shows the possible response of the working electrode potential to an applied constant charging current at  $t=0$ . In this example, there is one well-defined potential region where the hydrogen storage reactions ((3.1)-(3.3)) take place in region I.

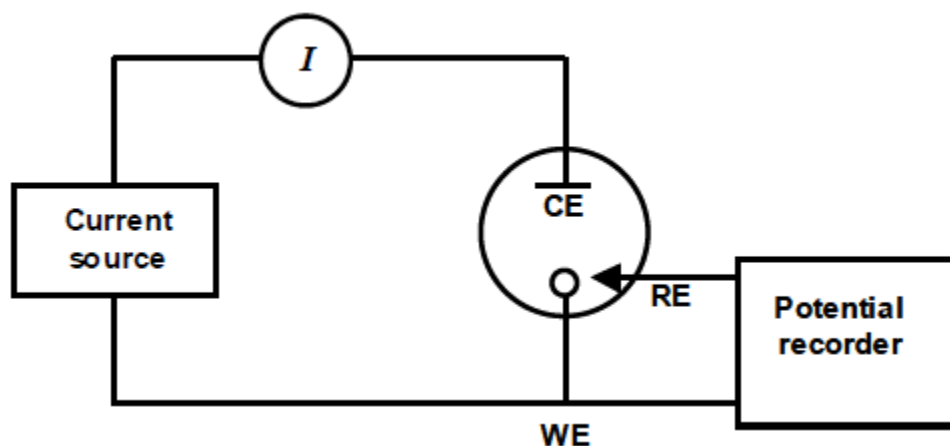


**Figure 3.2:** Schematic overview of the electrochemical experimental setup.

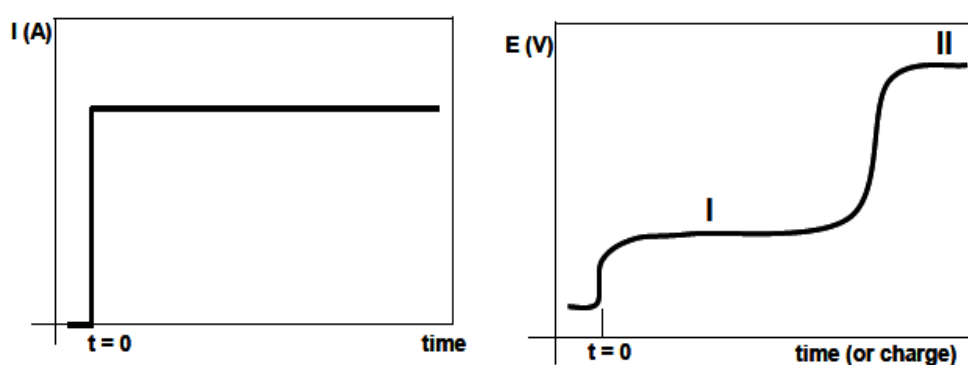


**Figure 3.3:** An applied constant current starting at  $t = 0$  (left) and a possible potential response of the working electrode during charge (right)

The applied current drives reactions involving electron transfer at the electrode surface; reaction (3.1). In the charge-transfer reaction that 1 transferred electron corresponds to 1 stored H atom. The amount of absorbed hydrogen can be determined by integrating the current over the time. Therefore, electrochemically determined capacities are most often reported in mAh/g. For conversion to weight%, the following relation is used:

$$1mAh = 10^{-3} C / s * 3600s = 3.6C \cong \frac{3.6C}{96485C / mol} * 1.008g / mol = 3.76 * 10^{-5} g$$

Thus, 1 mAh/g is equivalent to 0.00376 wt.%, or 1 wt.% corresponds to 265 mAh/g. Because currents can be straightly measured, electrochemical determination of the storage capacity is much more precise than by gas-phase measurements, especially during discharge. When the material approaches its maximum hydrogen content, the potential starts to change towards that of region II. In this region, the storage reactions (3.2) and (3.3) no longer take place and the formation of adsorbed hydrogen is exclusively followed by recombination of the hydrogen atoms to H<sub>2</sub> gas, can be seen in reaction (3.4). So, near the end of the charging step, some inaccuracy is introduced in the amount of absorbed hydrogen, as not all the transferred charge is converted to absorbed hydrogen.

### 3.3 Galvanostatic Intermittent Titration Technique (GITT)

To obtain equilibrium data of an electrochemical system, in this case a hydride-forming material, a technique most often abbreviated as GITT is used. In order to obtain equilibrium potentials, there should not flow any current through the system. Hence, short current pulses are alternated with relaxation periods as is shown in Figure 3.4. When a short current pulse is applied, reaction (3.1) will proceed, storing a small amount of hydrogen. As a consequence, the equilibrium potential after relaxation will differ from the one measured at  $t = 0$ . The current pulses and relaxation periods are subsequently repeated until the active material is completely charged with hydrogen. The equilibrium potentials recorded at the end of the relaxation periods each correspond to a certain concentration of hydrogen inside the material and an electrochemical equilibrium curve is obtained, which is equivalent to a pressure composition isotherm.

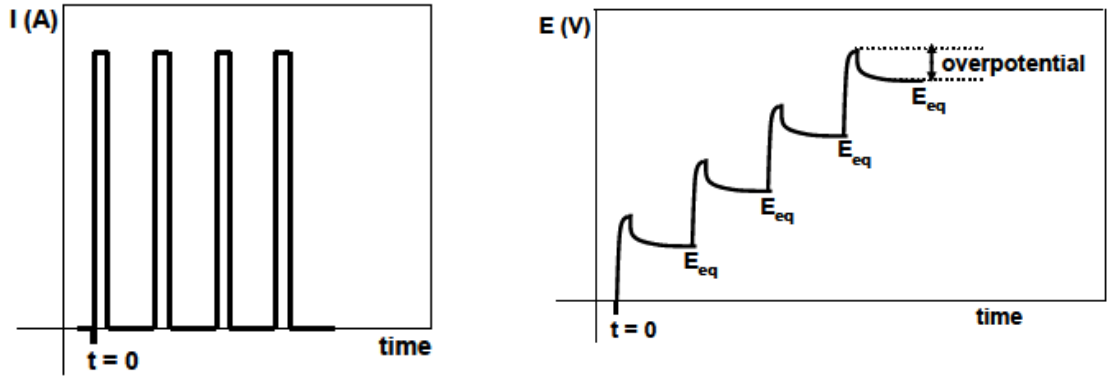


**Figure 3.4:** Alternately applied current pulses and resting periods (left) and the possible potential response of the working electrode (right) during a GITT measurement.

The equilibrium hydrogen pressure and the equilibrium electrode potential can be converted into one another. In general, the chemical potential of hydrogen in a hydride forming material  $\mu_{H,MH}$  is linked to that of hydrogen in the gas-phase ( $\mu_{H_2,g}$ ) [115] via

$$\mu_{H,MH} = \frac{1}{2} \mu_{H_2,g} = \frac{1}{2} \mu_{H_2,g}^0 + \frac{1}{2} RT \ln \left( \frac{P_{H_2}}{P_{ref}} \right) \quad (3.6)$$

$\mu_{H_2,g}^0$  is standard chemical potential of hydrogen gas, that is set to 0 by convention.

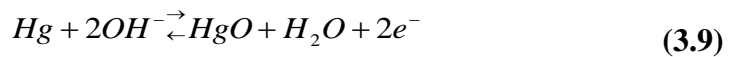
$\mu_{H,MH}$  is linked to the electrode potential by [116]

$$\mu_{H,MH} = -FE_{MH}^{eq} \quad (3.7)$$

Here  $F$  is Faraday's constant (96485.3 C/mol) and  $E_{MH}^{eq}$  is expressed versus the standard hydrogen electrode (SHE)



This is in a 1M acidic solution. In alkaline media, the working electrode potential is monitored versus an Hg/HgO reference electrode. The Hg/HgO redox couple in an alkaline solution is represented,



At 1M concentration of  $OH^-$ , this reaction has a potential vs. SHE of +98 mV [117].

The hydrogen electrode in alkaline medium;



The equilibrium potential of this redox reaction has the same pH dependence as the Hg/HgO couple and the potential vs. SHE is  $-0.828$  V at pH 14 [118]. Hence, the potential vs. Hg/HgO that corresponds to 1 bar of  $H_2$  pressure is, within certain concentration limits, independent of the pH at  $-0.926$  V. However, all electrochemical measurements presented in this thesis are done in 6M KOH solution, which is so concentrated that a small correction for the activity coefficients of all involved species has to be made. In the remainder of the work, the following relation will therefore be used.

$$E_{MH}^{eq} = -0.931 - \frac{RT}{2F} \ln \left( \frac{P_{H_2}}{P_{ref}} \right) \quad (3.11)$$

It can be seen in this equation that measuring the potential with mV accuracy enables the determination of the equilibrium pressure to within  $1/30^{\text{th}}$  of a pressure decade, which is a much higher accuracy than that which can be attained in gas-phase experiments.

### 3.4 Electrochemical Impedance Spectroscopy (EIS)

The Electrochemical Impedance Spectroscopy's principle is imposing a small alternating potential ( $E_{ac}$ ) on an electrochemical system in equilibrium at potential  $E_{eq}$  at a certain frequency  $\omega$  and measuring the current response of the system as a result of this perturbation. The amplitude  $E_m$  of the perturbation should be kept small, typically 5 mV, to preserve linearity of the system.

$$E = E_{eq} + E_{ac} = E_{eq} + E_m \sin(\omega t) \quad (3.12)$$

By varying the frequency  $\omega$  over several orders of magnitude (typically between  $10^5$  and  $10^{-3}$  Hz), information can be obtained on the electrochemical reactions (3.1)-(3.4). If the amplitude  $E_m$  is kept small, the response of the resulting current  $i_{ac}$  will be linear.



For a pure resistance R,  $E = iR$  and the resulting current is given by

$$i_{ac} = \frac{E_{ac}}{R} = \frac{E_m}{R} \sin(\omega t) \quad (3.13)$$

So the impedance Z is defined as

$$Z = \frac{E_{ac}}{i_{ac}} = R \quad (3.14)$$

For a capacitor C, the current response  $i_c$  to an alternating potential signal is given by

$$i_c = C \frac{dE}{dt} = i_{ac} = CE_m \omega \cos(\omega t) = CE_m \omega \sin(\omega t + \pi/2). \quad (3.15)$$

It is clear that the current response for a capacitor is phase shifted by  $90^\circ$  with respect to the applied potential signal. To take this into account, complex impedance is defined, consisting of a real and imaginary part. The potential E is now written as

$$E = E_{eq} + E_{ac} = E_{eq} + E_m e^{(j\omega t)} \quad (3.16)$$

Where  $j = \sqrt{-1}$  and  $e^{(j\omega t)} = \cos(\omega t) + j\sin(\omega t)$ . So the impedance

$$Z_C = \frac{E_{ac}}{i_{ac}} = \frac{E_m e^{(j\omega t)}}{CE_m j \omega e^{(j\omega t)}} = \frac{1}{j\omega C} = -\frac{j}{\omega C}. \quad (3.17)$$

When a redox reaction takes place at an electrode/electrolyte interface, the total current is the sum of the double layer charging current  $i_{dl}$  and a Faradaic current  $i_{Far}$  which corresponds to the charge transfer reaction (3.1) yielding

$$i_{tot} = i_{dl} + i_{Far} = C_{dl} \frac{dE}{dt} + i_{Far} \quad (3.18)$$

The impedance  $Z_{Far}$  associated with this reaction is the charge-transfer resistance  $R_{ct}$ . The addition of two currents is equivalent to putting their resistances in parallel, the total impedance

$$Z_{tot} = \left( \frac{1}{Z_C} + \frac{1}{Z_{reaction}} \right)^{-1} = \left( j\omega C_{dl} + \frac{1}{R_{ct}} \right)^{-1} = \frac{R_{ct} (1 - j\omega C_{dl} R_{ct})}{1 + \omega^2 C_{dl}^2 R_{ct}^2} \quad (3.19)$$

Usually, the results of an impedance measurement are depicted as an impedance spectrum, where  $-Z_{Im}$  is plotted versus  $Z_{Re}$  for each value of  $\omega$ , which is also known

as a Nyquist plot. When the impedance is described and plotted in this way, it has the shape of a semicircle. However, in a real electrochemical setup, there will always be a small ohmic resistance  $R_s$  of the electrolyte solution in series with the two parallel impedances of the double layer and the charge transfer resistance. This shifts the semicircle along the real axis over a distance corresponding to  $R_s$ . An electrochemical system can thus be translated to an equivalent electronic circuit, which in this case consists of a resistance (=electrolyte) arranged in series with a parallel arrangement of a capacitor (= electrical double layer) and a resistance (= charge transfer reaction). The circuit and resulting Nyquist plot are shown in Figure 3.5.

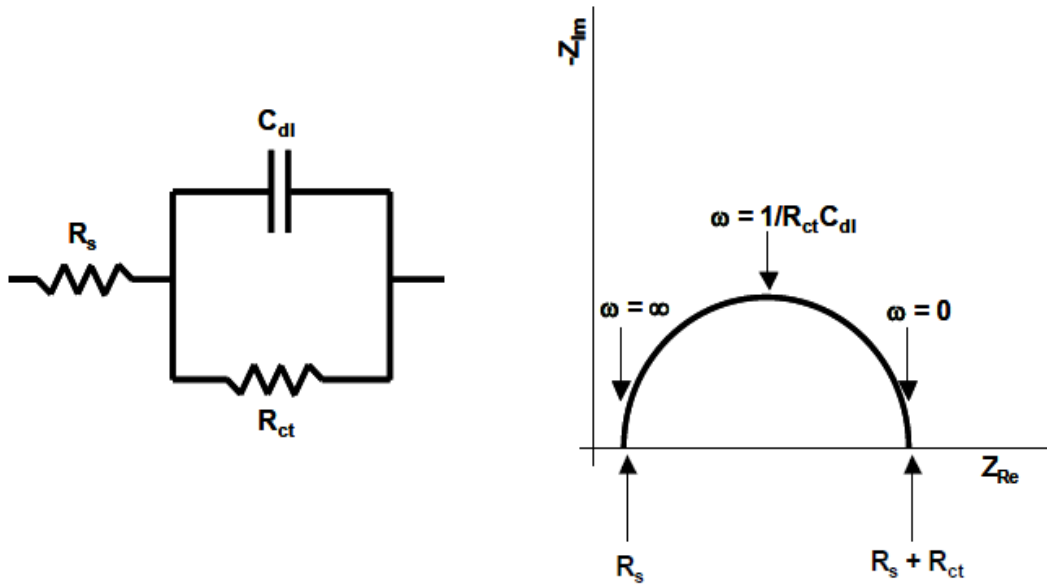


**Figure 3.5:** Equivalent circuit representing an electrode immersed in an electrolyte where a reaction takes place at the electrode/electrolyte interface and the resulting Nyquist plot.

Apart from the charge transfer reaction, bulk diffusion of hydrogen will also play a role in the electrochemical response of a practical system. Semi-infinite diffusion of an active species can be described by a Warburg element (W). Using Fick's laws, the Warburg diffusion element can be described as follows [119].

$$W = \sigma \frac{1}{\sqrt{\omega}} - j\sigma \frac{1}{\sqrt{\omega}} \quad (3.20)$$

The constant  $\sigma$  is given by

$$\sigma = \frac{RT}{n^2 F^2 \sqrt{2}} \left( \frac{1}{c_{ox}^{bulk} \sqrt{D_{ox}}} + \frac{1}{c_{red}^{bulk} \sqrt{D_{red}}} \right) \quad (3.21)$$

Where the subscripts ox and red stand for the oxidized and reduced form of the species, respectively,  $c_{bulk}$  stands for the bulk concentration of the species in the solid and  $D$  denotes the diffusion coefficients in the solid. This equation shows that the real and imaginary part of the Warburg impedance is equal. In a Nyquist plot, this will result in a straight line with a constant phase angle of  $45^\circ$  for all frequencies. It has to be noted, however, that this description holds only for semi-infinite diffusion in a flat plate electrode where only one face is in contact with the electrolyte such as the one shown in Figure 3.1. The value for  $R_{ct}$  as obtained from the Nyquist plot in Figure 3.5 is inversely proportional to the rate constant of the charge transfer reaction in equilibrium. The value of  $W$  is directly linked to the diffusion coefficient of the active species. At high  $\omega$ , the Warburg impedance plays no role as diffusion cannot keep up with the rapid changes in the potential. In this frequency range, the system is under kinetic control. At lower frequencies, diffusion is fast enough and the system can become diffusion-controlled. The complete equivalent circuit including bulk diffusion and the resulting Nyquist plot are shown in Figure 3.6. The equivalent circuit is also known as the Randles equivalent circuit.

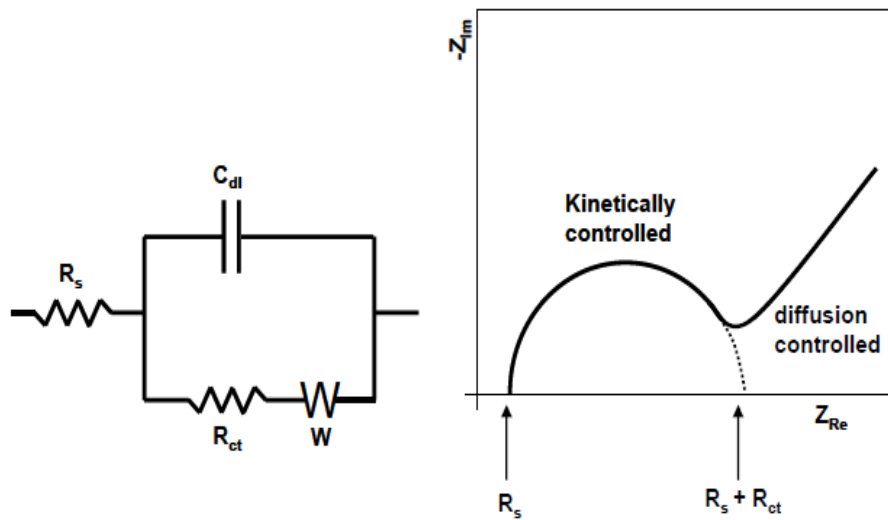


**Figure 3.6.** The Randles equivalent circuit and a typical Nyquist plot showing the Warburg impedance.



## 4 Mg BASED HYDROGEN STORAGE MATERIALS

### 4.1 Existing AB<sub>5</sub>

Alloys derived from LaNi<sub>5</sub> show some very promising properties, including fast and reversible sorption, plateau pressure of a few bars at room temperature and good cycling life. The density for practical purposes is reduced by the packing fraction of LaNi<sub>5</sub> powder, but is still above that of liquid hydrogen. Storage in these intermetallics allows very safe hydrogen handling. But as lanthanum and nickel are large elements, the proportion of hydrogen in LaNi<sub>5</sub>H<sub>x</sub> remains below 2 mass%, while for future mobile applications higher storage capacities are required.

A higher mass density is reachable only with light elements such as magnesium. Magnesium-alloys are very promising in this respect as they can store more than 7 wt. % hydrogen. But its major disadvantages are low kinetics equilibrium a plateau pressure of 1 bar at 300°C. Different processes have been tried to obtain micro- or nanostructured Mg precipitations from metal-organic solutions or high-energy ball milling of Mg have proved successful ways to obtain good charging or discharging kinetics at 150°C, and the thermodynamics evidently are not affected.

Alloying Mg before hydride formation is another approach. During our previous investigations it has been shown that the kinetics of the (de)hydrogenation process can be significantly improved by alloying Mg with other elements, like Ti and Sc. The origin of this favorable effect is the more open fluorite structure, which is formed upon hydriding the Mg-alloys instead of the more-dense rutile structure in the case of pure magnesium. In order to improve the thermodynamic properties of the alloy the ternary additions to the Mg-Ti binary alloys are proposed. However, these Mg alloys are often metastable and special synthesis processes have to be adopted to produce bulk powders.

In this thesis, ternary Mg alloys (Mg-Ti-X) as bulk materials by mechanical alloying are prepared. The as-produced powders will be characterized by X-ray diffraction and SEM. The materials will be (de)hydrided via electrochemical setups. Also the

relationship between the hydrogen storage properties, such as storage capacity, thermodynamic properties, (de)hydrogenation kinetics, reversibility were understood.

## 4.2 Magnesium Based Binary Alloys

In hydrogen storage technology, light weight materials have a critical importance for applications. This property can be achieved by Magnesium based alloys. In a long time period; the extremely poor (de)hydrogenation kinetics of pure Mg have been significantly improved by the discovery of nano-structured alloying materials. Ball milling is embraced to produce storage materials.

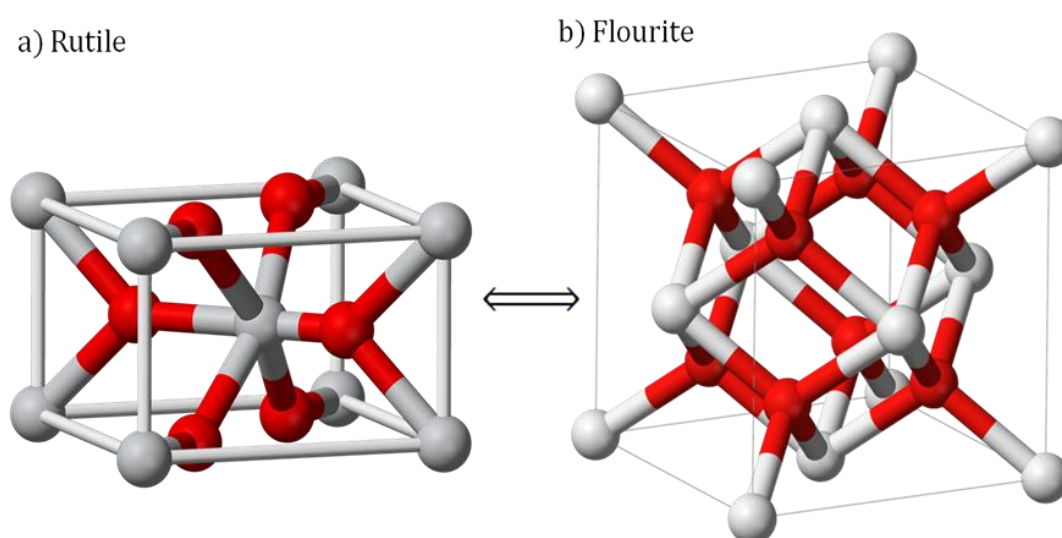


**Figure 4.1:** Rutile  $\text{MgH}_2$  (a) and fluorite  $\text{Mg}_x\text{TM}_{(1-x)}\text{H}_2$

Alloying Mg with transition metals has also a significant impact on the thermodynamics and kinetics of the hydride-formation reaction. In respect to this  $\text{Mg}_2\text{Ni}$  was the first alloy [120 -122]. This alloy has a better performance in terms of thermodynamics and kinetics but the hydrogen content in  $\text{Mg}_2\text{NiH}_4$  is about 3.6wt.%, which is less than half of pure  $\text{MgH}_2$ .

Under standard conditions, as shown in Figure 4.1a ( $\alpha\text{-MgH}_2$ ) magnesium-dihydride has the rutile structure with space group  $P4_2/mnm$  (136); Mg and H atoms are positioned in the 2a and 4f Wyckoff positions, respectively. Each Mg-atom is coordinated octahedrally by H atoms. Mainly, the hydrides of the transition metals in 4<sup>th</sup> and 5<sup>th</sup> row of the 3B to 6B groups crystallize in the fluorite structure ( $\alpha\text{-MgTMH}_2$ ) as shown in Figure 4.1 b) with space group  $Fm\bar{3}m$  (225) and TM atoms in

4a and H atoms in 8c Wyckoff positions. Alloying these transition metals helps to preserve the fluorite structure in  $\text{Mg}_x\text{TM}_{(1-x)}\text{H}_2$ .  $\text{MgH}_2$  has the rutile structure which is denser. So the hydrogen mobility is limited whereas  $\text{Mg}_x\text{TM}_{(1-x)}\text{H}_2$  ( $x < 0.8$ ) has adopted the fluorite structure, which is more open for hydrogen transportation.

In both thin film and bulk form, the hydrogen storage capacity of these fluorite-structured compounds was shown to have a much larger reversible electrochemical storage capacity with respect to Mischmetal-based  $\text{AB}_5$  compounds. Comparing the extracted amount of charge of a fully hydrogenated  $\text{AB}_5$ -type hydride-forming electrode – can be seen in curve (a) in Figure 4.2- with that of a fluorite-stabilized magnesium-based compound can be seen curve (b) in Figure 4.2- reveals that the latter has about four times higher storage capacity. In addition, the rates at which hydrogen can be electrochemically loaded and removed in the fluorite-structured Mg-alloys were substantial, making these fluorite-stabilized materials very interesting.

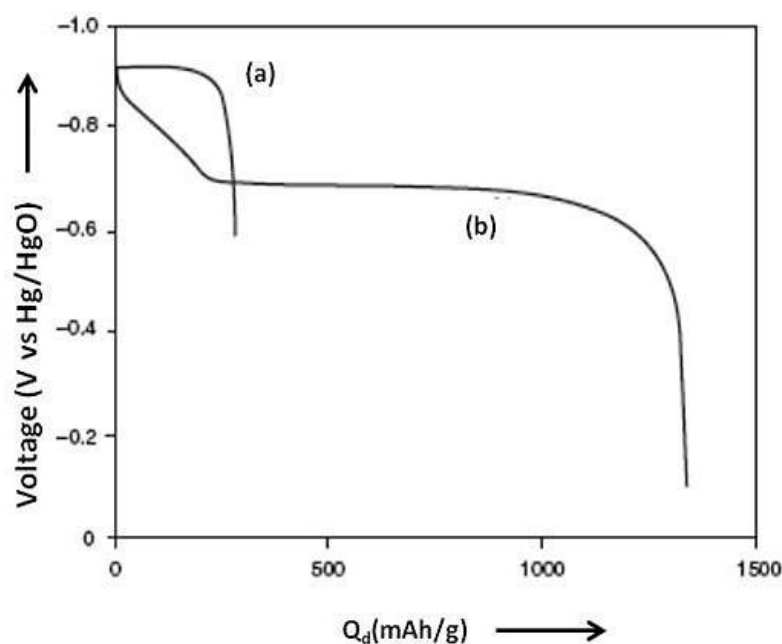


**Figure 4.2:** Comparison between (a)  $\text{AB}_5$  type compound and (b)  $\text{Mg}_{72}\text{Sc}_{28}(\text{Pd}_{0.012}\text{Rh}_{0.012})$ .

#### 4.2.1 Magnesium Scandium alloys

The specific fluorite-type of magnesium-based compounds alloyed with scandium has been studied electrochemically with compositions from 50 to 100 at. %, both in thin film and bulk forms. The thin film electrodes were prepared with a thickness of 200 nm on quartz substrates capped with a 10 nm Pd layer. The bulk powders were prepared through arc melting in a molybdenum crucible  $\text{Mg}_x\text{Sc}_{1-x}\text{Pd}_{0.24}$ . The XRD results of the thin films confirm the formation of Hexagonal Closed Packed (HCP) solid solution irrespective of the composition and this is far from the equilibrium state reported in the phase diagram, where a CsCl type solid solution is found between  $x=50-65$  at.% Mg. Single phase  $\alpha$ -Mg is only formed beyond 80 at.% of Mg presence. On the other hand, the XRD results of bulk powders, confirm the equilibrium phase diagram.

The electrochemical properties of MgSc thin films and bulk materials are very similar. Both materials show similar trends in storage capacity, also the shape of the discharge curves are very similar for the various compositions (Figure 4.3). The maximum storage capacity was reached at a composition of 80 at.% Mg and was 1740 mAh/g for thin films, corresponding to 6.5 wt.% H and 1495 mAh/g corresponding to 5.6 wt.% for bulk materials. The rate capability of the thin films is much better than the bulk materials due to shorter diffusion lengths. In the case of bulk materials, the Pd catalyst is dispersed inside bulk [123, 124].



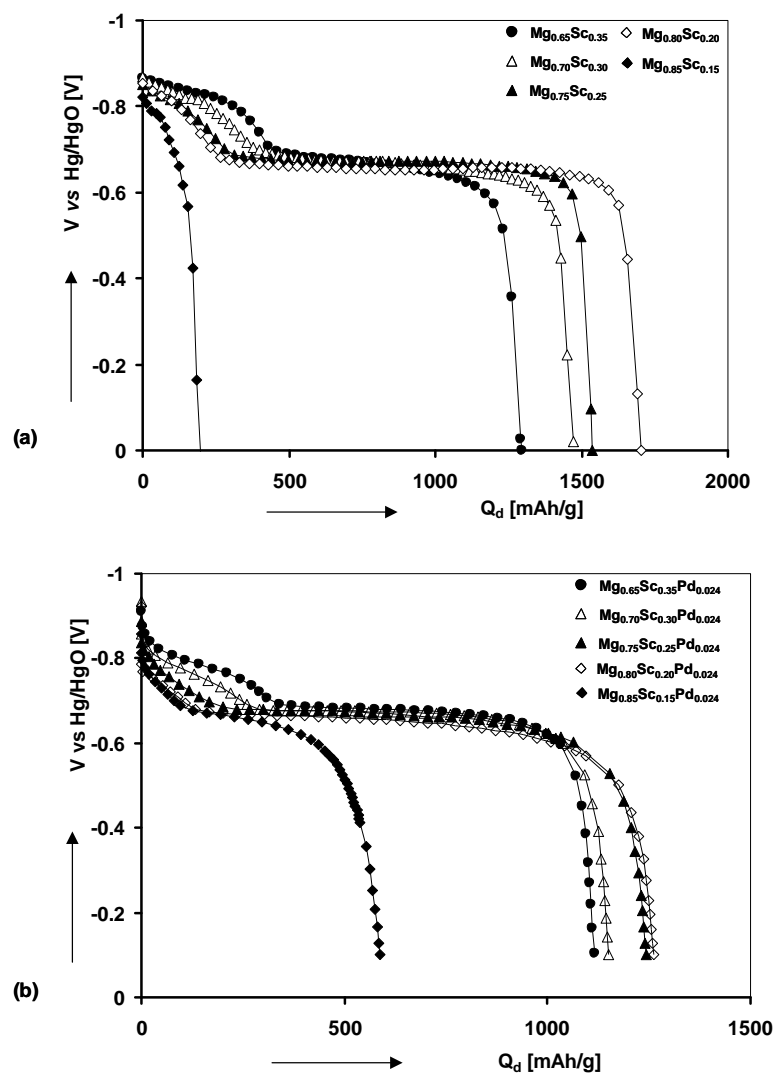


**Figure 4.3:** Galvanostatic discharge curves of: thin films (a) and bulk materials (b); the current density was 1000 mA/g for the thin films and 50 mA/g for the bulk materials.

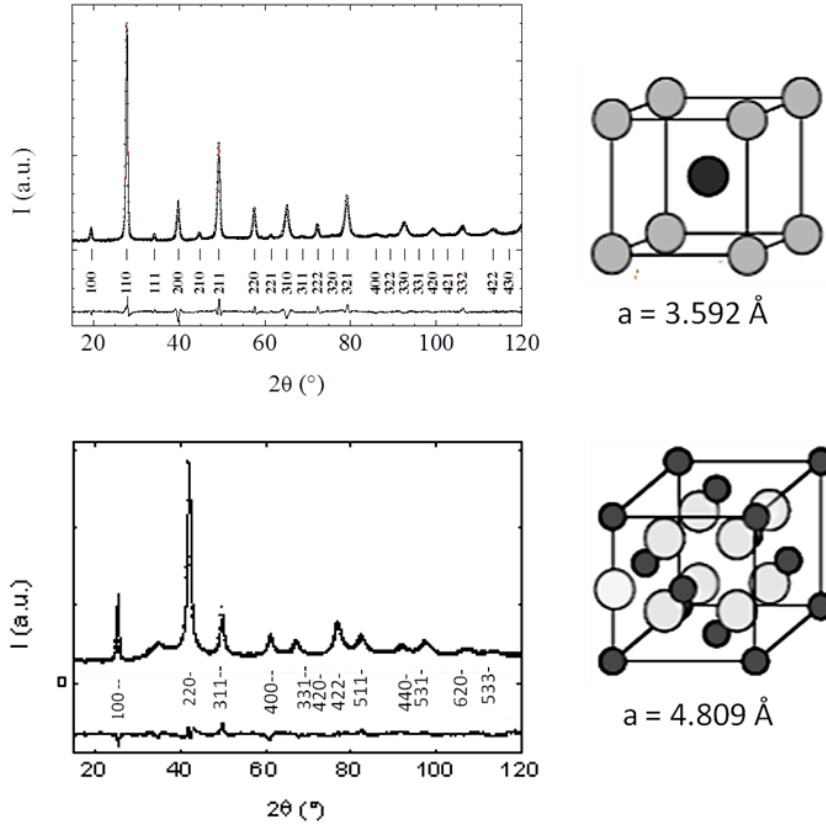


**Figure 4.4:** Neutron diffraction of  $\text{Mg}_{65}\text{Sc}_{35}$  (a) before deuterium loading (b) after deuterium loading.

It was found that the favorable discharge kinetics was retained up to 80 at.% magnesium. The improvement of the (de)hydriding kinetics compared to pure magnesium has been attributed to the more open fluorite structure of scandium-hydride instead of the more compact rutile structure of the conventional magnesium-hydrides. The plateau pressure is not a function of composition and almost equal to the equilibrium pressure of pure  $\text{MgH}_2$ . Diffraction data obtained from the bulk system unambiguously proved that the fully charged hydride is a single-phase fcc-structured hydride and no segregation into  $\text{MgH}_2$  and  $\text{ScH}_2$  has taken place. Two co-existing FCC structures were found in the plateau region. The hydrogen-rich phase (fluorite) is slightly expanded compared to pure  $\text{ScH}_2$ , whereas the hydrogen-poor phase (sphalerite) has a smaller volume than  $\text{ScH}_2$ , in agreement with Vegard's law[5].

Recently, the crystal structure of a palladium-containing  $\text{Mg}_{65}\text{Sc}_{35}$  compound has been studied upon hydrogenation by neutron diffraction [125]. The metallic phase adopts a pseudo-CsCl-type structure. While hydrogenation, the structure changes

from pseudo- CsCl to fcc involving an elongation along the c-axis and shrinkage along the a-axis (see Figure 4.5). Upon deuteration, a two phase domain is subsequently observed between 0.85 and 1.55 D/metal with two hydrides in equilibrium. Above this value, a pressure increase becomes apparent in the isotherm, leading to fully occupied tetrahedral sites and partially filled octahedral sites [126].

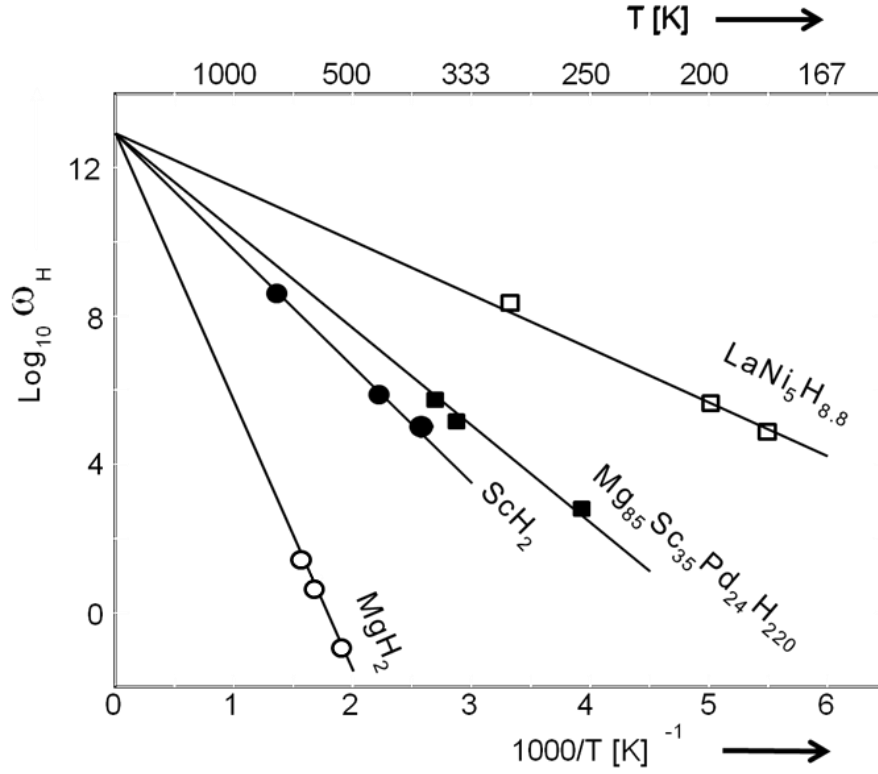


**Figure 4.5:** Relaxation map showing rate  $\omega H$  of H hopping as a function of reciprocal temperature in  $MgH_2$ ,  $ScH_2$ ,  $MgScH_x$ , and  $LaNi_5H_{6.8}$

It has been argued that interstitial hydrogen is highly mobile, due to the large and partially occupied octahedral sites that are favorably influencing the transportation properties. Using proton nuclear magnetic resonance (NMR), the crystallography has proven to be responsible for the beneficial transportation properties of the fluorite-structured magnesium compounds. The frequency hopping rate for the fluorite-structured compounds at the relevant temperatures was found to be many orders of magnitude higher than that for the rutile-structured material. At any given temperature, the rate of  $MgScH_x$  is faster than in  $ScH_2$  and much faster than in the ionic  $MgH_2$ , but still slower than in  $LaNi_5H_{6.8}$  (Figure 4.5) [127].

Pauw et al. did first principle calculations on  $\text{Mg}_x\text{Sc}_{x-1}$  alloys [128]. Figure 4.6 shows that the decrease in the formation enthalpy with increasing Sc-content is more pronounced for the fluorite structure than for the rutile structure. The crossing point of the two curves is located around 20% Sc ( $y=0.20$  as shown in Figure 4.6), that is the exact composition where the electrochemical results showed the maximum rate capability and therefore electrochemical storage capacity. The first principle calculations are in good agreement with these experimental findings.

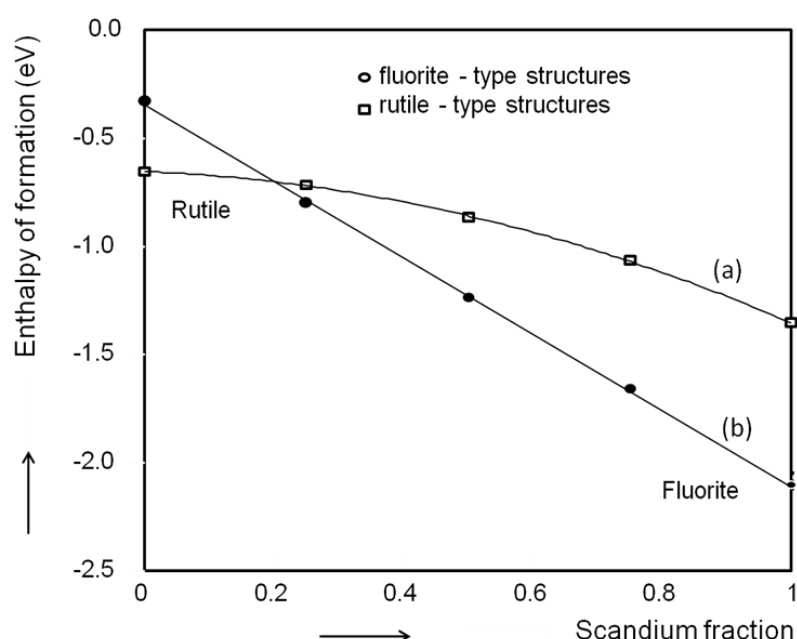


**Figure 4.6:** Enthalpies of formation of  $\text{Mg}_{1-y}\text{Sc}_y\text{H}_2$ . (a) Rutile (b) fluorite.

#### 4.2.2 Magnesium Titanium alloys

Since scandium is rather expensive, attempts to find cheaper substitutes were recently undertaken. Titanium dihydrides are also promising candidates because of having the same fluorite structure as that of scandium dihydride. Experiments performed with  $\text{Mg}_{80}\text{Ti}_{20}$  thin film electrodes indeed showed a similar drastic improvement of the discharge (dehydrogenation) kinetics compared to pure magnesium hydride ( $\text{MgH}_2$ ). A more elaborate study on the Mg–Ti system, can be seen in Figure 4.7, revealed that the composition dependence of the hydrogen storage capacity was quite similar to that of the Mg–Sc system, also showing a maximum capacity around 80 at.% magnesium [129].

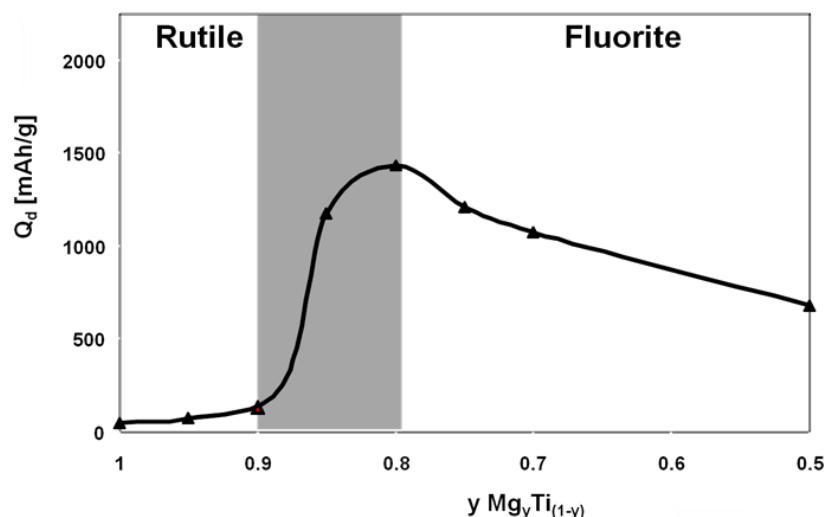


**Figure 4.7:** Electrochemical determined reversible electrochemical capacity at room temperature as function of magnesium content in Mg-Ti thin film electrodes.

The formation enthalpies of metal hydrides in both the rutile and fluorite structure were investigated by Pauw et al. [9]. The calculations showed that the addition of Ti induces a remarkable change in the crystal structure compared to pure  $\text{MgH}_2$ . The formation enthalpy of rutile  $\text{Mg}_{0.50}\text{Ti}_{0.50}\text{H}_2$  is  $-0.421 \text{ eV/H}_2$ , which is  $22.7 \text{ kJ mol}^{-1}$  less negative than pure  $\text{MgH}_2$ . The rutile structure with composition  $\text{Mg}_{0.25}\text{Ti}_{0.75}\text{H}_2$  is also less stable than  $\text{MgH}_2$ , which means that Ti destabilizes the rutile structure over almost the entire compositional range. The formation enthalpy of the fluorite structure shows a tendency towards more negative values over the entire compositional range, the same as for the MgSc system. The fluorite structure becomes the most stable phase around  $y=0.20$ , which is also very similar to MgSc and these theoretical results are also in good agreement with the experimental results. The crystal structure of the resulting hydrides seems to play a crucial role in determining the (de)hydrogenation kinetics for this interesting new class of hydrogen storage materials [9].

In situ electrochemical XRD was carried by Vermeulen et al. to investigate the crystallographic phase transformation during the electrochemical hydrogenation of the MgTi alloys [130]. While hydrogenating  $\text{Mg}_{90}\text{Ti}_{10}$  thin films electrochemically the hexagonal reflections decreases with increasing hydrogen content (Figure 4.8a). Simultaneously, the bct reflections evolve, indicating the formation of body centered tetragonal phase which is the same as for pure  $\text{MgH}_2$ . On the other hand, hydrogenation of  $\text{Mg}_{70}\text{Ti}_{30}$  showed an increase in the FCC phase (Figure 4.8b).

Substantial electrochemical storage capacities of more than 1500 mAh/g have been reported for the Mg-Ti system at room temperature. This corresponds to a reversible hydrogen content of about 6 wt.%. In addition, it has been shown that these meta-stable materials cannot only be produced by thin film evaporation and sputtering techniques but also by mechanical alloying.

Several attempts have been made to produce Mg-Ti alloys by mechanical alloying. Rousselot et al. [131] investigated the phase transformation during electrochemical hydrogenation. The meta-stable HCP  $\text{Mg}_{50}\text{Ti}_{50}$  alloy was formed through mechanical alloying. XRD had been performed on the electrochemically hydrogenated alloy. Upon cycling, the intensity of HCP phase decreases and a new peak arises, which corresponds to hydrided FCC phase. The FCC phase is irreversibly formed and does not disappear after dehydrogenation, instead a slight decrease in the lattice constant was observed upon discharge. Kalisvaart et al. reported the formation of two FCC phases of the Mg-Ti alloy when the milling process was carried out with stearic acid as process control agent [132,133]. Among the two FCC phases only one was concluded to be electrochemically active. The storage capacity of this bulk material was reported to be 500 mAh/g.

Kyoi et al. [134] synthesized Mg-Ti-H compound at 873K in a high pressure anvil cell above 8 GPa by mixing  $\text{MgH}_2$  and  $\text{TiH}_{1.9}$ . The metal atom structure was found to be close to the  $\text{Ca}_7\text{Ge}$  type FCC structure. This is in line with the findings of Vermeulen et al. [130]. It could be concluded from in situ XRD studies that the hydrogen atoms are occupied in the tetrahedral sites.

The Mg-Ti alloy has a positive heat of mixing and must therefore be considered as an immiscible system [135]. The alloy can therefore, in principle, not be synthesized under equilibrium conditions and the only way to produce these meta-stable materials is by making use of non-equilibrium preparation methods. The stability of the meta-stable alloys is still questionable at high temperature and pressure conditions. Liang et al. reported an extended solubility of Ti in Mg, during mechanical alloying of Mg and Ti [136]. In the case of Mg with 20 at.% Ti, about 12.5 at.% Ti is dissolved in the Mg lattice when the mechanical alloying process reaches a stable state, while the rest remains as fine particles in the size of 50–150 nm in diameter. Dissolution of Ti in the Mg lattice causes a decrease in unit cell volume. The phase segregation begins at high temperature and the supersaturated

Mg-Ti alloys starts to decompose at 200 °C. Hydrogenation is an exothermic reaction and enhances the decomposition process.

Srinivasan et al. [137] investigated the structure of bulk magnesium-titanium deuteride  $\text{Mg}_{0.65}\text{Ti}_{0.35}\text{D}_x$  prepared via mechanical alloying and deuterium gas-phase loading at 75 bars and 175°C. The structural analysis was made with XRD, NMR and neutron diffraction. Deuterium loading causes the formation of both interdispersed rutile  $\text{MgD}_2 - \text{TiD}_y$  nano-domains and a separate fluorite  $\text{TiD}_z$  phase. Exchange NMR indicates complete deuterium exchange between the  $\text{MgD}_2$  and  $\text{TiD}_y$  phase within 1 second. Gas phase hydrogenation of the Mg-Ti alloys at higher temperatures increase the risk of phase segregation.

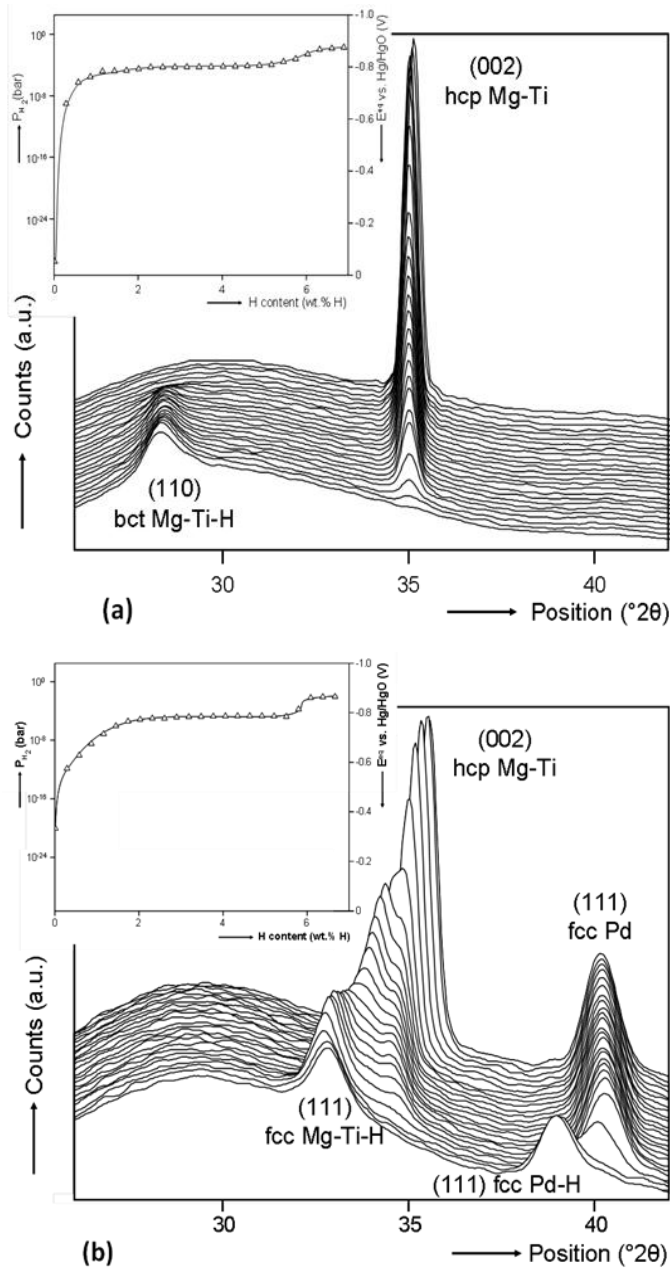


**Figure 4.8:** In-situ electrochemical XRD measurements of  $Mg_{0.90}Ti_{0.10}$  (a) and  $Mg_{0.70}Ti_{0.30}$  (b) during hydrogenation [130].

Even though the kinetics of the fluorite-structured compounds is faster compared to the  $MgH_2$ , the thermodynamic properties are not improved by the addition of these transition metals. For instance, the dehydrogenation enthalpy of  $Mg_x-Sc_{(1-x)}-H_2$  and  $Mg_x-Ti_{(1-x)}-H_2$  is higher compared to  $MgH_2$ . Thus, high temperature is required to dehydrogenate these compounds in case of gas phase loading. However, only Mg-Sc alloys are stable with respect to decomposition into its elemental metallic form. Since scandium is expensive the next optional metal Ti is preferred considering the storage capacity compared to Cr and V. Due to the high stability of the Mg-Ti hydrides and



low thermal stability of Mg-Ti alloy, the addition of a third element into the binary alloys is required to stabilize the host materials and, consequently, to destabilize the alloy hydrides. Careful selection of the third alloying element could assist in improving the thermodynamic properties while maintaining the storage capacities.

### 4.2.3 Mg-based ternary alloys

Increasing the plateau pressure of the metal-hydrogen system can be accomplished by destabilization of the metal hydride. Miedema proposed a mathematical model to calculate the effect on the thermodynamic stability of an additional element(s) to the metallic compound [138,139]. The Miedema model was used by Vermeulen et al. to screen elements that stabilize the metallic Mg-Ti system [140]. Al and Si were selected to destabilize the Mg-Ti alloy, due to their advantageous lightweight mass to maintain the high gravimetric capacity of the overall Mg-Ti alloy. The isothermal curves of the  $\text{Mg}_{0.69}\text{Ti}_{0.21}\text{Al}_{0.10}$  show two plateau regions, a plateau up to 4 wt% H at  $10^{-6}$  bars and a second sloping plateau lies at higher pressures Figure 4.9.

Addition of higher Al content in Mg-Ti lattice leads to decrease in the reversible storage capacity. If only 10 at.% is incorporated in Mg-Ti alloy with a high Mg-content does not seem to significantly affect the reversible capacity. The declining capacity at high Al content could be due to kinetic limitations imposed by the material. Additionally, Si also clearly affects the isotherms compared to Mg-Ti alloys. The length of the first plateau decreases, when  $P_{\text{H}_2}$  increases steeply and reaches soon a sloping plateau. Since Si is heavier than Al, the storage capacity is lower than that of the Al-containing ternary alloys. The occurrence of the second plateau was also observed in other systems, such as  $\text{Mg}_2\text{CuAl}_{0.375}$ ,  $\text{LaCo}_6$ ,  $\text{TiFe}$  and  $\text{NdCo}_5$ . Interestingly, the Mg-Ti-Al-H system shows a plateau near atmospheric pressures and temperature.

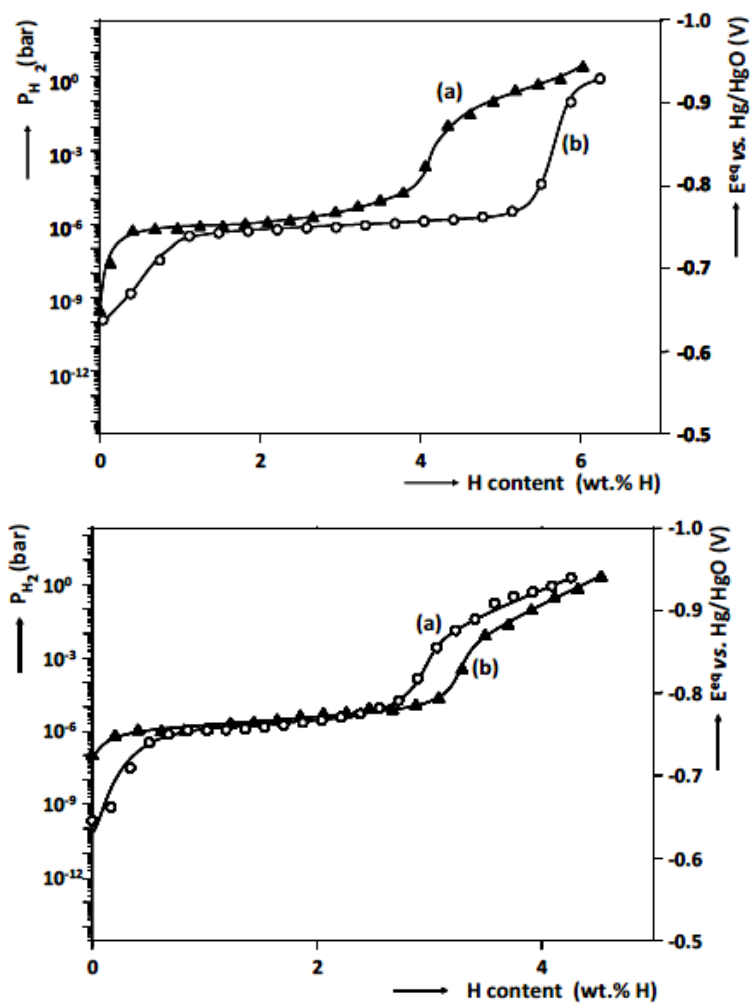


**Figure 4.9:** Electrochemically determined dehydrogenation isotherms of 200 nm; (top a)  $Mg_{0.69}Ti_{0.21}Al_{0.10}$  and (top b)  $Mg_{0.80}Ti_{0.20}$  thin films with a 10 nm Pd top-coat (bottom a)  $Mg_{0.55}Ti_{0.35}Si_{0.10}$  and (bottom b)  $Mg_{0.69}Ti_{0.21}Si_{0.10}$  films capped with 10 nm Pd [140].

## 5 EXPERIMENTAL WORK

### 5.1 Alloy and Electrode Preparation and Characterisation

Mg powder (~325 mesh, 99.8% purity metal basis, Alfa Aesar GmbH&Co, Germany), Ti powder (~325 mesh, 99.98% purity metal basis, Aldrich), Ni powder (~325 mesh, 99.8% purity, Alfa Aesar GmbH&Co, Germany), Si powder (~325 mesh, 99.98% purity metal basis, Aldrich) and Pd powder (~200 mesh, 99.95% purity, Alfa Aesar GmbH&Co, Germany) were weighed and mixed manually in the appropriate ratios before loading into the milling-vial.

High-energy milling was performed in a Spex 8000-230 ball-mill using tungsten-carbide-lined vials with an internal volume of 55 ml. Ball-to-powder (BTP) ratio is 30:1 for the system. Milling was done for intervals of 60 minutes to avoid overheating of the vials. After each interval, the vials were checked for coldwelding and scraped before continuing milling. The Spex 8000 - 230 ball mill was installed inside an Ar-flushed glove box and all powder handling was done under this inert atmosphere. Prior to electrochemical testing, the samples were activated by milling for 120 minutes with 5 at.% Pd powder, which acts as a catalyst.

X-Ray Diffraction analysis (XRD) was used to monitor the progress of the milling process which performed by XRD analysis with a Bruker Enduar D4 diffractometer using CuK $\alpha$  radiation at room temperature in the 2 theta ranges from 20° to 90° with a step size of 0.02° and counting time per step of 1 s.

Morphology changes of the powder materials annealed at different compositions were investigated by scanning electron microscopy using a Quanta 3D FEG instrument (FEI Company).

Electrochemical measurements were carried out in conventional thermostated three electrode cells at 25 °C. The cells containing 6M KOH aqueous electrolyte and the potential of the working electrode was measured versus a Pb-free Hg/HgO (6M KOH) reference electrode from Koslow Scientific Company, USA. Unless stated otherwise, all potential values are given versus this reference. Galvanostatic

measurements were performed using a Maccor M2300 battery tester (Maccor, Tulsa, USA).

To make a test electrode, the ingot is filled down to small flakes and the fraction  $<50$  micrometers is mixed with Ni or Ag powder, pressed into a small pellet and fixed onto a metal rod (also Ni or Ag) by means of a shrink sleeve.

Instead of melting the constituent metals to form an alloy, other preparation methods are also used in this study. Ball-milling is a non-equilibrium room-temperature technique to synthesize alloys from elements that are not miscible by standard methods. In the present work, Spex 8000 shaker mill has been used; depicted in Figure 5.1.



**Figure 5.1:** A Spex 8000M shaker mill.

In the Spex shaker mill, the vial makes both left-to-right and back-and-forth motion, inducing an extremely chaotic movement of the powder and balls inside the vial. The rotation speed of the electric engine is very high (at 1425 rpm) which makes the milling process highly energetic.

A picture of the experimental electrochemical setup is shown in Figure 5.2. All electrochemical measurements described in this study were performed using this 3-electrode setup consisting of a working electrode (bottom right), a counter electrode

(left) and a Pb-free Hg/HgO reference electrode (top right) [141]. The experimental setup is continuously flushed with Ar gas to remove any oxygen that is dissolved in the electrolyte. This is necessary because of the oxygen reduction reaction given in reaction 5.1.



As can be seen oxygen consumes electrons that can be supplied either by an applied current during charging or by oxidation of the metal hydride during discharge or a resting period. This will lead to overestimation of the absorption capacity and underestimation of the discharge capacity in an electrochemical experiment.

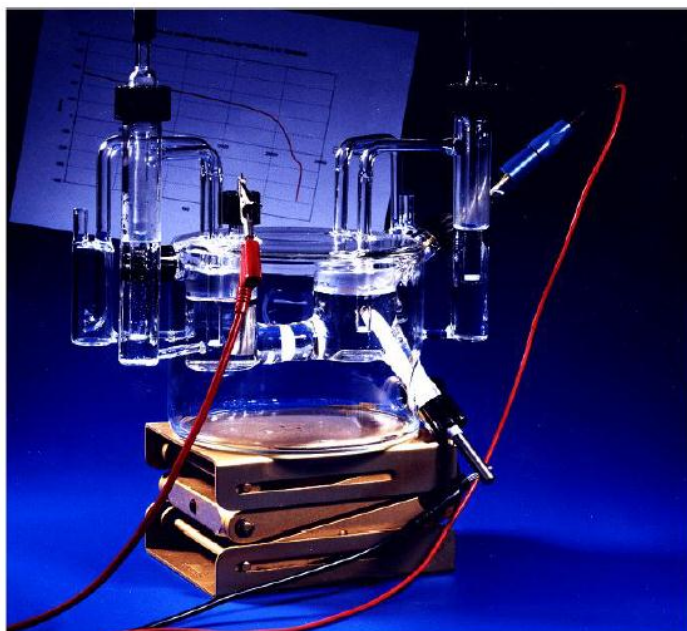


**Figure 5.2:** The experimental setup used for electrochemical measurements.



## 6 RESULTS AND DISCUSSION

### 6.1 Results

Figure 6.1 shows the X-Ray diffraction patterns of  $\text{Mg}_{0.70}\text{Ti}_{0.30}$  for two different milling time. The contamination due to tungsten carbide milling media was not observed in XRD patterns. The Magnesium reflections shift towards higher angle and the Titanium reflections decrease in the intensity during the milling process. Figure 6.1 shows also the shifts which was observed with an increasing milling time. Mg is a Hexagonal Closed Packed (HCP) metal with higher lattice constant ( $a=3.20$  Å;  $c=5.21$  Å) and Ti is also HCP metal with lower lattice constant ( $a=2.95$  Å;  $c=4.68$  Å). The molar volumes of Mg and Ti are  $14.00$  and  $10.64$   $\text{cm}^3/\text{mol}$ , respectively.

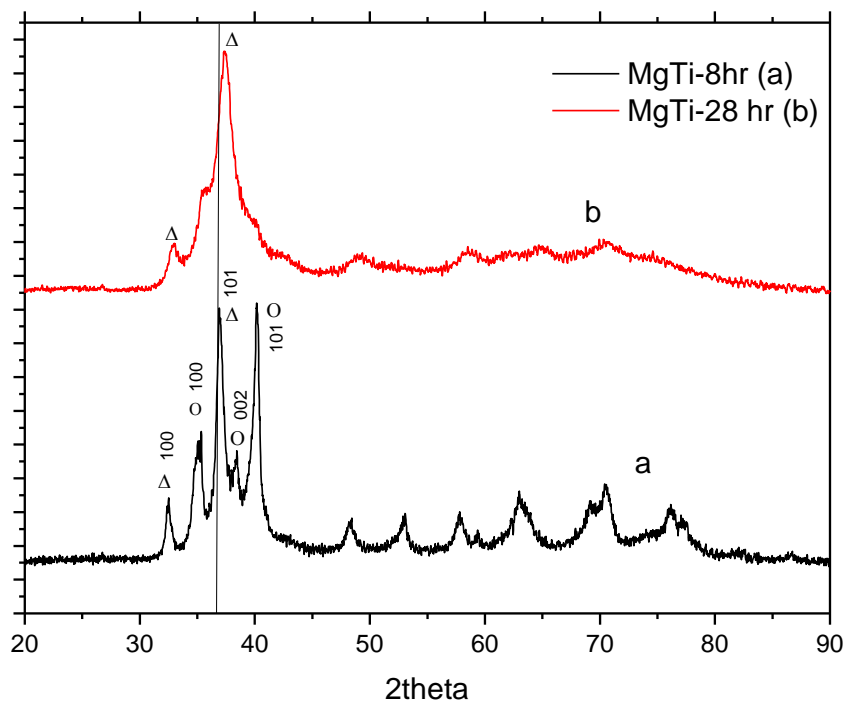


**Figure 6.1:** XRD patterns of  $\text{Mg}_{0.70}\text{Ti}_{0.30}$  ( $\Delta$  indicates Mg, O indicates Ti).

The shift is ascribed due to the fact that Ti is having lower molar volume compared to Mg. The lattice of the Mg is getting smaller with Ti inclusion. It has been observed that the shifts occur up to 28 hours which means there is not much difference in the lattice parameters. After 28 hours Ti peak becomes invisible. The reason of this is due to the saturation level attained in the mechanical alloying process, upon milling will not change the crystal lattice.

An attempt has been made to calculate the lattice parameter. The lattice parameters  $a$  and  $c$  of this material are 3.141 Å and 5.02 Å, respectively.

The SEM figures of Mg-Ti alloy are shown in Figure 6.2. The mean particle size of the alloy lies between ~20-50 µm. The larger agglomerates shown in the figure are due to coldwelding of the smaller fractured materials.

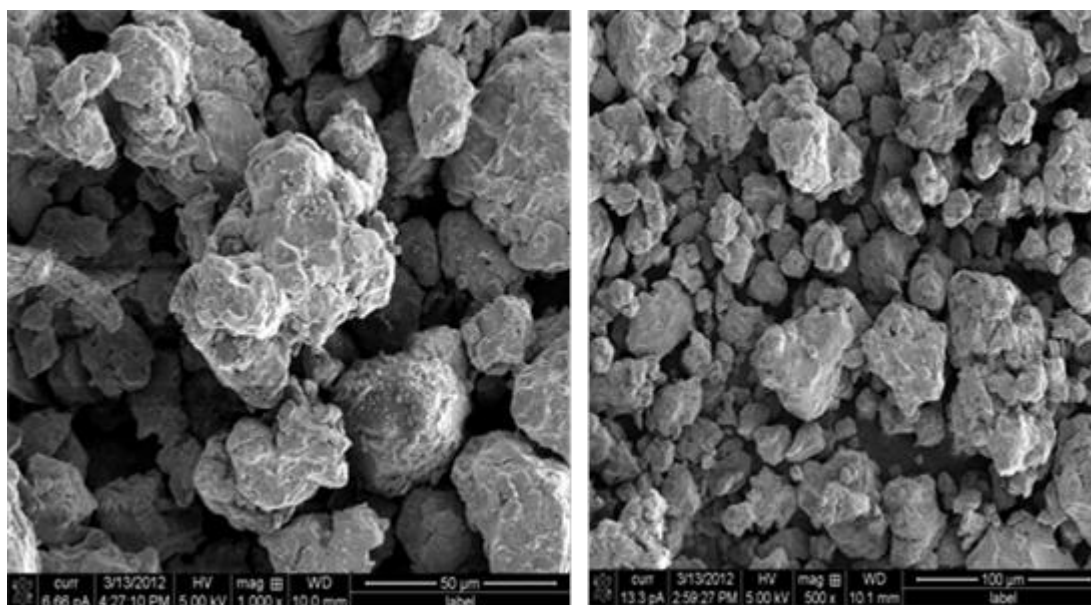


**Figure 6.2:** SEM micrographs of  $\text{Mg}_{0.70}\text{Ti}_{0.30}$  milled for 28 hours.

As the details given in section 4, the alloys are milled with 5 at. % of Pd for 2 hours. The Pd particles on the top of the Mg particles inhibits the formation of  $\text{Mg}(\text{OH})_2$  and the Pd particles make dissociation of the water molecules easier.

The Figure 6.3 shows the electrochemical charge and discharge graph of the  $\text{Mg}_{0.70}\text{Ti}_{0.30}$  alloy. Charging means hydrogenation and discharging means dehydrogenation for the alloy. The curve (a) shows the hydrogenation reaction. The pattern contains two plateau regions. The plateau with higher potential (first plateau) corresponds to more stable hydrogen region. The first plateau is due to the



hydrogenation of Ti rich sites in the alloy. The second plateau is due to the hydrogenation of Mg rich sites. The second plateau ends with the hydrogen evolution reaction (HER) where the material reaches the maximum capacity. Upon applying constant current leads the recombination reaction and subsequent formation of the  $H_2$  at the surface of the electrode. The electrochemical capacity of the alloy is the point where the alloy reaches HER. The theoretical capacity is calculated by considering H/M ratio as 2, where M is Mg and Ti. Theoretical capacity of this material is 6.04 wt.% which is equivalent to 1600 mAh/g, calculated from the unit conversion in Section 3.2.

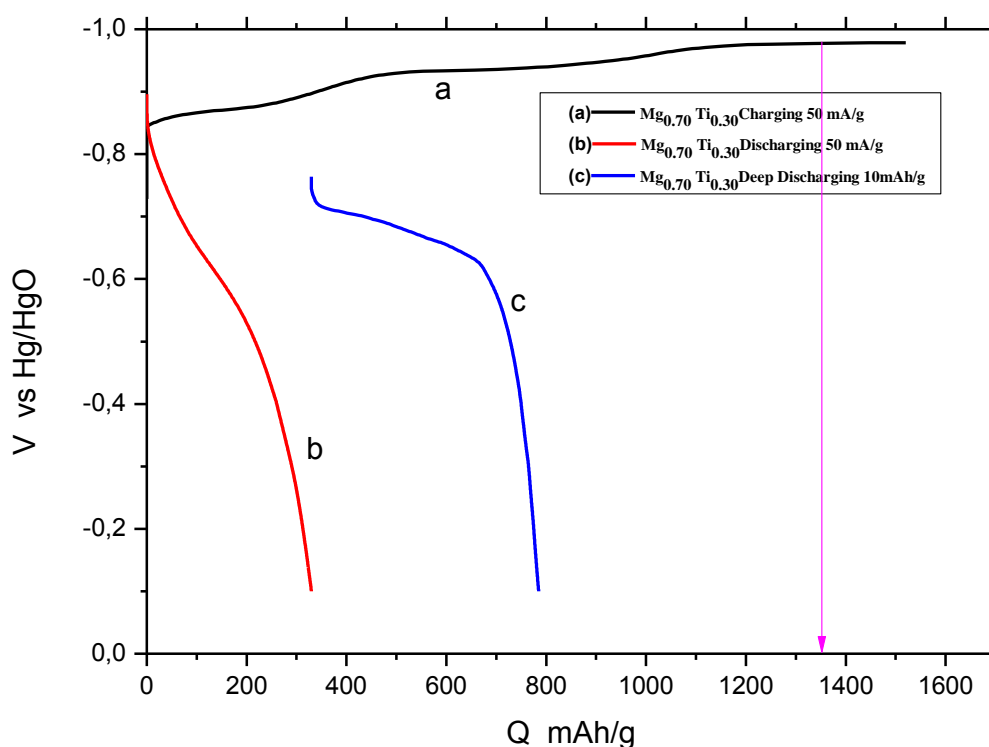


**Figure 6.3:** The electrochemical measurements of the  $Mg_{0.70}Ti_{0.30}$  alloy.

According to Figure 6.3 total capacity of  $Mg_{0.70}Ti_{0.30}$  alloy is 5.027 wt.% (1332.37 mAh/g), charging capacity is 1.25 wt.% (333.27 mAh/g), and deepdischarging capacity is 2.96 wt.% (784.95 mAh/g). The midpoint of second plateau is -0.931 V which represents easy charging of the alloy. The HER potential of the alloy is -0.976V. Deviation from the theoretical capacity is ascribed due to the HER reached before the the maximum theoretical capacity.

Comparison of  $\text{Mg}_{0.70}\text{Ti}_{0.30}$  and  $(\text{Mg}_{0.70}\text{Ti}_{0.30})_{0.90}\text{Ni}_{0.10}$  is given in Figure 6.4. Ni peaks by a minor shifting towards lower angle appears on the XRD pattern after milling  $\text{Mg}_{0.70}\text{Ti}_{0.30}$  with Ni for 2 hours, shown in Figure 6.4 b. On further milling up to 12 hours the Mg peak shifts towards lower angle and Ni reflections disappear completely. The molar volume of Ni is  $6.59\text{ cm}^3/\text{mol}$  which is smaller compared to Mg and Ti. Addition of Ni is theoretically expected to reduce the lattice parameters of Mg-Ti alloy by thus shifting the Mg peak towards higher angle. The shifting of Mg peak towards lower angle conflict with the theoretical explanation given above. If shifting towards lower angle is not due to the particle size differences for the alloys or any other measurement conditions that can affect the XRD pattern, this could be due to an increase in the lattice parameters of Mg-Ti alloy by addition of Ni. Since the Ni reflections disappear in 12 hours milling process on XRD pattern, Ni dissolution in the Mg-Ti alloy could be occurred with an increase in lattice parameters. The crystal structure remains HCP and the lattice parameters of a and c for the material are 3.187, c 5.14 Å, respectively.

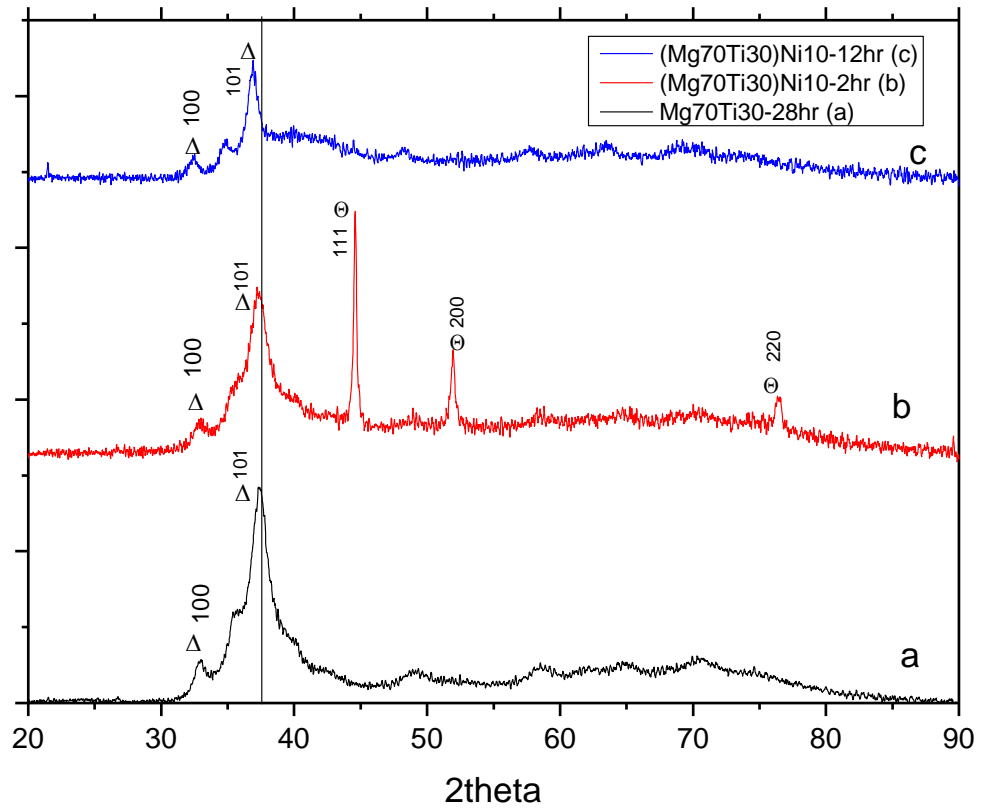


**Figure 6.4:** XRD patterns of  $(\text{Mg}_{70}\text{Ti}_{30})_{0.90}\text{Ni}_{10}$  ( $\Delta$  represent Mg and  $\Theta$  present Ni).

The SEM micrographs of  $(\text{Mg}_{0.70}\text{Ti}_{0.30})_{0.90}\text{Ni}_{0.10}$  are shown in Figure 6.5. The main particle size lies between 10 and 20  $\mu\text{m}$ .

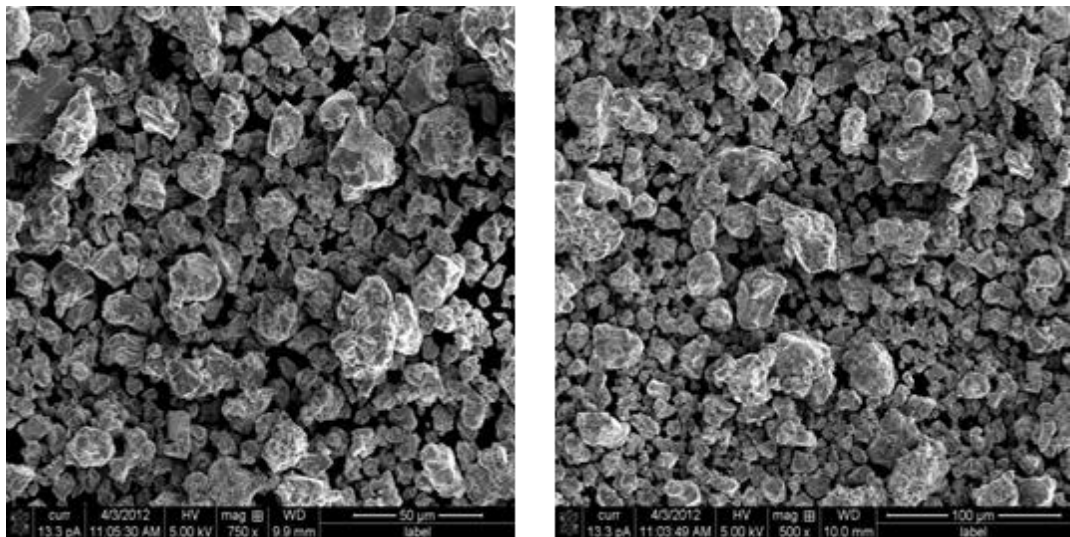


**Figure 6.5:** SEM micrographs of  $(\text{Mg}_{0.70}\text{Ti}_{0.30})_{0.90}\text{Ni}_{0.10}$ .

Figure 6.6 shows that the theoretical capacity of  $(\text{Mg}_{0.70}\text{Ti}_{0.30})_{0.90}\text{Ni}_{0.10}$  is 5.218 wt.% (1382.77 mAh/g). Total capacity of this material is 3.7 wt.% (983.02 mAh/g), discharging capacity is 1.61 wt.% (426.09 mAh/g), and deepdischarging capacity is 3.02 wt.% (800.30 mAh/g). The alloy behaves the similar way as that of pure  $\text{Mg}_{0.70}\text{Ti}_{0.30}$  which shows two plateau regions in the hydrogenation curve. The plateau potentials moved towards higher value indicating the change in the kinetics and thermodynamic property of the alloy. The difference between charging and deepdischarging capacities of this alloy is approximately 200 mAh/g. The value was approximately 550 mAh/g for pure  $\text{Mg}_{0.70}\text{Ti}_{0.30}$ . When these values are compared, it is clearly seen that there is an important improvement for  $(\text{Mg}_{0.70}\text{Ti}_{0.30})_{0.90}\text{Ni}_{0.10}$  alloy compared to the pure  $\text{Mg}_{0.70}\text{Ti}_{0.30}$ .

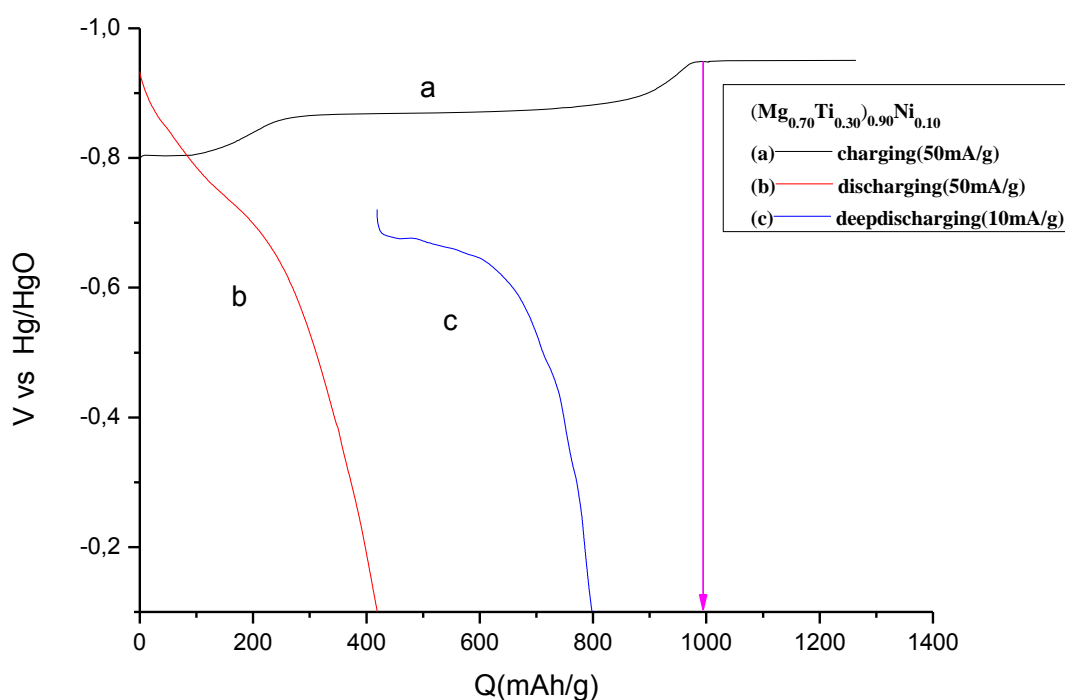


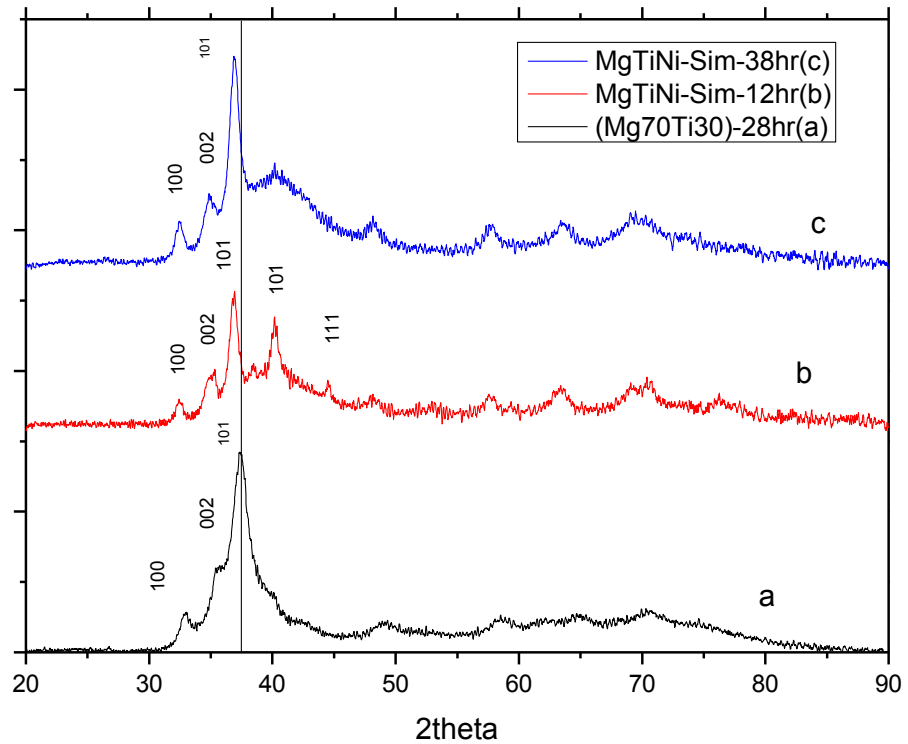
**Figure 6.6:** The electrochemical charging and discharging graph of the  $(\text{Mg}_{70}\text{Ti}_{30})_{0.90}\text{Ni}_{10}$  alloy.

$\text{Mg}_{0.70}\text{Ti}_{0.30}$  is metastable alloy. Nickel which is having negative heat of mixing with both Mg and Ti would stabilize the  $\text{Mg}_{0.70}\text{Ti}_{0.30}$  alloy. According to “reverse rule of stability” the more stable the alloys the less stable the their hydride will be. Because

of this, Ni addition is expected to increase the rate of hydrogenation and dehydrogenation properties and alter the thermodynamics of the Mg-Ti alloy.

Since Nickel by itself has good catalytic activity, Nickel is expected to improve the kinetics of the system. The theoretical capacity of alloy was calculated based on the H/M as 2 for Mg and Ti and H/M as 0.7 for Ni.

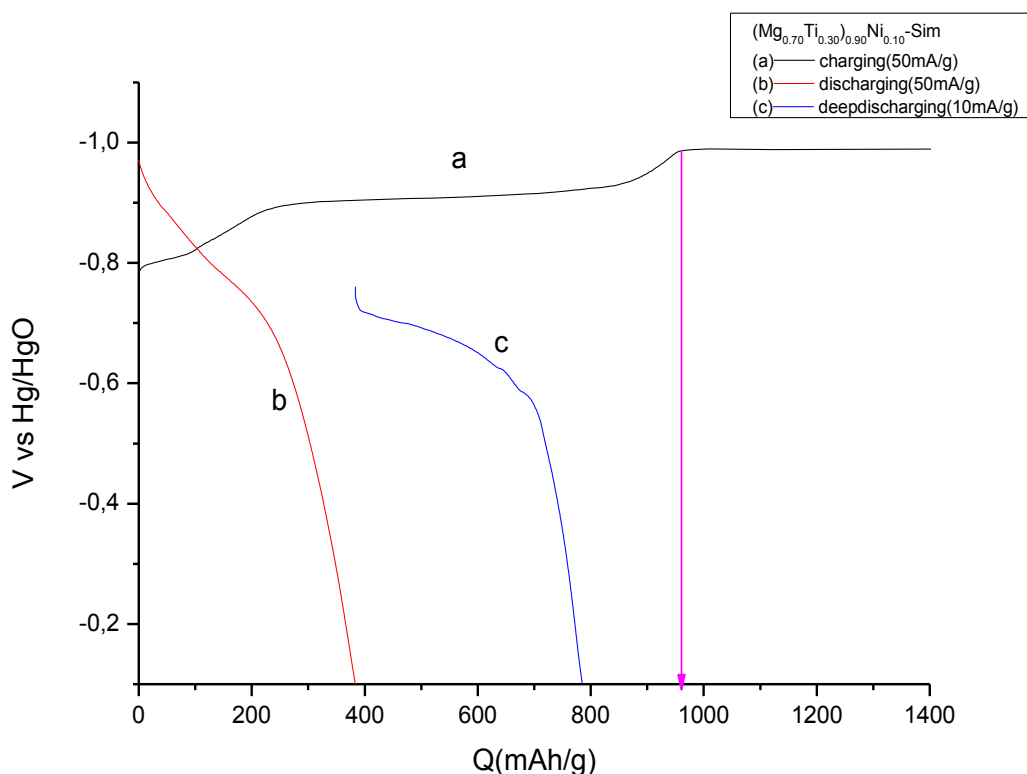
For comparasion of the alloying method with premilled alloy, simultaneous milling was carried out. All Mg, Ti and Ni were added simultaneously and milled. The XRD pattern shows the formation of HCP structure with similar lattice constant values and the alloying was completed within 38 hours (Figure 6.7).



**Figure 6.7:** XRD patterns of  $(\text{Mg}_{0.70}\text{Ti}_{0.30})_{0.90}\text{Ni}_{0.10}$  simultaneously milled alloy compared with the reference alloy  $(\text{Mg}_{70}\text{Ti}_{30})$ . The Mg reflection is shifting to the lower angles, which means lattice parameters are increasing. Lattice parameters of a and c for  $\text{Mg}_{0.70}\text{Ti}_{0.30}$  are 3.141, 5.02 Å, respectively. Lattice parameters of a and c for the materials

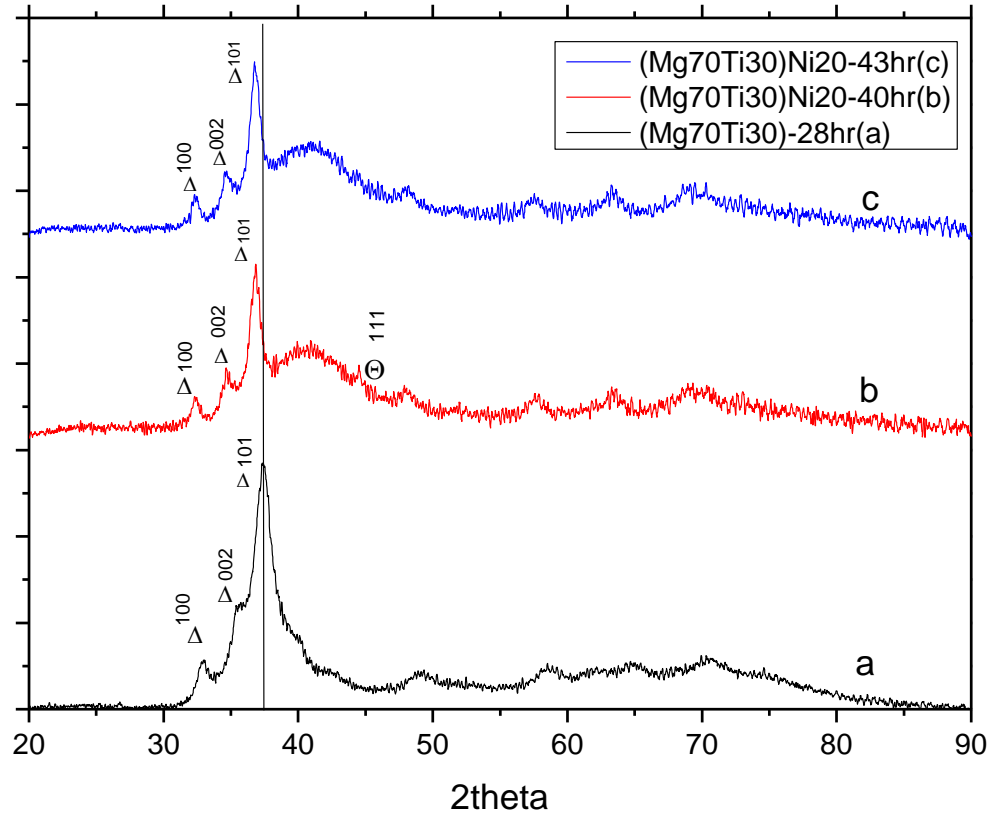
prepared simultaneously are 3.175, 5.12 Å, respectively. Lattice parameters of a and c for  $(\text{Mg}_{0.70}\text{Ti}_{0.30})_{0.90}\text{Ni}_{0.10}$  are 3.187, 5.14 Å, respectively. The lattice constants of simultaneously milled alloy is similar to that of premilled  $(\text{Mg}_{0.70}\text{Ti}_{0.30})_{0.90}\text{Ni}_{0.10}$ .

Total capacity of the simultaneously alloy is 3.63 wt.% (964.01 mAh/g), charging capacity is 1.44 wt.% (383.70 mAh/g), deepdischarging capacity is 2.96 wt.% (786.41 mAh/g). Plateau potential is -0.991 V. Figure 6.8 looks similar to the Figure 6.6 which belongs to  $(\text{Mg}_{0.70}\text{Ti}_{0.30})_{0.90}\text{Ni}_{0.10}$ .



**Figure 6.8:** The electrochemical charging and discharging graph of the  $(\text{Mg}_{0.70}\text{Ti}_{0.30})_{0.90}\text{Ni}_{0.10}$  simultaneously alloy.

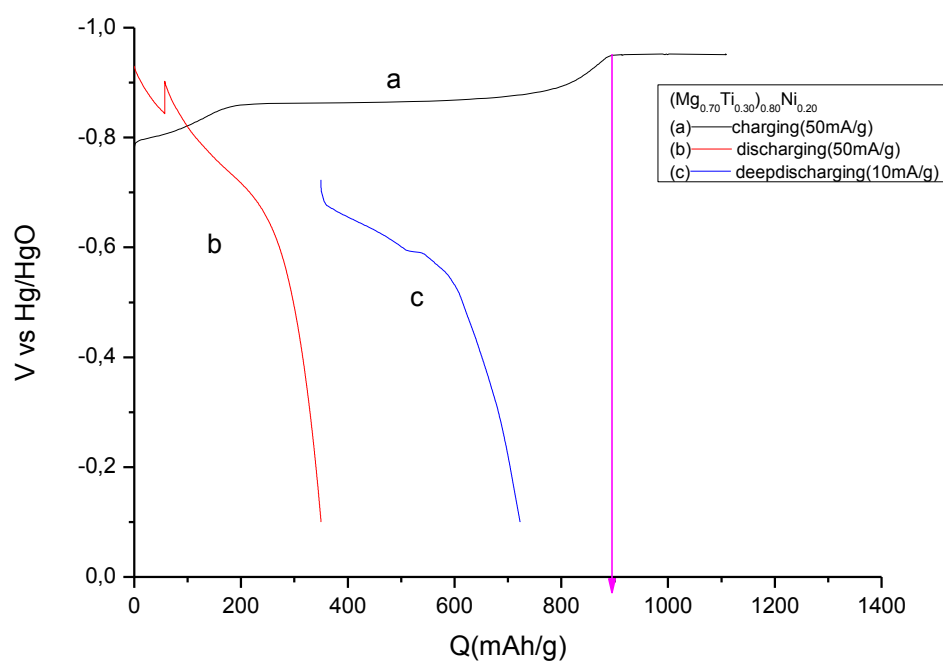
In Figure 6.9, the XRD patterns of  $\text{Mg}_{0.70}\text{Ti}_{0.30}$  and  $(\text{Mg}_{0.70}\text{Ti}_{0.30})_{0.80}\text{Ni}_{0.20}$  are compared. After premilling  $\text{Mg}_{0.70}\text{Ti}_{0.30}$  alloy with 20 at.% Ni for 12 hours, Ni peaks by a minor shift towards to lower angle appears on the XRD pattern (Figure 6.9b). Milling up to 15 hours the Mg peak shifts towards to lower angle and Ni reflections disappeared, which means  $(\text{Mg}_{0.70}\text{Ti}_{0.30})_{0.80}\text{Ni}_{0.20}$  completely alloyed. A broad background is found near the Mg reflection which does not present in Ni 10 at.%.



**Figure 6.9:** XRD pattern of  $(\text{Mg}_{0.70}\text{Ti}_{0.30})_{0.80}\text{Ni}_{0.20}$  ( $\Delta$  represent Mg and  $\Theta$  present Ni).

The lattice parameters of  $(\text{Mg}_{0.70}\text{Ti}_{0.30})_{0.80}\text{Ni}_{0.20}$  tends to increase. The crystal structure of the alloy formed is HCP. Ni is dissolved in Mg-Ti alloy. Lattice parameters of a and c for this material are 3.187, 5.18 Å, respectively. The lattice parameters are higher than that of  $\text{Mg}_{0.70}\text{Ti}_{0.30}$ . The lattice parameters of  $(\text{Mg}_{0.70}\text{Ti}_{0.30})_{0.80}\text{Ni}_{0.20}$  are similar to that of  $(\text{Mg}_{0.70}\text{Ti}_{0.30})_{0.90}\text{Ni}_{0.10}$  with ambiguity in c-axis. The reason of this needs to be explained by making further experiments in details.

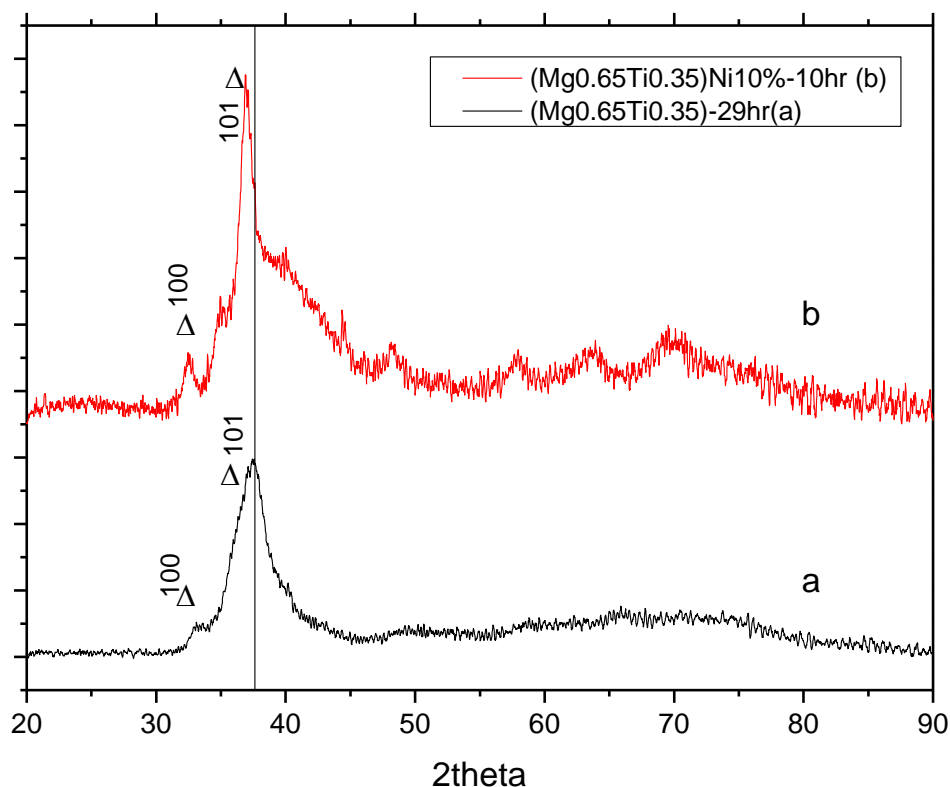
In Figure 6.10, it is shown that the theoretical capacity of  $(\text{Mg}_{0.70}\text{Ti}_{0.30})_{0.80}\text{Ni}_{0.20}$  is 4.51 wt.% (1195 mAh/g). Experimental total capacity of this material was measured as 3.39 wt.% (900 mAh/g) with a charging and deepdischarging capacities of 1.32wt.% (350mAh/g), 2.73wt.% (725mAh/g), respectively.



**Figure 6.10:** The electrochemical charging and discharging graph of the  $(\text{Mg}_{70}\text{Ti}_{30})_{0.80}\text{Ni}_{20}$  alloy.

Figure 6.11 shows XRD patterns of  $\text{Mg}_{0.65}\text{Ti}_{0.35}$  and  $(\text{Mg}_{0.65}\text{Ti}_{0.35})_{0.90}\text{Ni}_{0.10}$ .  $\text{Mg}_{0.65}\text{Ti}_{0.35}$  alloy is first prepared by milling of 29 hours. After milling of  $\text{Mg}_{0.65}\text{Ti}_{0.35}$  with 10 wt.% for further 10 hours, Ni peaks disappear on XRD pattern (Figure 6.11b), which means  $(\text{Mg}_{0.65}\text{Ti}_{0.35})_{0.90}\text{Ni}_{0.10}$  alloy is occurred.

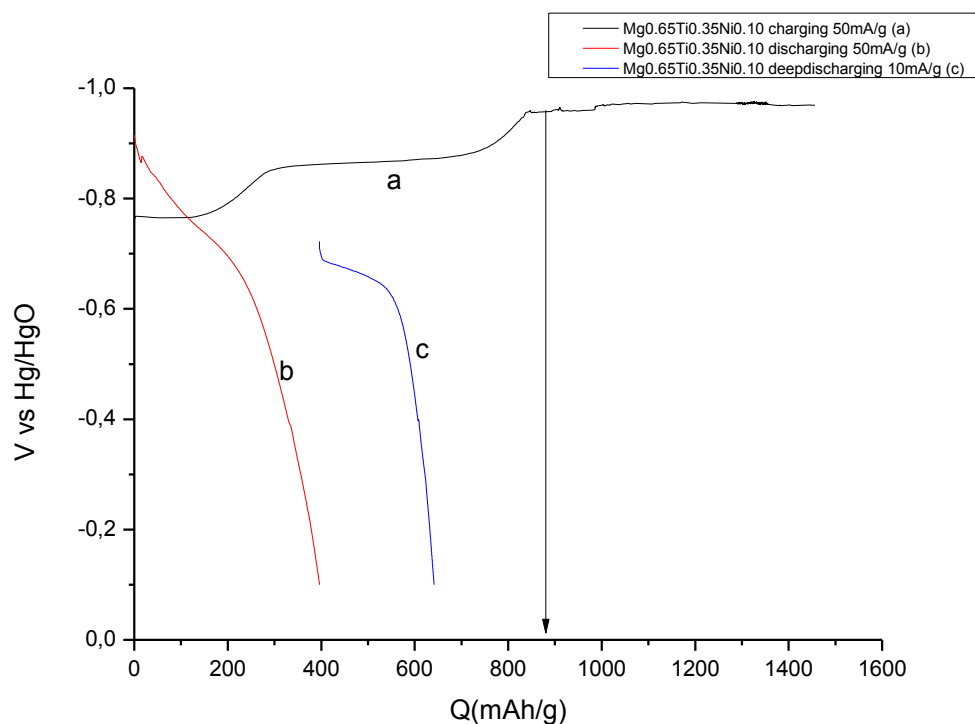




**Figure 6.11:** XRD patterns of  $(\text{Mg}_{0.65}\text{Ti}_{0.35})_{0.90}\text{Ni}_{0.10}$  ( $\Delta$  represent Mg).

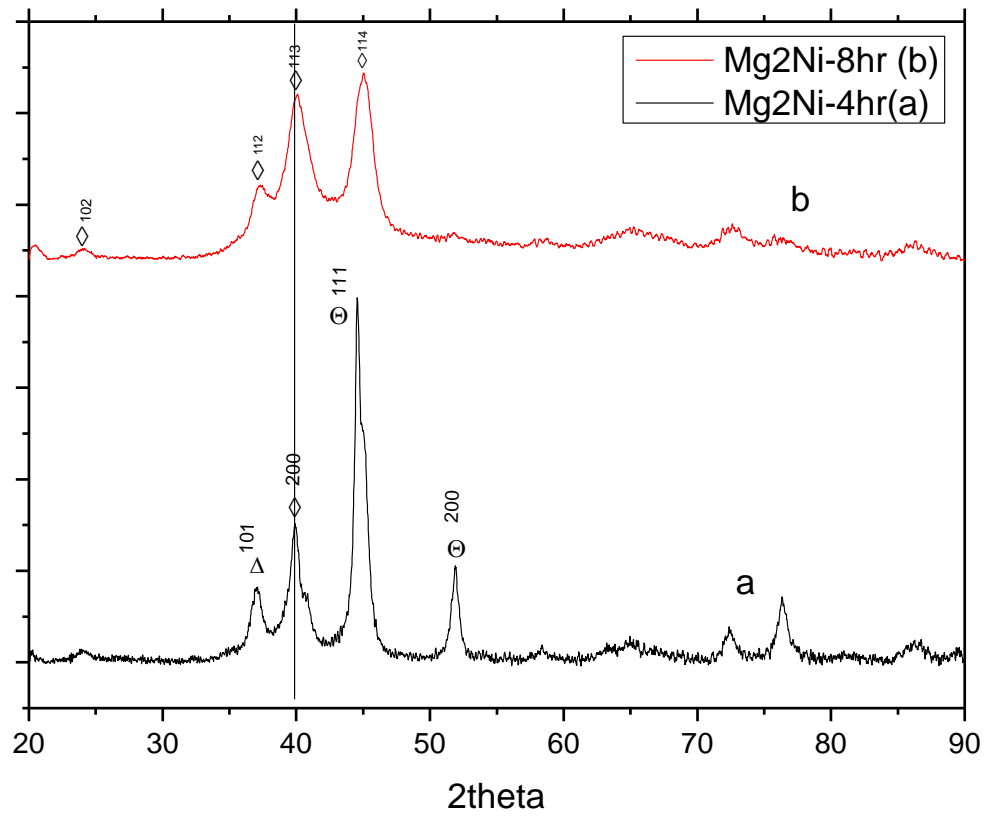
Mg peak shiftings towards to lower angles, and lattice parameters of the material are increased compared to  $\text{Mg}_{0.65}\text{Ti}_{0.35}$ . HCP phase is formed for the  $(\text{Mg}_{0.65}\text{Ti}_{0.35})_{0.90}\text{Ni}_{0.10}$  alloy. Lattice parameters of  $a$  and  $c$  for  $\text{Mg}_{0.65}\text{Ti}_{0.35}$  are 3.118, 4.84 Å, respectively. Lattice parameters of  $a$  and  $c$  of  $(\text{Mg}_{0.65}\text{Ti}_{0.35})_{0.90}\text{Ni}_{0.10}$  are 3.175, 5.12 Å, respectively.

Electrochemical graph of  $(\text{Mg}_{0.65}\text{Ti}_{0.35})_{0.90}\text{Ni}_{0.10}$  is given in Figure 6.12. The theoretical capacity of  $(\text{Mg}_{0.65}\text{Ti}_{0.35})_{0.90}\text{Ni}_{0.10}$  is 5.069 wt.% (1343 mAh/g). Total capacity of this material is 3.33 wt.% (882 mAh/g) with a discharging and deepdischarging capacities are 1.49 wt.% (395 mAh/g), 2.41 wt.% (638 mAh/g), respectively. Plateau potential is -0.960 V.



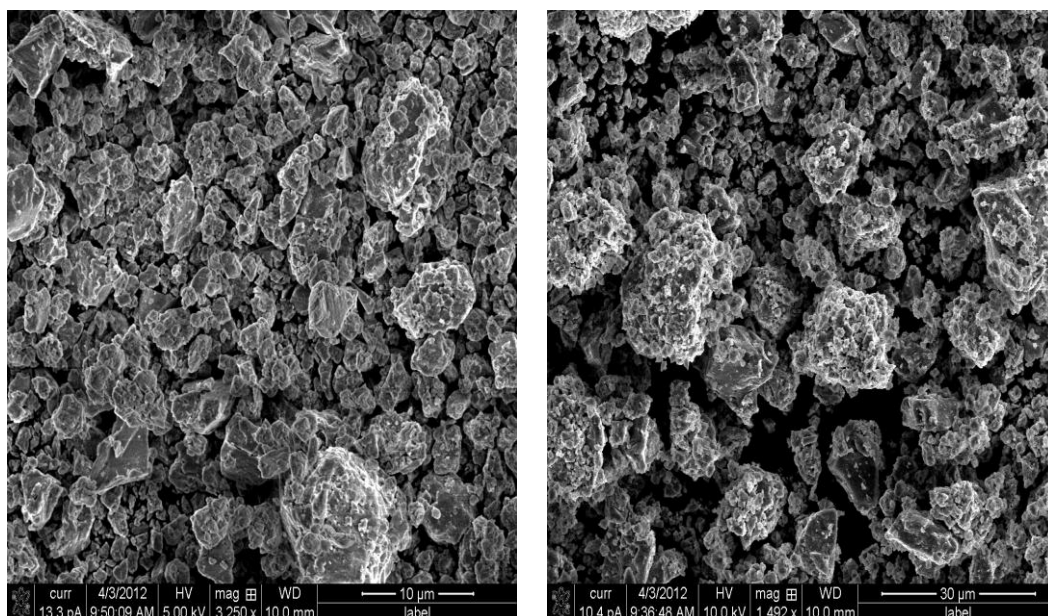
**Figure 6.12.** The electrochemical charging and discharging graph of the  $(\text{Mg}_{0.65}\text{Ti}_{0.35})_{0.90}\text{Ni}_{0.10}$  alloy.

An attempt was made to synthesized the  $\text{Mg}_2\text{Ni}$  first and then add Titanium in the later stages of the milling and observe the influence of the  $\text{Mg}_2\text{Ni}$  premilling on the final ternary alloys. The XRD patterns of  $\text{Mg}_2\text{Ni}$  for different milling hours, are given in Figure 6.13.



**Figure 6.13:** XRD patterns of Mg<sub>2</sub>Ni(Δ represent Mg, Θ present Ni and ◇ Mg<sub>2</sub>Ni).

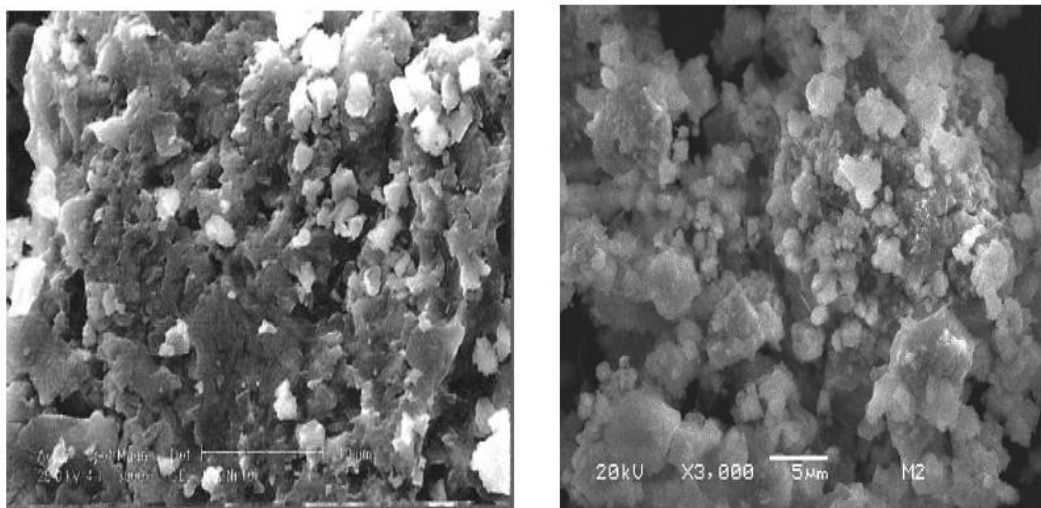
Mg<sub>2</sub>Ni peak started to emerge at 4 hours milling time with an existing of Ni peaks. With an increase in milling time upto 8 hours the Ni reflections are disappeared and the Mg<sub>2</sub>Ni reflections become visible only. This indicates the complete formation of the Mg<sub>2</sub>Ni compound. The SEM micrograph of Mg<sub>2</sub>Ni (Figure 6.14) shows that the main particle size of Mg<sub>2</sub>Ni is smaller compared to Mg-Ti alloy. The mean particle size is about 1-10μm. EDX analysis indicates the presence of Mg 66 at.% and Ni 33at.%.



**Figure 6.14:** SEM micrographs of Mg<sub>2</sub>Ni

Garcia et al. [142] studied the production of Mg<sub>2</sub>Ni in the presence of methanol as a controlling agent in milling process. The SEM micrograph of Mg<sub>2</sub>Ni produced by Garcia et al. is shown in Figure 6.15. In Figure 6.15b, a plastic deformation were observed in form of flakes and individual particles that thus Magnesium and Nickel elements that had not yet reacted by the forces of interactions during the milling process. It is noticable on the image that after 4 hours of milling process the union events and fragmentation were initiated indicating laminar morphology. They supported this phenomenon by XRD analysis in their studies.

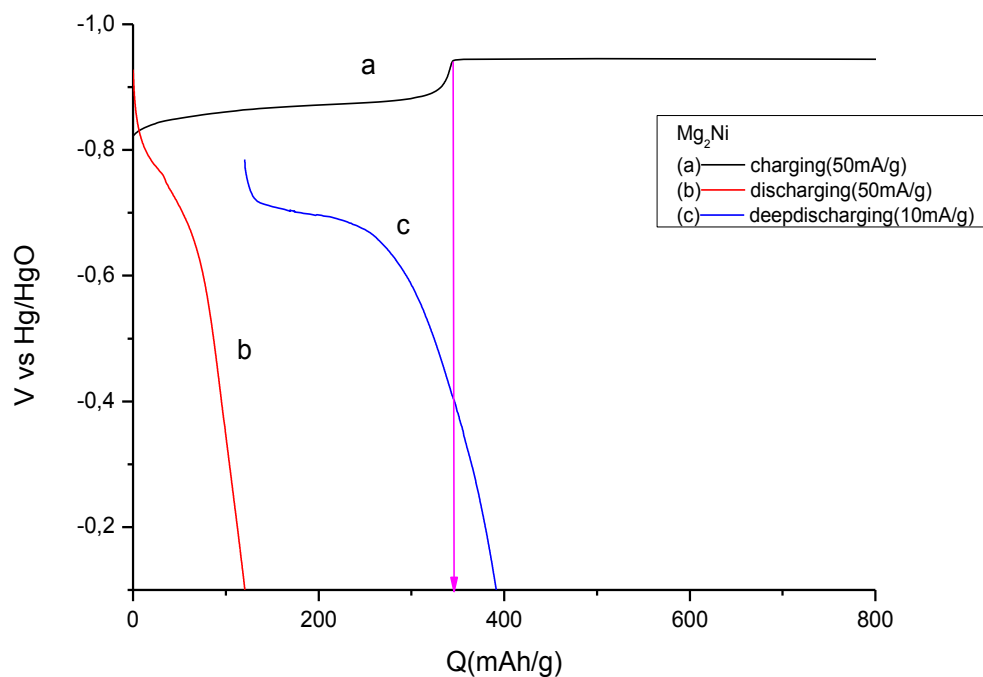
Since any segregation of the elements was not observed locally, they were concluded that the initial elements had completely reacted to form the Mg<sub>2</sub>Ni compound.



**Figure 6.15:** The SEM micrograph of  $\text{Mg}_2\text{Ni}$  after 4 (b) and 10 (a) hours of milling[142].

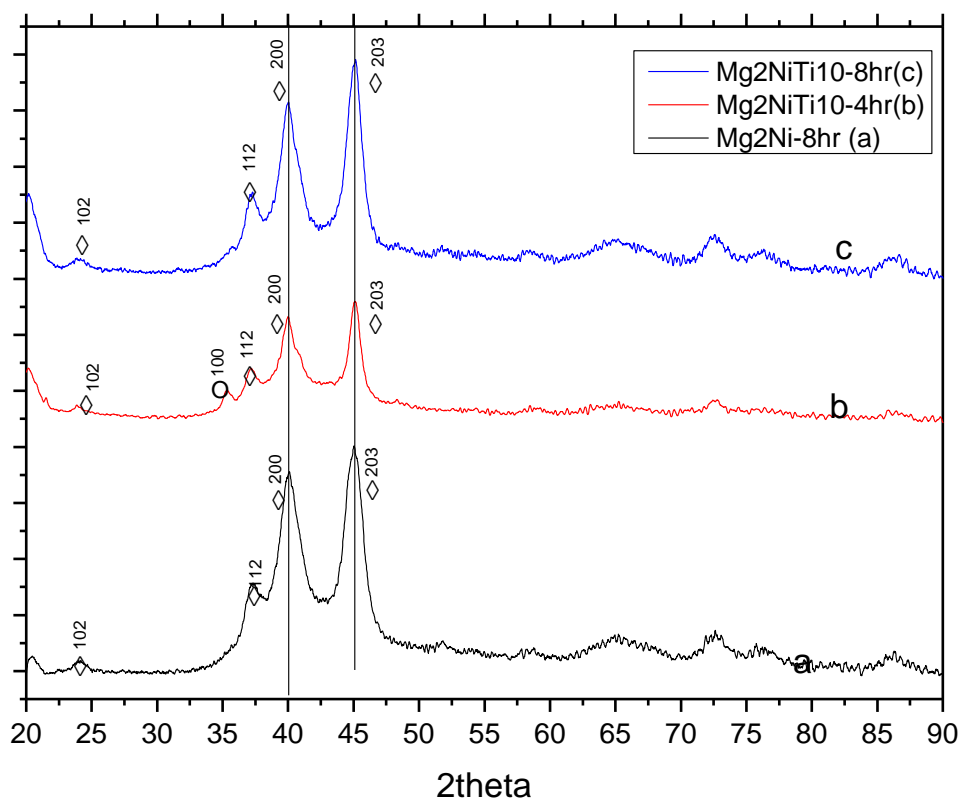
The experimental results about  $\text{Mg}_2\text{Ni}$  obtained in this study were compared and observed that the results were parallel to the results given in literature. Comparing the experimental results in this study with the literature work with the other publication's SEM micrographs and XRD patterns, the results are parallel.

Figure 6.16 shows that the total capacity of  $\text{Mg}_2\text{Ni}$  is 1.34 wt.% (355.54 mAh/g) and the discharging and deepdischarging capacities of  $\text{Mg}_2\text{Ni}$  are 0.46 wt.% (122.52 mAh/g), 2.26 wt.% (599.74 mAh/g), respectively. Plateau potential is -0.94 V.

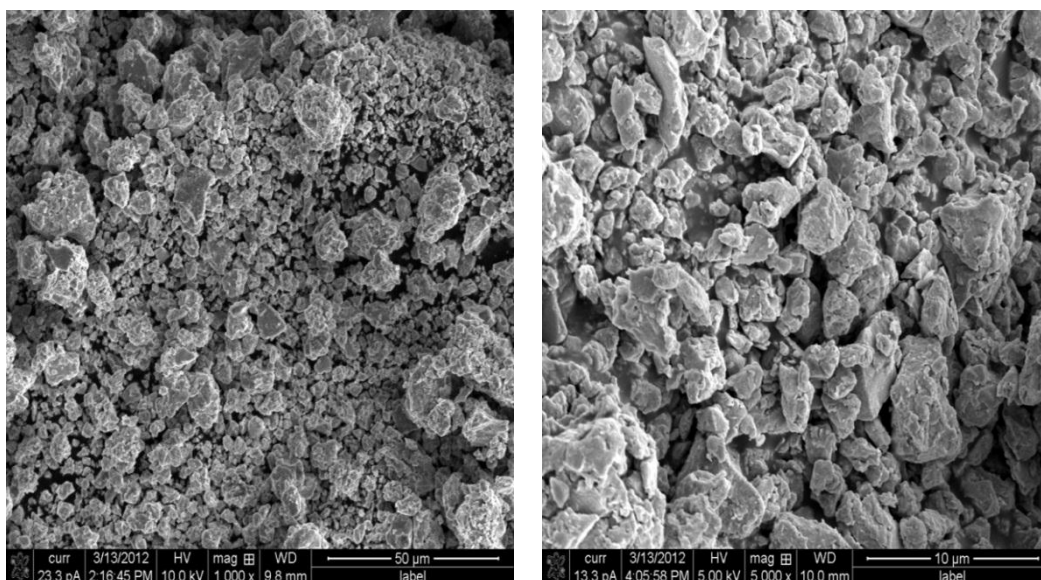


**Figure 6.16.** The electrochemical charging and discharging graph of the  $\text{Mg}_2\text{Ni}$  alloy.

Figure 6.17 shows XRD patterns of  $\text{Mg}_2\text{Ni}$  and  $(\text{Mg}_2\text{Ni})_{0.90}\text{Ti}_{0.10}$ . As it can be seen from Figure 6.17b Ti peaks exist after 4 hours milling of  $\text{Mg}_2\text{Ni}$  with Ti. Upon further milling Ti peaks disappeared and only  $\text{Mg}_2\text{Ni}$  peaks are visible. Any peak shifts in the main peaks were not observed depending on the milling time, despite Mg-Ti-Ni and Mg-Ti-Si alloys. SEM micrographs (Figure 6.18) show the some cold welded agglomerates with the particle size of  $\text{Mg}_2\text{Ni}$  ranging from 1 to 10  $\mu\text{m}$ .

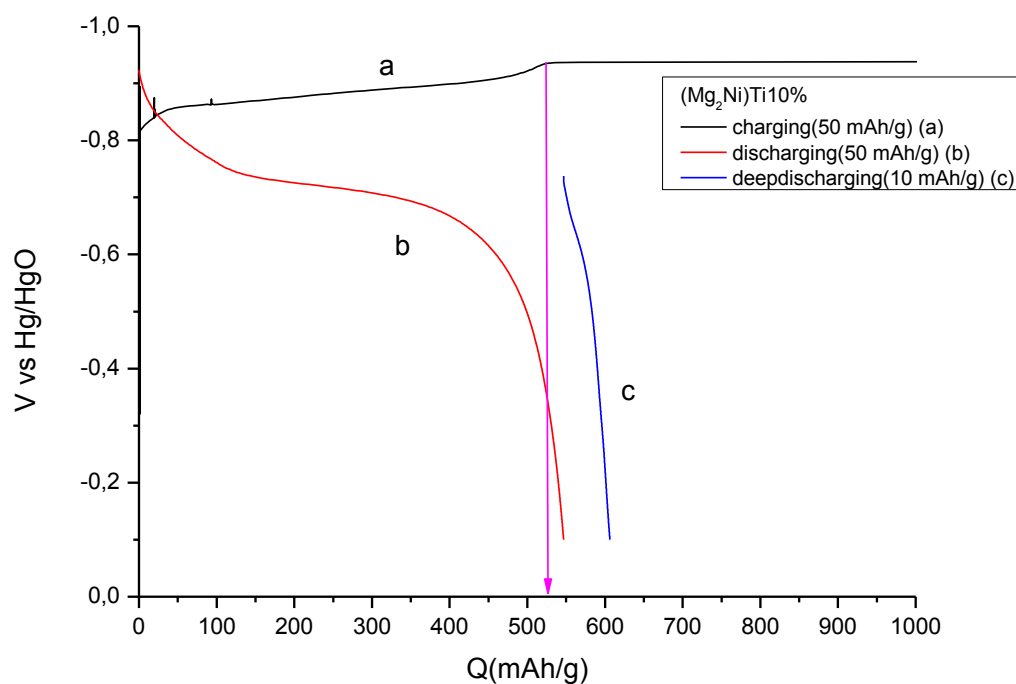


**Figure 6.17.** XRD patterns of  $\text{Mg}_2\text{Ni}$  and  $(\text{Mg}_2\text{Ni})_{0.90}\text{Ti}_{0.10}$



**Figure 6.18.** SEM micrograph of  $(\text{Mg}_2\text{Ni})_{0.90}\text{Ti}_{0.10}$

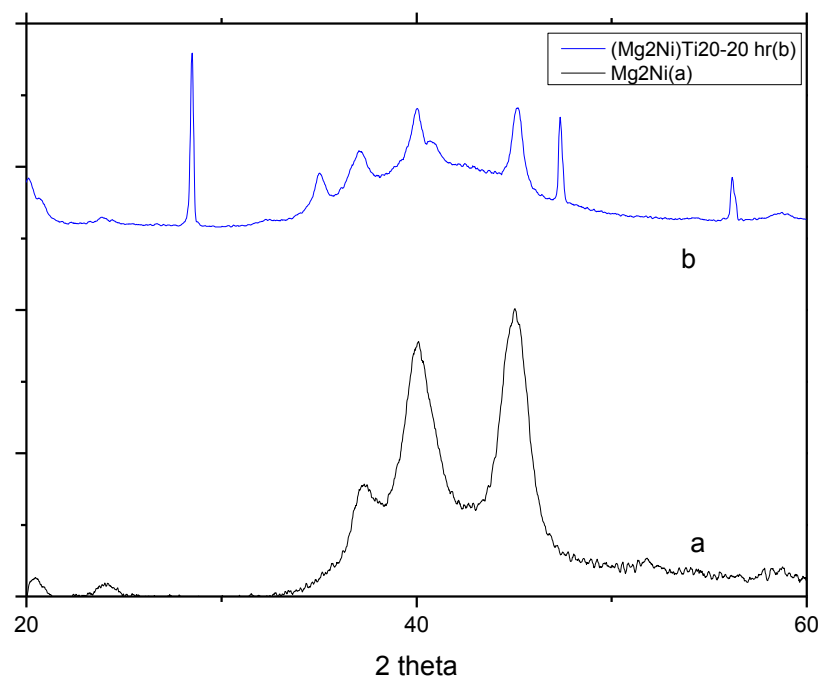
In Figure 6.19, the total capacity of  $(\text{Mg}_2\text{Ni})_{0.90}\text{Ti}_{0.10}$  can be observed as 2.07 wt.% (550.30 mAh/g), charging capacity and deepdischarging capacities are 1.48 wt.% (392.94 mAh/g), 2.28 wt.% (605.76 mAh/g), respectively. Plateau potential is -0.93V.



**Figure 6.19.** The electrochemical charging and discharging graph of the  $(\text{Mg}_2\text{Ni})_{0.90}\text{Ti}_{0.10}$  alloy.

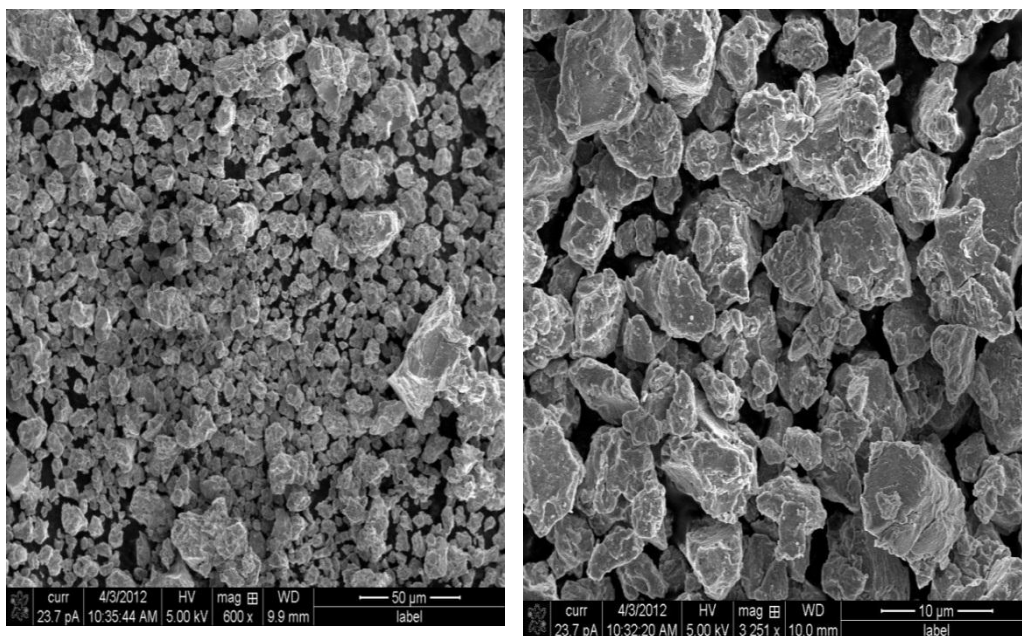
The XRD patterns of  $(\text{Mg}_2\text{Ni})_{0.80}\text{Ti}_{0.20}$  was measured in different department and using different equipment, shown in Figure 6.20. Figure 6.20, the shift of  $\text{Mg}_2\text{Ni}$  reflections were not observed again.





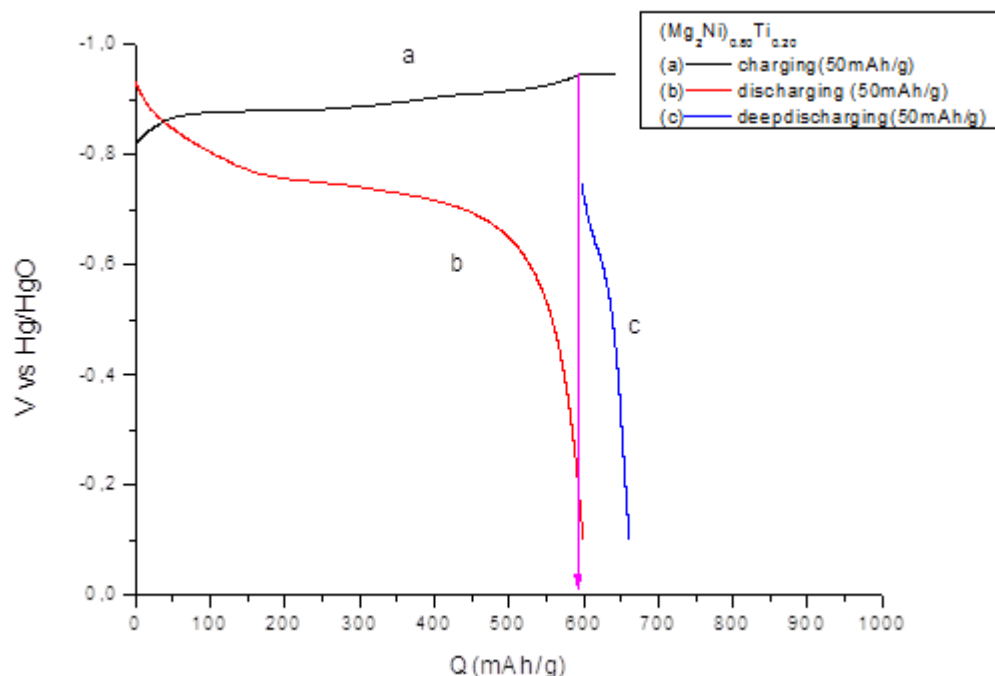
**Figure 6.20.** XRD patterns of  $(\text{Mg}_2\text{Ni})_{0.80}\text{Ti}_{0.20}$

The SEM micrographs of  $(\text{Mg}_2\text{Ni})_{0.80}\text{Ti}_{0.20}$  shown in Figure 6.21 represent similar particle distribution with the  $(\text{Mg}_2\text{Ni})_{0.90}\text{Ti}_{0.10}$ , with the particles size ranging from 1 to 10  $\mu\text{m}$ .



**Figure 6.21.** SEM micrographs of  $(\text{Mg}_2\text{Ni})_{0.80}\text{Ti}_{0.20}$

In Figure 6.22 the total capacity of  $(\text{Mg}_2\text{Ni})_{0.80}\text{Ti}_{0.20}$  is 2.31 wt.% (613.92 mAh/g), charging and deepdischarging capacities are 2.06 wt.% (547.72 mAh/g), 2.49 wt.% (660.79 mAh/g), respectively. Plateau potential is -0.94 V.



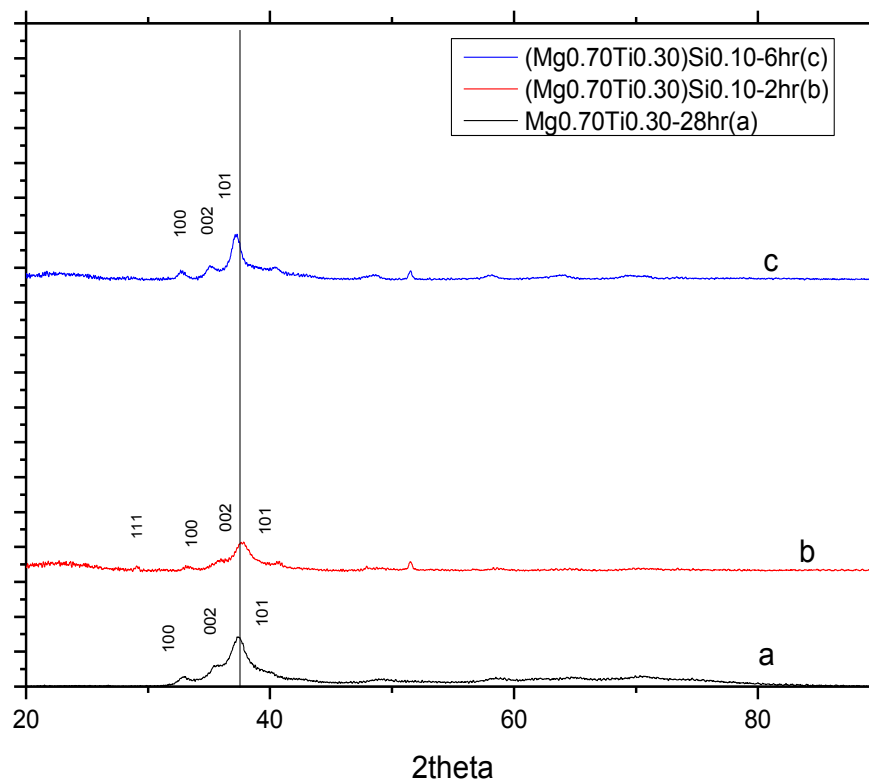
**Figure 6.22:** The electrochemical charging and discharging graph of the  $(\text{Mg}_2\text{Ni})_{0.80}\text{Ti}_{0.20}$  alloy.

Figure 6.23 shows the XRD patterns of  $\text{Mg}_{0.70}\text{Ti}_{0.30}$  and  $(\text{Mg}_{0.70}\text{Ti}_{0.30})_{0.90}\text{Si}_{0.10}$ .  $\text{Mg}_{0.70}\text{Ti}_{0.30}$  was milled with Si for 2 hours. In the XRD pattern of this alloy shown in Figure 6.23b, Si reflection is still visible. On further milling with Si upto 4 hours, Si reflection disappeared which means Si is dissolved in the  $\text{Mg}_{0.70}\text{Ti}_{0.30}$  alloy. When a literature survey on the production of Mg-Ti-Si ternary alloy by using mechanical alloying technique. It can be seen that there is not too much study on this issue. One of the study is published by Brett [143]. The XRD results of them are shown in

Figure 6.24. When the patterns are examined it can be seen that the ternary alloy was not occurred properly. In our case, Mg-Ti-Si ternary alloy was produced properly with the premilling mechanical alloying method (Figure 6.23c).

In Figure 6.23 Mg peak shifted to lower angles, tending to increase in lattice parameters. The crystal structure of the alloy is HCP. Lattice parameters of a and c of

$\text{Mg}_{0.70}\text{Ti}_{0.30}$  are 3.141, 5.02 Å, respectively. Lattice parameters of  $a$  and  $c$  of  $(\text{Mg}_{0.70}\text{Ti}_{0.30})_{0.90}\text{Si}_{0.10}$  are 3.152, 5.1 Å, respectively.



**Figure 6.23:** XRD patterns of  $\text{Mg}_{0.70}\text{Ti}_{0.30}$  and  $(\text{Mg}_{0.70}\text{Ti}_{0.30})_{0.90}\text{Si}_{0.10}$  ( $\Delta$  represent Mg,  $\sigma$  present Si).

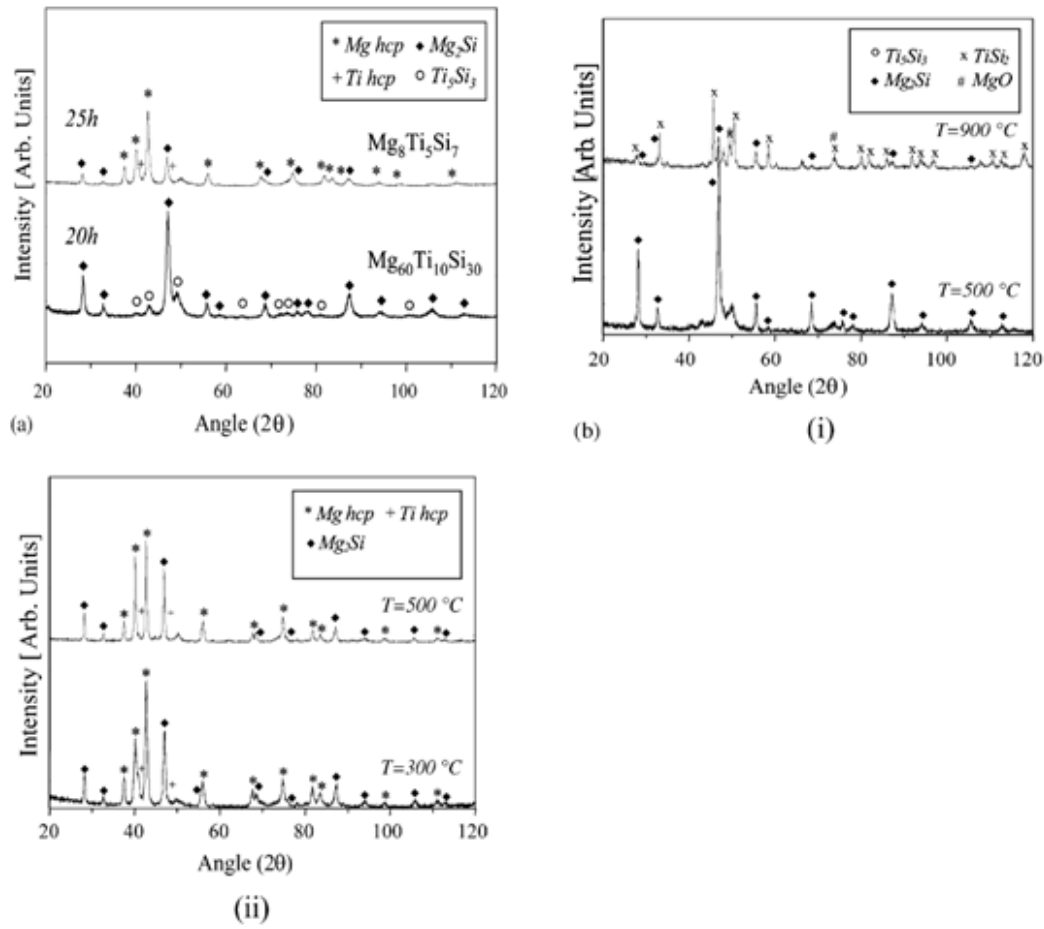


**Figure 6.24:** XRD patterns of samples of: (a) mechanically alloyed  $\text{Mg}_{0.60}\text{Ti}_{0.10}\text{Si}_{0.30}$  and  $\text{Mg}_{0.88}\text{Ti}_{0.05}\text{Si}_{0.07}$ ; (b) heat-treated (i)  $\text{Mg}_{0.60}\text{Ti}_{0.10}\text{Si}_{0.30}$  and (ii)  $\text{Mg}_{0.88}\text{Ti}_{0.05}\text{Si}_{0.07}$ .

SEM micrographs shown Figure 6.25 represent the particle size ranging from 10 to 50  $\mu\text{m}$ , which is similar to Mg-Ti alloy and different from the Ni based alloys containing smaller particles ranged from 1 to 10  $\mu\text{m}$ . One of the reason for the better kinetic performance of the Ni based alloys could be due to the smaller particle size which in turn have different surface area.

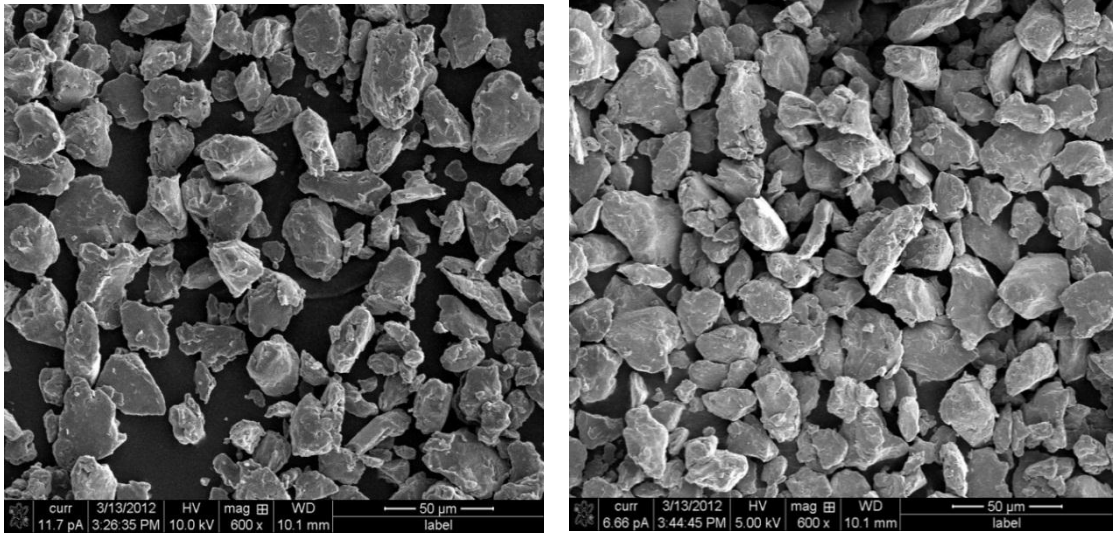


**Figure 6.25:** SEM micrographs of  $(\text{Mg}_{0.70}\text{Ti}_{0.30})_{0.90}\text{Si}_{0.10}$

In Figure 6.26, the theoretical capacity of  $(\text{Mg}_{0.70}\text{Ti}_{0.30})_{0.90}\text{Si}_{0.10}$  is 5.70 wt.% (1510.5 mAh/g). Total capacity of this material is 2.78 wt.% (737.44 mAh/g), charging and deepdischarging capacities are 0.44 wt.% (116.20 mAh/g), 1.85 wt.% (490.41 mAh/g), respectively. Plateau potential is -0.96 V.

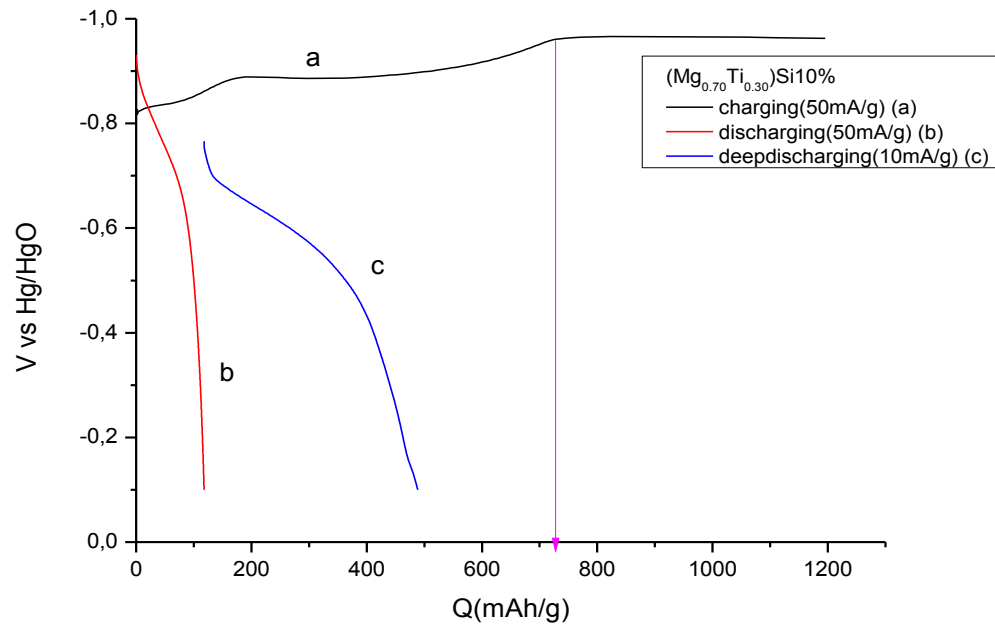
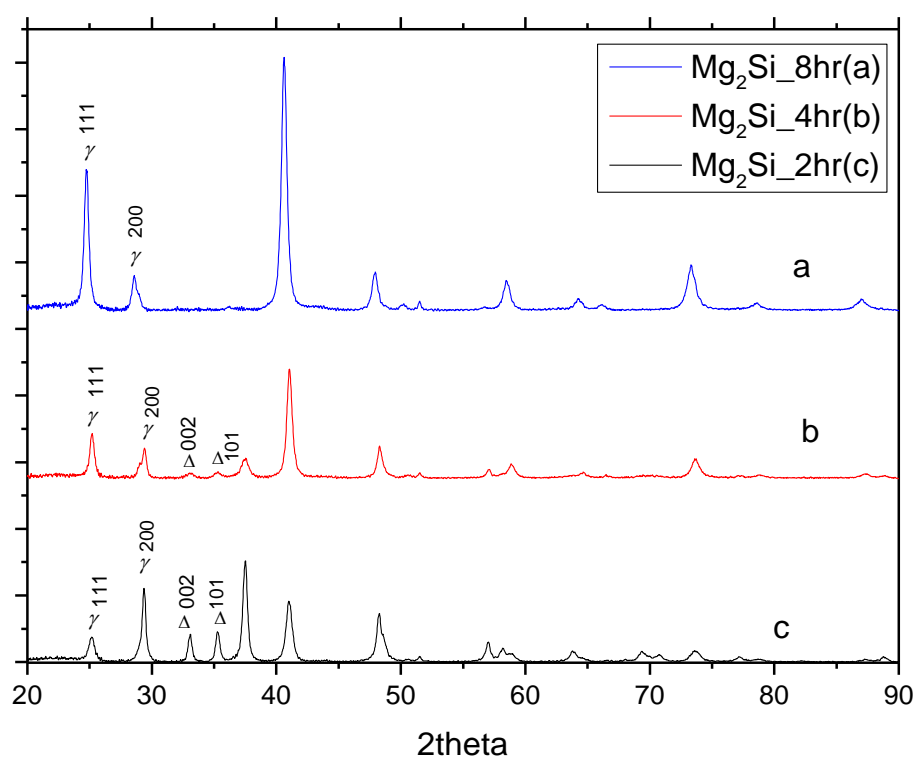


**Figure 6.26:** The electrochemical charging and discharging graph of the  $(\text{Mg}_{0.70}\text{Ti}_{0.30})_{0.90}\text{Si}_{0.10}$  alloy.

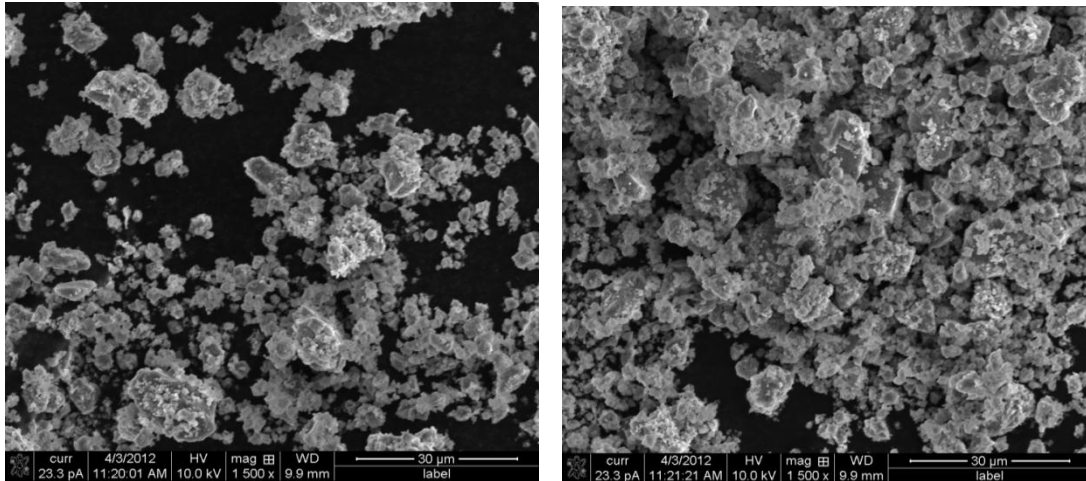
Figure 6.27 shows the XRD patterns of  $\text{Mg}_2\text{Si}$ . Mg reflections exist upto 8 hours milling process. After 8 hours milling time Mg peaks disappear, showing  $\text{Mg}_2\text{Si}$  alloy occurred completely. The particle size of  $\text{Mg}_2\text{Si}$  ranges from 1 to  $30\mu\text{m}$  (

Figure 6.28).

Munoz-Palos et al. [144] was demonstairted the SEM image of  $\text{Mg}_2\text{Si}$  having spherical shapes (Figure 6.29). They commended that at a higher magnification, the particles were resolved as agglomerates arising, (in their case that is probably) from the cold welding of the mixtures with the jar wall (small bright particles).



**Figure 6.27:** XRD patterns of  $\text{Mg}_2\text{Si}$  alloy.



**Figure 6.28:** SEM micrographs for  $\text{Mg}_2\text{Si}$ .

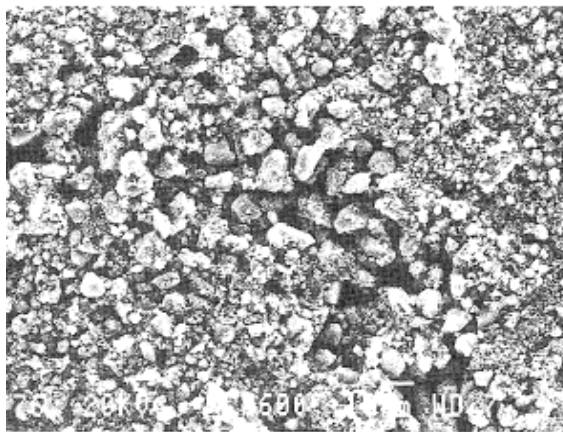


**Figure 6.29:** SEM micrograph of a general view of mechanically alloyed  $\text{Mg}_2\text{Si}$  powder (23 hr alloyed) [144].

As it can be seen from Figure 6.30  $\text{Mg}_2\text{Si}$  reaches immediately starting point of HER, which represent the charging capacity of materials.  $\text{Mg}_2\text{Si}$  is not an efficient hydrogen storage material. Since the charging capacity of  $\text{Mg}_2\text{Si}$  alloy is quite low, any further study on  $\text{Mg}_2\text{Si}$  alloys are not performed.

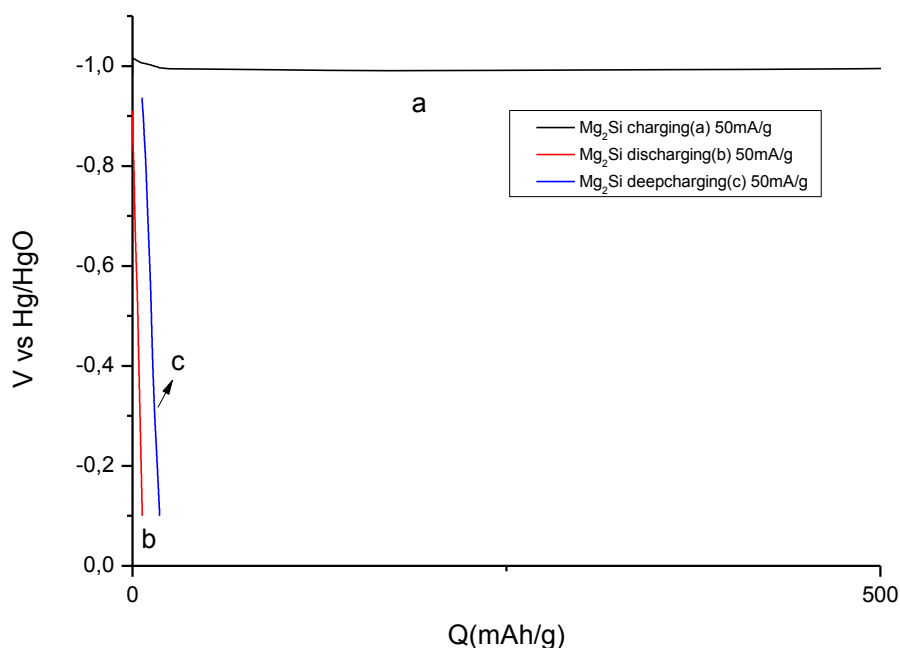


**Figure 6.30.** The electrochemical charging and discharging graph of the  $\text{Mg}_2\text{Si}$  alloy.

## 6.2 Comparisons of the Alloys with Their Hydrogen Storage Performance

In **Figure 6.31**,  $\text{Mg}_{0.70}\text{Ti}_{0.30}$  is compared with  $(\text{Mg}_{0.70}\text{Ti}_{0.30})_{0.90}\text{Ni}_{0.10}$ . As shown in the figure, there is a difference between the charging potentials of  $\text{Mg}_{0.70}\text{Ti}_{0.30}$  and  $(\text{Mg}_{0.70}\text{Ti}_{0.30})_{0.90}\text{Ni}_{0.10}$  having the values of -0.8398 V and -0.7977 V, respectively. The charging potential improved with Ni addition. This means the potential required for hydrogenation of the material becomes lower compared to the binary  $\text{Mg}_{0.70}\text{Ti}_{0.30}$  alloy. Deepdischarging potential was also improved with Ni addition.

Addition 10 at.% Ni to  $\text{Mg}_{0.70}\text{Ti}_{0.30}$  decrease the total capacity from 5.02 wt.% to 3.71 wt.%. Since Ni is heavy element and calculation of  $\text{H}_2$  capacity is defined as per mass amount, the results obtained here was expected. The kinetic improvement did not affect capacity that much. Although kinetic improvement was observed in case of  $(\text{Mg}_{0.70}\text{Ti}_{0.30})_{0.90}\text{Ni}_{0.10}$  compared to  $\text{Mg}_{0.70}\text{Ti}_{0.30}$ , the measured total capacity of  $(\text{Mg}_{0.70}\text{Ti}_{0.30})_{0.90}\text{Ni}_{0.10}$  much lower than expected decrease from the theoretical value and that of  $\text{Mg}_{0.70}\text{Ti}_{0.30}$ . This represent that there is not any positive correlation between the kinetic improvement and total capacity measured. Addition 10 at.% Ni to  $\text{Mg}_{0.70}\text{Ti}_{0.30}$  the discharging capacity increased from 2.96 wt.% to 3.02 wt.%.



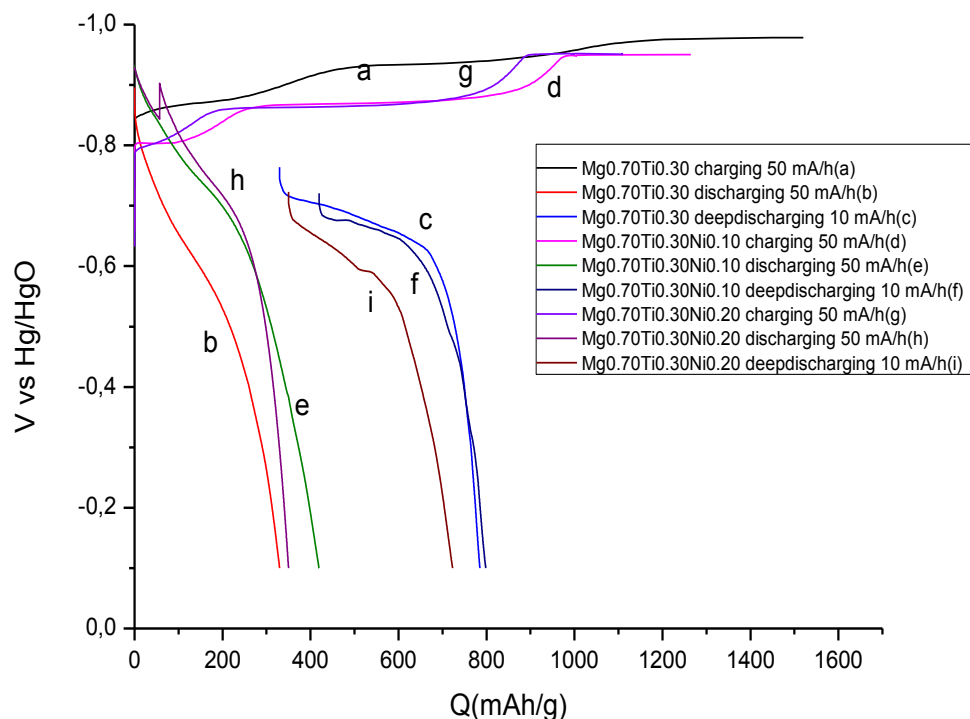


**Figure 6.31:** The electrochemical charging and discharging graphs of the  $\text{Mg}_{0.70}\text{Ti}_{0.30}$ ,  $(\text{Mg}_{0.70}\text{Ti}_{0.30})_{0.90}\text{Ni}_{0.10}$  and  $(\text{Mg}_{0.70}\text{Ti}_{0.30})_{0.80}\text{Ni}_{0.20}$  alloy.

Since Nickel is having negative heat of mixing with both Magnesium and Titanium and  $\text{Mg}_{0.70}\text{Ti}_{0.30}$  is metastable alloy, the alloy could be stabilized with Ni addition. For a stabilized alloy, hydride form of the alloy will be more destabilized. The discharging capacity improved with 10 at.% Ni, when a high rate discharge is applied. It is clear that a given Ni addition (in this study 10 at.%) improves the kinetic performans of  $\text{Mg}_{0.70}\text{Ti}_{0.30}$ . The deepdischarge capacity of  $(\text{Mg}_{0.70}\text{Ti}_{0.30})_{0.90}\text{Ni}_{0.10}$  is almost the same with  $\text{Mg}_{0.70}\text{Ti}_{0.30}$ , showing the former slightly lower value and  $(\text{Mg}_{0.70}\text{Ti}_{0.30})_{0.80}\text{Ni}_{0.20}$ . has much more lower deepdischarge capacity. The possible reason of this could be due to the high rate discharge (50 mA/h) applied ,where the most of the dehydrogenation takes place, before the deepdischarge (10 mA/h). A decrease in the gap between discharge and deepdischarge patterns indicates kinetic improvement of the alloy which makes,the dehydrogenation easily.

As shown in **Figure 6.31**, there is a difference between the charging potentials of  $\text{Mg}_{0.70}\text{Ti}_{0.30}$ ,  $(\text{Mg}_{0.70}\text{Ti}_{0.30})\text{Ni}_{0.10}$  and  $(\text{Mg}_{0.70}\text{Ti}_{0.30})_{0.80}\text{Ni}_{0.20}$  having the values are - 0.8398 V, -0.7977 V, and -0.7884 V, respectively. As it can be seen from the values

the charging potential improved as Ni addition was increased. Addition of Ni improved the deepdischarge potential of the alloy compared to binary one, but the deepdischarge potential was not affected by the amount of Ni addition.

Total capacity of alloy decreased from 3.71 to 3.39 wt.% with 20 at.% Ni addition. As explained before the reason of this is mainly due to addition of Ni which is heavy element.

Kinetic properties of ternary alloy are not changed for 20 at.% Ni addition compared to 10 at.% addition.

In Figure 6.32,  $\text{Mg}_{0.70}\text{Ti}_{0.30}$  and  $(\text{Mg}_{0.70}\text{Ti}_{0.30})_{0.90}\text{Si}_{0.10}$  are compared with respect to electrochemical performances. The charging potential of  $(\text{Mg}_{0.70}\text{Ti}_{0.30})_{0.90}\text{Si}_{0.10}$  was improved changing from -0.8398 to -0.8211 V.

Addition of 10 at.% Si to the binary alloy decreased the total capacity from 5.02 to 2.78 wt.%. Discharging capacity was also decreased from 2.96 to 1.85 wt.%.

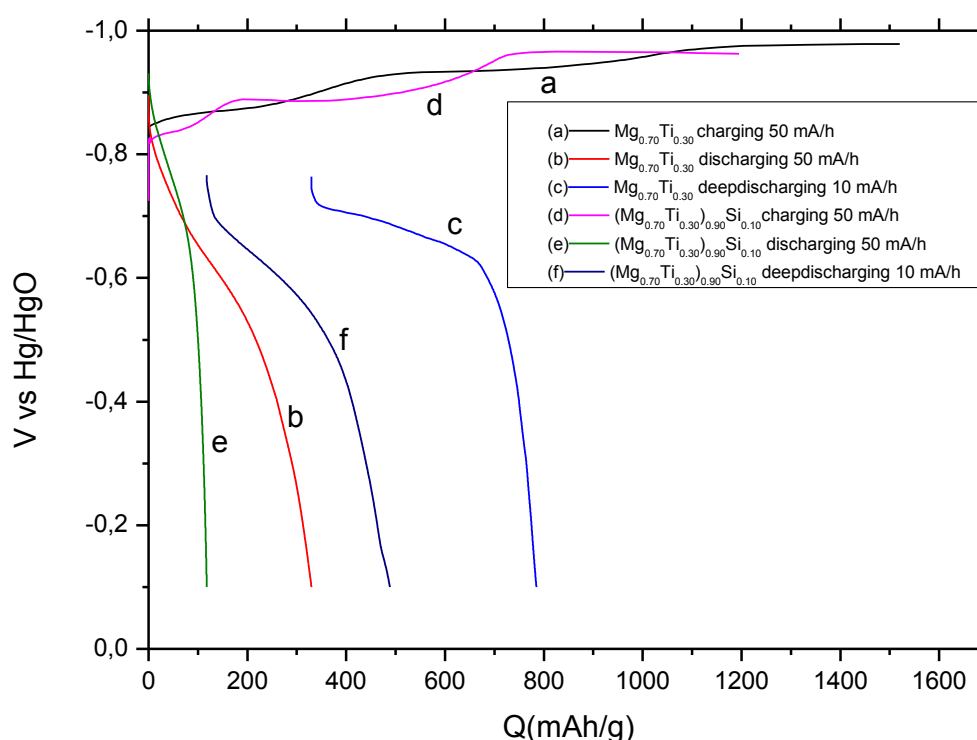


**Figure 6.32:** The electrochemical charging and discharging graphs of the  $\text{Mg}_{0.70}\text{Ti}_{0.30}$ ,  $(\text{Mg}_{0.70}\text{Ti}_{0.30})_{0.90}\text{Si}_{0.10}$  alloy.

The kinetic improvement was not observed in case of Si compared to Ni addition. The reason of this could be due to the NiHx by itself is favorable face centered cubic (FCC) structure which indeed compliments with the kinetic improvement.

As shown in **Figure 6.33**,  $(\text{Mg}_{0.70}\text{Ti}_{0.30})_{0.90}\text{Ni}_{0.10}$  is compared with  $(\text{Mg}_{0.70}\text{Ti}_{0.30})_{0.90}\text{Ni}_{0.10}$ -simultaneously. Total capacities are these alloys are approximetly the same (3.71 wt.% and 3.63 wt.%). Charging capacities of them are 3.02 and 2.96 wt.%, respectively. When the kinetic properties of the alloys are compared, any improvement has not been observed.

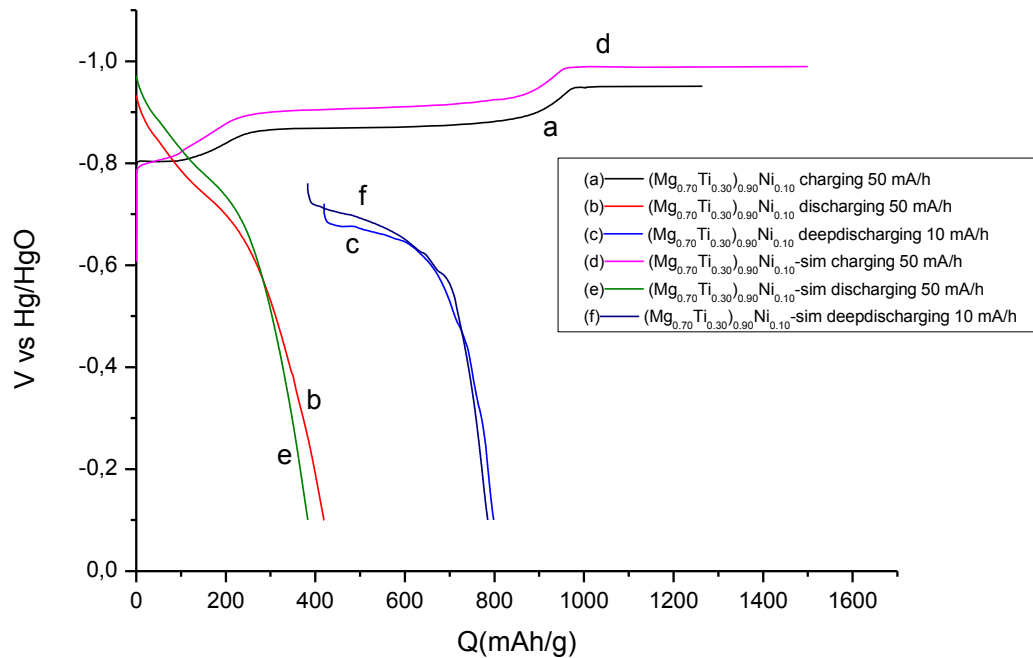


**Figure 6.33:** The electrochemical charging and discharging graphs of  $(\text{Mg}_{0.70}\text{Ti}_{0.30})_{0.90}\text{Ni}_{0.10}$ ,  $(\text{Mg}_{0.70}\text{Ti}_{0.30})_{0.90}\text{Ni}_{0.10}$  simultaneously alloy.

$(\text{Mg}_{0.70}\text{Ti}_{0.30})_{0.90}\text{Ni}_{0.10}$  and  $(\text{Mg}_{0.70}\text{Ti}_{0.30})_{0.90}\text{Si}_{0.10}$  are compared in Figure 6.34. According to this figure, the total capacity of  $(\text{Mg}_{0.70}\text{Ti}_{0.30})_{0.90}\text{Si}_{0.10}$  (2.78 wt.%) is lower than  $(\text{Mg}_{0.70}\text{Ti}_{0.30})_{0.90}\text{Ni}_{0.10}$  (3.02 wt.%). Since Si is lighter element than Ni, the total capacity is expected to be higher than Ni based ternary alloy. The experimental results (Figure 6.34) are not parallel to expectations. The discharging capacity (1.85 wt.%) of Si based alloy is lower than Ni based alloy.

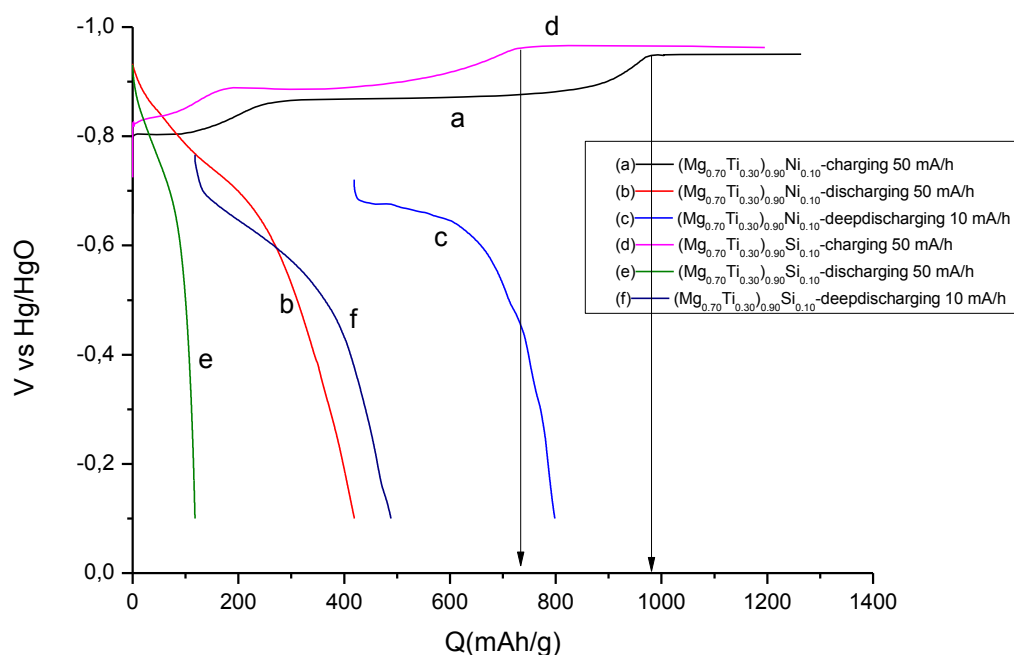


**Figure 6.34:** The electrochemical charging and discharging graphs of  $(\text{Mg}_{0.70}\text{Ti}_{0.30})_{0.90}\text{Ni}_{0.10}$  and  $(\text{Mg}_{0.70}\text{Ti}_{0.30})_{0.90}\text{Si}_{0.10}$  alloy.

$\text{Mg}_2\text{Ni}$ ,  $(\text{Mg}_2\text{Ni})_{0.90}\text{Ti}_{0.10}$  and  $(\text{Mg}_2\text{Ni})_{0.80}\text{Ti}_{0.20}$  are compared in Figure 6.35. Total capacities of them are in the order of 1.34, 2.07, and 2.31 wt.%. It is clear that the total capacity increased with Ti amount. Discharging capacities of them are 2.31, 2.066, and 2.49 wt.%, respectively. There is a remarkable improvement in kinetic properties depending on Ti addition. The high rate discharge capacity of  $(\text{Mg}_2\text{Ni})_{0.80}\text{Ti}_{0.20}$  is higher than  $\text{Mg}_2\text{Ni}$  and  $(\text{Mg}_{0.70}\text{Ti}_{0.30})_{0.90}\text{Ni}_{0.10}$ . The structural modification of the hydrided compound could be one of the reason for kinetic improvements. The Ti addition favors the formation of the fluorite structure in the resultant hydride compound. When  $\text{Mg}_2\text{Ni}$  and  $\text{Mg}_{0.70}\text{Ti}_{0.30}$  alloys are compared,  $\text{Mg}_2\text{Ni}$  compound is more stable than  $\text{Mg}_{0.70}\text{Ti}_{0.30}$  alloy. This results in an improvement in the kinetic properties of  $\text{Mg}_2\text{Ni}$ .

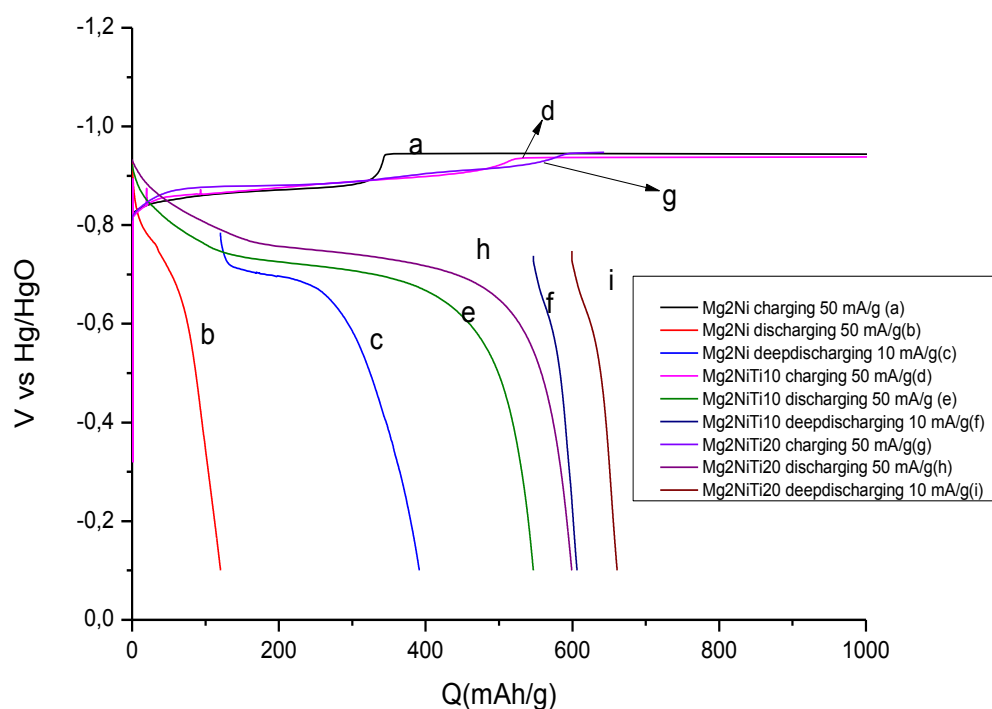


**Figure 6.35:** The electrochemical charging and discharging graphs of  $\text{Mg}_2\text{Ni}$  and  $(\text{Mg}_2\text{Ni})_{0.90}\text{Ti}_{0.10}$  and  $(\text{Mg}_2\text{Ni})_{0.80}\text{Ti}_{0.20}$  alloy.

Among the alloys produced in this study,  $(\text{Mg}_2\text{Ni})_{0.90}\text{Ti}_{0.10}$  depending on its kinetic performance, was chosen as an alloy to observe the charging and discharging performances with in three cycles (Figure 6.36). Any important difference was not observed for the first two cycles, an important decrease in discharging potential was obtained in the third cycle. The charging capacities slightly decrease depending on the cycles. Although such result seemed to be promising to get a final conclusion some other performance test for other cycles has to be performed.

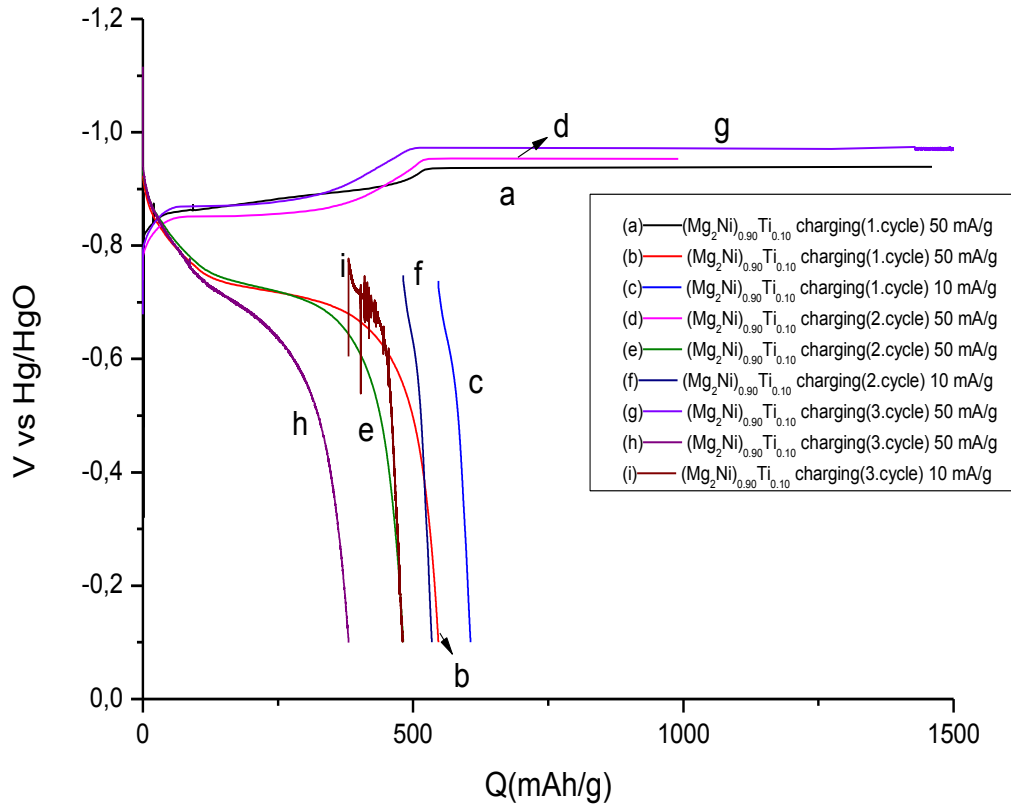


**Figure 6.36:** The electrochemical charging and discharging graph of the  $(\text{Mg}_2\text{Ni})_{0.90}\text{Ti}_{0.10}$ .

GITT was performed on  $(\text{Mg}_{0.70}\text{Ti}_{0.30})_{0.90}\text{Ni}_{0.10}$  with charging current density of 50 mA/g for one hour and continued by the resting period of 3 hours to record the equilibrium potential. The equilibrium pressure is calculated by equation (3.11). The GITT for the discharging was performed by discharging with the current density of 25 mA/g for one hour and subsequent resting period of 3 hour. The overpotential during the charging is lower compared to the discharging. This is ascribed due to the fact that discharging current is away from equilibrium.

In GITT graphs, the potential relaxes faster in the second plateau region and attains the equilibrium value faster compared to the first plateau. As shown in Figure 6.37 and Figure 6.38, the equilibrium potential values (red curve) are much lower than the charging values shown in the graph. The gap between charging and charging equilibrium curves is quite high in the first plateau. The reason of this is thought to be due to the resting time of three hours which could not be sufficient to attain the equilibrium in the first plateau. The equilibrium potential of the HER lies around -

0.93 V which corresponds to 1 bar. The equilibrium potential of the second charging plateau lies around -0.83 V which corresponds to  $10^{-4}$  bar at room temperature. The equilibrium potential of the discharging lies around -0.75 V. In the case of Si (**Figure 6.39**), the over potential is higher compared to the Ni based alloys. In the case of Si such as Ni, the improvement in the dehydrogenation potential was not observed which means that the equilibrium potential is changed.

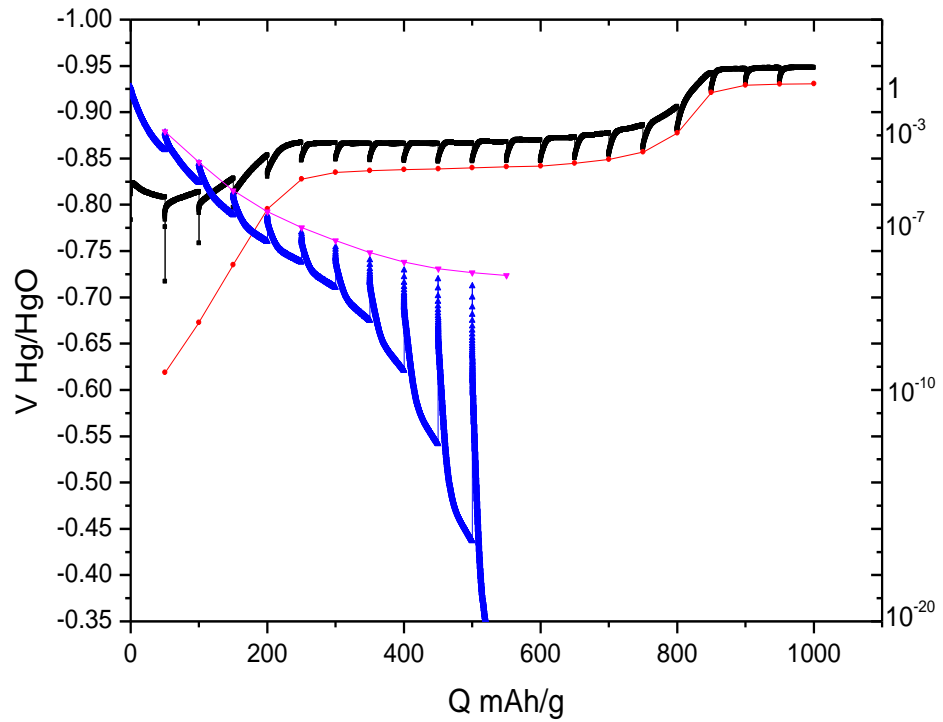


**Figure 6.37:** GITT graph of  $(\text{Mg}_{0.70}\text{Ti}_{0.30})_{0.90}\text{Ni}_{0.10}$ .

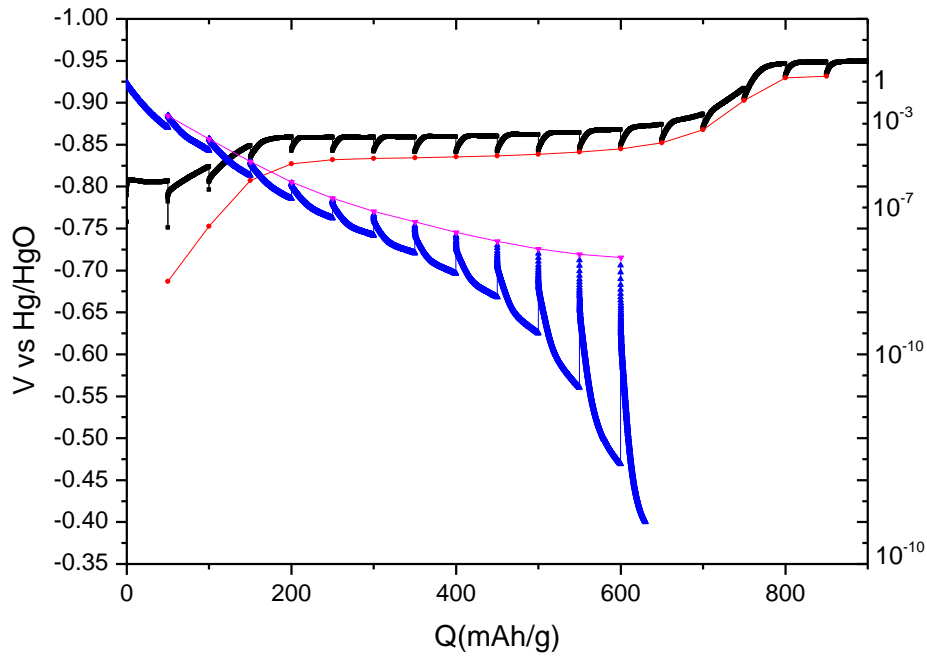


**Figure 6.38:** GITT graph of  $(\text{Mg}_{0.70}\text{Ti}_{0.30})_{0.80}\text{Ni}_{0.20}$ .

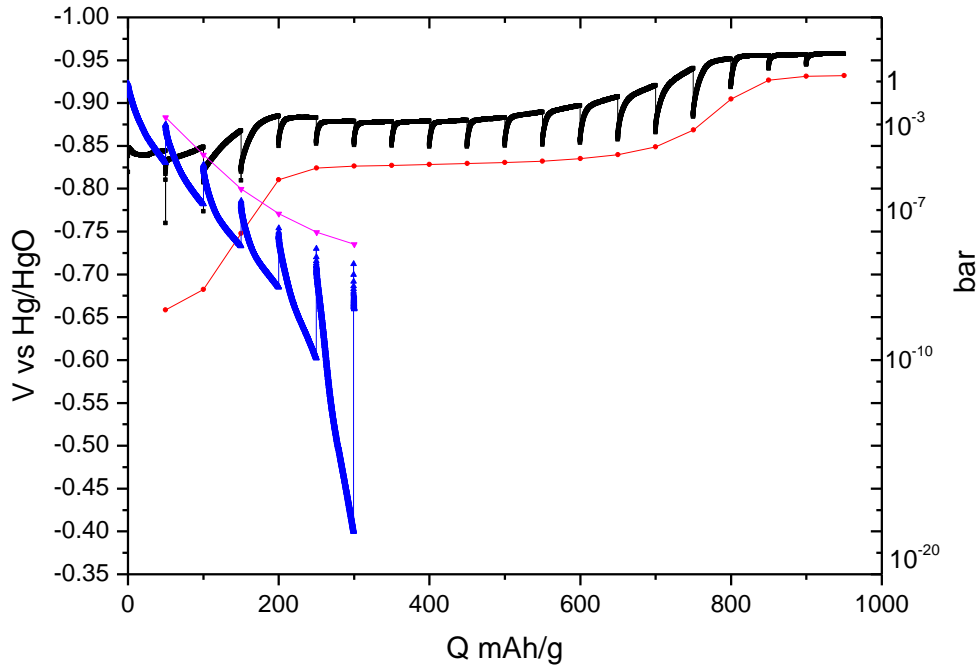


**Figure 6.39:** GITT graph of  $(\text{Mg}_{0.70}\text{Ti}_{0.30})_{0.90}\text{Si}_{0.10}$ .

Impedance measurements having the range of frequencies covered is between 50 kHz and 1 MHz are taken at the end of the resting period in GITT. Current in the experiments was applied as  $\pm 5 \text{ mV}$ . The impedance of the electrochemical system



includes the solution resistance, the double layer capacitance, charge transfer resistance and Warburg diffusion element. The solution resistance comes from the electrolyte and the solution resistance can be minimized by keeping the reference electrode near to the working electrode. In an electrolyte solution, the overall reaction during the charging and discharging are as follows:

Liquid-solid interface reaction:



Solid state reactions:



When the hydrogen is generated by electrolysis of water on the surface electrode, the hydrogen atom is absorbed on the surface and the absorbed hydrogen diffuses into the bulk metal. At the discharge process, the hydrogen transfers from the host metal lattice to the metal electrolyte interface.

The Nyquist plot consists of the semi-circle at the mid frequencies and a line at the low frequencies. The former part represents the charge transfer reaction (6.1) and the latter part represents the diffusion of the hydrogen in the bulk reaction (6.2). During the diffusion reaction the hydrogen located on the metal surface, start to diffuse into the material. This is explained by the Warburg's element. Figure 6.40, Figure 6.41 and Figure 6.42 show the impedance plots of different alloys at various stages of discharge.

The dehydrogenation processes of Mg-Ti-Ni alloys (Figure 6.40 and Figure 6.41) and Mg-Ti-Si (Figure 6.42) cover both the charge transfer at the metal electrolyte interface and diffusion of the hydrogen in the metal lattice. As it can be seen from the figures, when depth of discharge decrease the Warburg component becomes more noticable. The hydrogen concentration decreases with an increase in the depth of discharge which in turn decreases the mass transfer dependence.

The size of the semi circle in the mid frequencies depends on the charge transfer resistance of the material. As the depth of the discharge increases, the charge transfer resistance also increases. It reveals a fast charge-transfer process and slow diffusion for hydrogen in the alloy at this stage. The Mg-Ti-Si impedance plot (Figure 6.42)

shows two semi circle at lower hydrogen content (higher depth of discharge). The semicircle is less pronounced or even not observed at higher hydrogen contents.

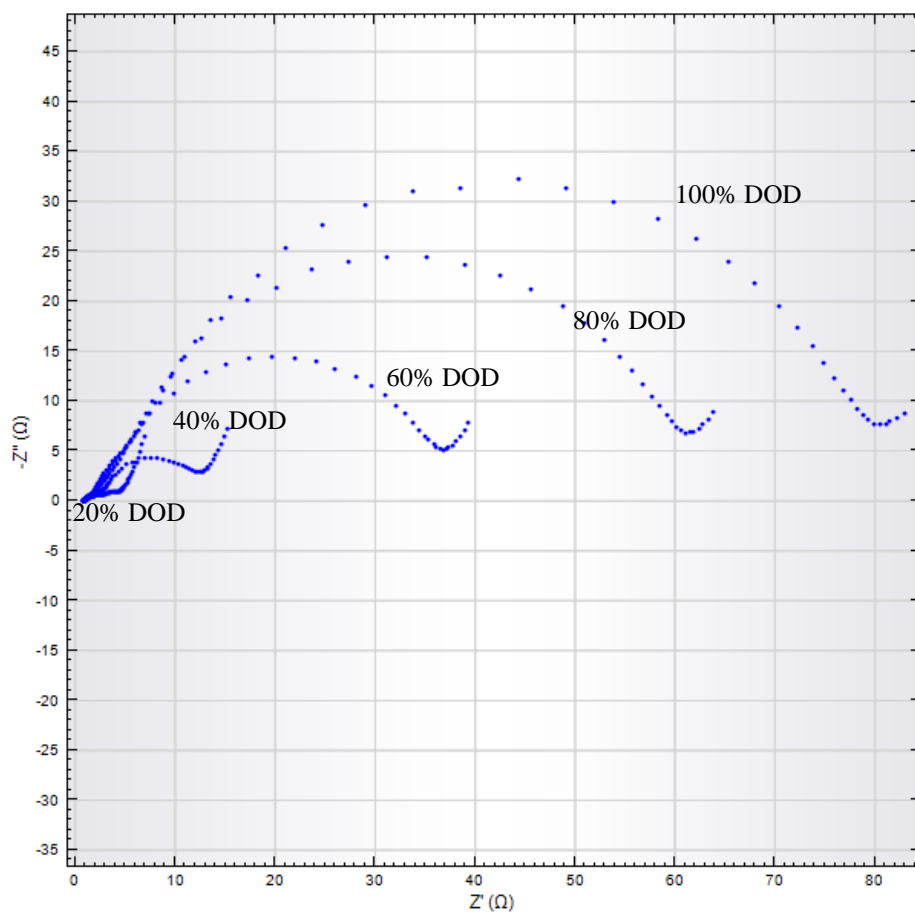


**Figure 6.40:** Impedance measurement of  $(\text{Mg}_{0.70}\text{Ti}_{0.30})_{0.90}\text{Ni}_{0.10}$ .

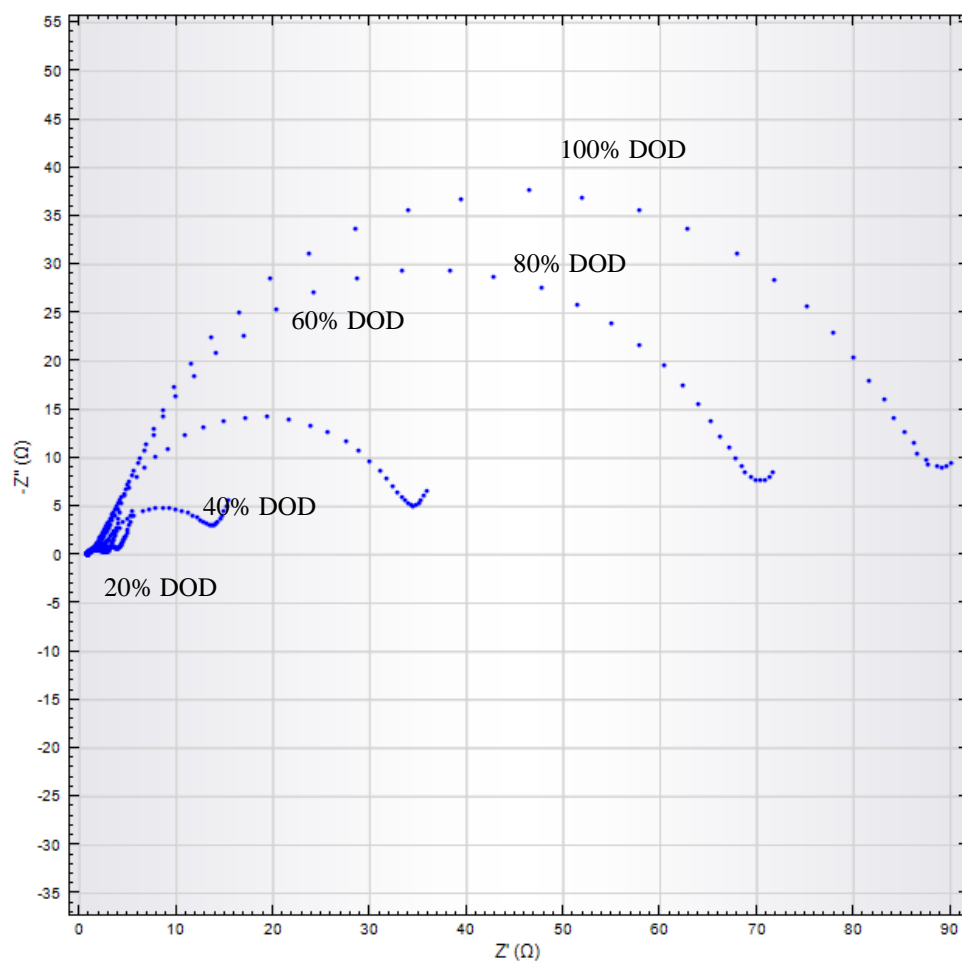


**Figure 6.41:** Impedance measurement of  $(\text{Mg}_{0.70}\text{Ti}_{0.30})_{0.80}\text{Ni}_{0.20}$ .

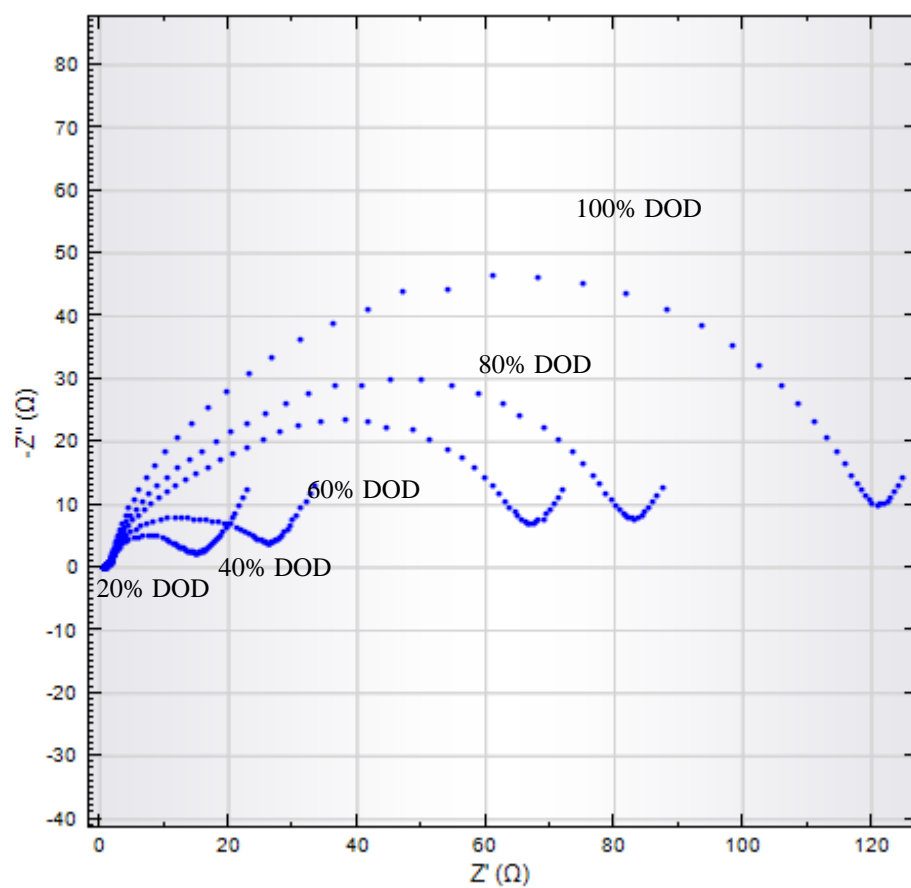


**Figure 6.42:** Impedance measurement of  $(\text{Mg}_{0.70}\text{Ti}_{0.30})_{0.90}\text{Si}_{0.10}$ .

## 7 CONCLUSIONS AND RECOMMENDATIONS FOR FUTURE RESEARCH

The main aim of this project is to prepare Mg-based alloys and obtain their performance with respect to hydrogen storage capabilities.

The ternary alloys with different compositions were successfully synthesized and contamination was not observed with XRD. Mg-Ti-Ni ternary alloy was prepared by mechanical alloy method with pre-milling of Mg-Ti alloy and adding the Ni at later stages. According to XRD patterns a shift in Mg reflection is observed for the premilled alloy. Magnesium reflections shift towards higher angle and the Titanium reflections decrease in the intensity during the milling process. The shifts were observed with increasing milling time. The shift is ascribed due to fact that Ti is having lower molar volume compared to Mg. The lattice of the Mg is getting smaller with Ti inclusion. The later addition of Ni cause a shift in unexpected direction. Since Ni has the lower molar volume comparing to Mg and Ti, the shift should be towards to lower angles. Shifting towards to lower angles means the higher lattice parameters occurred. The addition of Ni to Mg-Ti alloy improves the kinetic performance of the ternary alloy with a decrease in the capacity of it due to its higher atomic weight. The kinetic improvement could also be due to the particle size effect which was obtained by the SEM micrographs. The particle size of Mg-Ti and Mg-Ti-Ni alloys are 20-50  $\mu\text{m}$  and 10-30  $\mu\text{m}$ , respectively. Addition of Ni in 20at.% was not caused to improve the kinetic properties with respect to 10 at.% Ni addition. The efficient amount of Ni addition should be investigated with some other experiments in details. The lattice parameters of  $(\text{Mg}_{0.70}\text{Ti}_{0.30})_{0.80}\text{Ni}_{0.20}$  are similar to that of  $(\text{Mg}_{0.70}\text{Ti}_{0.30})_{0.90}\text{Ni}_{0.10}$  with ambiguity in c-axis. The reason of this needs to be explained by making further experiments in details. As a final conclusion, addition of Ni to Mg-Ti alloy improves the kinetic properties. Addition of Ni does not affect the thermodynamic properties of the alloy. Such conclusions are supported by GITT graphs.

$\text{Mg}_2\text{Ni}$ -Ti ternary alloy was prepared by mechanical alloy method with pre-milling of  $\text{Mg}_2\text{Ni}$  alloy and adding the Ti at later stages. The XRD patterns confirmed that the

alloys was performed successfully. After a given milling time Ti reflections were not observed which means the alloys occurred homogeneously. The Ti addition hardly influences the crystal structure of  $\text{Mg}_2\text{Ni}$ . Any peak shifts in the  $\text{Mg}_2\text{Ni}$  peaks were not observed depending on the milling time despite of Mg-Ti-Ni and Mg-Ti-Si alloys. The shifting in the main peaks can also be because of the changes in particle size of the alloys.  $\text{Mg}_2\text{Ni}$  based alloys have not shifted in their main peaks which have smaller particle size compared to Mg-Ti-Ni and Mg-Ti-Si alloys. The reasons of such peak shifts must be investigated in details by making some other experiments focus on this issue.

The electrochemical performance of  $\text{Mg}_2\text{Ni}$  based alloys was found to be interesting and it showed a remarkable improvement in kinetic performances. The kinetic improvements observed for these alloys could be due to the particle size (1-10  $\mu\text{m}$ ) differing from the other alloys having the higher particle sizes. The surface area calculations can also be performed to explore the electrochemical behavior of the alloys and get some other conclusions about the kinetic improvements observed.

The ternary Mg-Ti alloy with Si was also investigated in this study. The Mg-Ti-Si alloy was formed by using the premilling technique as used for the case of Ni. The Mg-Ti alloy was first prepared then the Si powder was added at the later stages after the formation of Mg-Ti binary alloy. The addition of Si shifts the Mg reflection towards the lower angle which means there is a decrease in the lattice constant with the addition of Si. All Si reflections were disappeared after 6 hours milling time which means the alloy was completed homogeneously. The electrochemical behavior of this alloy was not fulfilled the expectations since it showed lower kinetic performance compared to Mg-Ti itself. The thermodynamic properties of the alloy was also not improved which is completely different from the thin film studies of Vermulen et al. [129,130]. The  $\text{Mg}_2\text{Si}$  was synthesized and confirmed by the formation with XRD. The electrochemical behavior of the alloy was observed as poor. The alloy just reaches the HER immediately. As a final conclusion  $\text{Mg}_2\text{Si}$  itself is not a suitable material for hydrogen storage. In all cases, the theoretical capacities of the alloys were higher than experimental values, the reason of this should be explained by making some other studies in details. The relations between kinetic improvements and capacities should also be investigated.

Impedance measurements of Mg-Ti-Ni and Mg-Ti-Si were performed in this study for comparison. It was observed that when depth of discharge decrease the Warburg component becomes more noticable. To get a final conclusion some other detail studies and calculations must be performed.





## REFERENCES

- [1] F.E. Pinkerton and B.G. Wicke, *Bottling the hydrogen genie*, Ind. Phys. **2004**, 10, 20-23
- [2] B.P. statistical review of world energy, Url-1 <http://www.bp.com/statisticalreview> (March**2012**)\_publications/statistical\_energy\_review\_2007/STAGING/local\_assets/downloads/pdf/statistical\_review\_of\_world\_energy\_full\_report\_2007.pdf.
- [3] L. Schlapbach and A. Züttel, *Hydrogen-storage materials for mobile applications*, Nature (London) **2001**, 414, 353-358.
- [4] A. Züttel, A. Borgschulte and L. Schlapbach, *Hydrogen as a future energy carrier*, Wiley-VCH Verlag GmbH & Co. KGaA **2008**.
- [5] W. Doenitz, R. Schmidberger, E. Steinheil and R. Streicher, *Hydrogen production by high temperature electrolysis of water vapour*, Int. J. Hydrogen Energy **1998**, 5, 55-63
- [6] H. Gaffron and J.J. Rubin, *Fermentative and photochemical production of hydrogen in algae*, J. Gen. Physiol. **1942**, 26, 219-240.
- [7] U.S. Department of Energy, Multi-Year Research, Development and Demonstration, Plan: Planned program activities for 2003-2010,<http://www.eere.energy.gov/hydrogenandfuelcells/mypp/> (March **2012**).
- [8] R. Griessen and T. Riesterer, *Topics in Applied Physics Hydrogen in Intermetallic Compounds,Chapter 6: Heat of Formation Models*, Vol. 63 (Ed. L. Schlapbach), Springer-Verlag, Berlin, **1988**, 219-284
- [9] E. Huheey, *Inorganic Chemistry*, Harper & Row, New York **1983**.
- [10] F. Stampfer, C.E. Holley and J.F. Suttle, *The magnesium-hydrogen system*, J. Am. Chem. Soc.**1960**, 82, 3504-3508.
- [11] A. Andreasen, *PhD thesis: Hydrogen storage materials with focus on main group I-II elements*,Risø National Laboratory, Denmark, **2005**.
- [12] K.H.J. Buschow, P.C.P. Bouten and A.R. Miedema, *Hydrides formed from intermetalliccompounds of two transition metals: a special class of ternary alloys*, Rep. Prog. Phys. **1982**, 45,937-1039.
- [13] C.M. Stander, *Kinetics of the formation of magnesium hydride from magnesium and hydrogen*,Phys. Chem. Neue Folge **1977**, 104, 229-238.
- [14] A. Krozer and B. Kasemo, *Unusual kinetics due to interface hydride formation in the hydriding of Pd/Mg sandwich layers*, J. Vac. Sci. Technol. A **1987**, 5, 1003-1005.
- [15] J. Rydén, B. Hjörvarsson, T. Ericsson, E. Karlsson, A. Krozer and B. Kasemo, *Unusual kinetics of hydride formation in Mg-Pd sandwiches, studied by hydrogen*

*profiling and quartz crystal microbalance measurements*, J. Less-common Met. **1989**, 152, 295-309.

[16] V.P. Zhdanov, A. Krozer and B. Kasemo, *Kinetics of first-order phase transitions initiated by diffusion of particles from the surface into the bulk*, Phys. Rev. B **1993**, 47, 11044-11048.

[17] K.B. Gerasimov and E.Y. Ivanov, *The mechanism and kinetics of formation and decomposition of magnesium hydride*, Mater. Lett. **1985**, 3, 497-499

[18] Z. Luz, J. Genossar and P.S. Rudman, *Identification of the diffusing atom in MgH<sub>2</sub>*, J. Less-common Met. **1980**, 73, 113-118.

[19] J. Töpler, H. Buchner and H. Säuferer, *Measurements of the diffusion of hydrogen atoms in magnesium and Mg<sub>2</sub>Ni by neutron scattering* J. Less-common Met. **1982**, 88, 397-404.

[20] P. Spatz, H.A. Aebischer, A. Krozer and L. Schlapbach, *The diffusion of H in Mg and the nucleation and growth of MgH<sub>2</sub> in thin films*, Z. Phys. Chem. **1993**, 181, 393-397.

[21] B. Vigeholm, K. Jensen, B. Larsen and A.S. Pedersen, *Elements of hydride formation mechanisms in nearly spherical magnesium powder particles*, J. Less-common Met. **1987**, 131, 133-141.

[22] M. Stioui, A. Grayevski, A. Resnik, D. Shaltiel and N. Kaplan, *Macroscopic kinetics of hydrogen in magnesium-rich compounds*, J. Less-common Met. **1986**, 123, 9-24.

[23] J.M. Tarascon, M. Armand, *Issues and challenges facing rechargeable Lithium batteries*, Nature, **414**, 359 (2001)

[24] J.N. Huiberts, R. Griessen, J.H. Rector, R.J. Wijngaarden, J.P. Dekker, D.G. de Groot and N.J. Koeman, *Yttrium and lanthanum hydride films with switchable optical properties*, Nature **1996**, 380, 231-234.

[25] C.G. Granqvist, *Handbook of Inorganic Electrochromic Materials*, Amsterdam, Elsevier **1995**.

[26] P.H.L. Notten, M. Kremers M and R. Griessen, *Optical switching of Y-hydride thin film electrodes: a remarkable electrochromic phenomenon*, J. Electrochem. Soc. **1996**, 143, 3348-3353.

[27] P. van der Sluis, M. Ouwerkerk and P.A. Duine, *Optical switches based on magnesium lanthanide alloy hydrides*, Appl. Phys. Lett. **1997**, 70, 3356-3358.

[28] T.J. Richardson, R.D. Armitage, J.L. Slack and M.D. Rubin, *Alternative materials for electrochromic mirror devices*, poster presentation at the Fourth International Meeting on Electrochromism (IME-4), August 21-23 **2000**, Uppsala, Sweden.

[29] T.J. Richardson, J.L. Slack, R.D. Armitage, R. Kostecki, B. Farangis and M.D. Rubin, *Switchable mirrors based on nickel-magnesium films*, Appl. Phys. Lett. **2001**, 78, 3047-3049.

[30] T.J. Richardson, J.L. Slack, B. Farangis and M.D. Rubin, *Mixed metal films with switchable optical properties*, Appl. Phys. Lett. **2002**, 80, 1349-1351.

- [31] R.A.H. Niessen and P.H.L. Notten, *Electrochemical hydrogen storage characteristics of thin film MgX (X=Sc,Ti,V,Cr) compounds*, Electrochem. Solid-State Lett. **2005**, 8, A534-A538.
- [32] M. Slaman, B. Dam, M. Pasturel, D.M. Borsa, H. Schreuders, J.H. Rector and R. Griessen, *Fiberoptic hydrogen detectors containing Mg-based metal hydrides*, Sens. Actuators B **2006**, 123,538-545.
- [33] D.M. Borsa, A. Baldi, M. Pasturel, H. Schreuders, B. Dam, R. Griessen, P. Vermeulen and P.H.L.Notten, *Mg-Ti-H thin films for smart solar collectors*, Appl. Phys. Lett. **2006**, 88, 241910/1-3.
- [34] S. Bao, K. Tajima, Y. Yamada, M. Okada and K. Yoshimura, *Color-neutral switchable mirrors based on magnesium-titanium thin films*, Appl. Phys. A **2007**, 87, 621-624.
- [35] S. Bao, K. Tajima, Y. Yamada, M. Okada and K. Yoshimura, *Magnesium-titanium alloy thin-film switchable mirrors*, Solar Energy Materials & Solar Cells **2008**, 92, 224-227.
- [36] A. Baldi, D.M. Borsa, H. Schreuders, J.H. Rector, T. Atmakidis, M. Bakker, H.A. Zondag, W.G.J. van Helden, B. Dam and R. Griessen, *Mg-Ti-H thin films as switchable solar absorbers*, Int. J. Hydrogen Energy **2008**, 33, 3188-3192.
- [37] JS. Benjamin, Mechanical Alloying, Scientific American, 1976, 234, 40-8.
- [38] Suryanarayana C., Nanocrystalline Materials, International Materials Reviews, 1995, 40, 41-64.
- [39] Benjamin JS., Fundamentals of Mechanical Alloying, Metal Powder Rep, 1990, 45, 122-7.
- [40] Gilman PS., Benjamin JS., Mechanical Alloying, Annual Review Of Materials Science, 1983, 13, 279-300.
- [41] Lee PY, Koch CC., Formation Of Amorphous Ni-Zr Alloy Powder By Mechanical Alloying Of Intermetallic Powder Mixtures And Mixtures Of Nickel Or Zirconium With Intermetallics, Journal Of Materials Science, 1988, 23, 2837-45.
- [42] Davis RM, Koch CC., Mechanical Alloying of Brittle Components- Silicon and Germanium, Scripta Metallurgica, 1987, 21, 305-10.
- [43] Davis RM, McDermott B, Koch CC., Mechanical Alloying of Brittle Materials, Metallurgical Transactions A-Physical Metallurgy And Materials Science, 1988, A19, 2867-74.
- [44] Lee PY, Koch CC., Formation of Amorphous Ni-Zr Alloys by Mechanical Alloying of Mixtures of Intermetallic Compounds Ni<sub>11</sub>Zr<sub>9</sub> and NiZr<sub>2</sub>, Applied Physics Letters, 1987, 50, 1578-80.
- [45] Harris CC., Effect of Time in Batch Grinding, Powder Technology, 1970, 4, 57.
- [46] Okada K, Kikuchi S, Ban T, Otsuka N., Difference of Mechanochemical Factors for Al<sub>2</sub>O<sub>3</sub> Powders Upon Dry and Wet Grinding, Journal of Materials Science Letters, 1992, 11, 862-4.
- [47] Nicoara G, Fratiloiu D, Nogues M, Dormann JL, Vasiliu F., Ni-Zn Ferrite Nanoparticles Prepared by Ball Milling, Materials Science, 1997, 235- 238, 145-50.

- [48] Bellosi A, Montverde F, Botti S, Martelli S., Development and Characterization of Nanophase Si<sub>3</sub>N<sub>4</sub>-based Ceramics, Materials Science Forum, 1997, 235-238, 55-60.
- [49] Dolgin BP, Vanek MA, McGory T, Ham DJ., Mechanical Alloying of Ni, Co, and Fe with Ti- Formation of an Amorphous Phase, Journal of Non-Crystalline Solids, 1986, 87, 281-9.
- [50] Blaskov V, Radev DD, Klissurski D, Yordanov ND., Behavior of Cu(II) Hydroxide During Mechanical Treatment, Journal of Alloys and Compounds, 1994, 206, 267-70.
- [51] Kerr I., Experience With 5FU Plus L-Leucovorin, Metal Powder Rep 1993, 48, 36-8.
- [52] Di LM, Bakker H., Phase-Transformation of the Copmpound V<sub>3</sub>Ga Introduced by Mechanical Grinding, Journal of Physics-Condensed Matter, 1991, 3, 3427-32.
- [53] Suryanarayana C, Ivanov E, Noufi R, Contreras MA, Moore JJ., Phase Selection in a Mechanically Alloyed Cu-In-Ga-Se Powder Mixture, Journal of Materials Research, 1999, 14, 377-83.
- [54] Chu B-L, Chen C-C, Perng T-P., Amorphization of Ti<sub>1</sub>-XMNX Binary Alloys by Mechanical Alloying, Metallurgical Transactions A-Physical Metallurgy and Materials Science, 1992, A23, 2105-10.
- [55] Tokumitsu K., Synthesis of metastable Fe<sub>3</sub>C, Co<sub>3</sub>C and Ni<sub>3</sub>C by mechanical alloying method, Materials Science Forum, 1997, 235-238, 127-32.
- [56] Yen BK, Aizawa T, Kihara, Synthesis And Formation Mechanisms Of Molybdenum Silicides By Mechanical Alloying, Materials Science And Engineering A-Structural Materials Properties Microstructure And Processing, 1996, A 220, 8-14.
- [57] Yen BK, Aizawa T, Kihara J., Mechanical Alloying Behavior In Molybdenum-Silicon System, Material Science Forum 1997;235-238:157-62.
- [58] El-Eskandarany MS., Mechanical Solid State Mixing For Synthesizing Of SiCp/Al Nanocomposites, Journal of Alloys and Compounds, 1994, 203, 117-26.
- [59] El-Eskandarany MS, Sumiyama K, Aoki K, Masumoto T, Suzuki K., Cyclic Crystalline-Amorphous Transformations By Mechanical Alloying, Journal of Materials Research, 1994, 9, 2891-8.
- [60] Tonejc A, Duzevic D, Tonejc AM., Effects Of Ball Milling On Pure Antimony, On Ga-Sb Alloy And On Ga+Sb Powder Mixture - Oxidation, Glass-Formation And Crystallization, Materials Science And Engineering A-Structural Materials Properties Microstructure And Processing, 1991, A134, 1372-5.
- [61] Ohtani T, Maruyama K, Ohshima K., Synthesis Of Copper, Silver, And Samarium Chalcogenides By Mechanical Alloying, Materials Research Bulletin, 1997, 32, 343-50.
- [62] El-Eskandarany MS., Cyclic Solid-State Transformations During Ball Milling Of Aluminum Zirconium Powder And The Effect Of Milling Speed, Metallurgical And Materials Transactions A-Physical Metallurgy And Materials Science, 1996, A27, 2374-82.

- [63] Abe O, Suzuki Y., Mechanochemically assisted preparation of BaTiO<sub>3</sub> powder, Materials Science Forum, 1996, 225-227, 563-8.
- [64] Fukunaga T, Nakamura K, Suzuki K, Mizutani U., Amorphization Of Immiscible Cu-Ta System By Mechanical Alloying And Its Structure Observation, Journal Of Non-Crystalline Solids, 1990, 117-118, 700-3.
- [65] Fukunaga T, Mori M, Inou K, Mizutani U., Amorphization In An Immiscible Cu-V System By Mechanical Alloying And Its Structure Observed By Neutron-Diffraction, Materials Science And Engineering A-Structural Materials Properties Microstructure And Processing, 1991, A134, 863-6.
- [66] Lee CH, Fukunaga T, Mizutani U., Temperature-Dependence Of Mechanical Alloying And Grinding In Ni-Zr, Cu-Ta And Fe-B Alloy Systems, Materials Science And Engineering A-Structural Materials Properties Microstructure And Processing, 1991, A134, 1334-7.
- [67] Lee CH, Mori M, Fukunaga T, Sakurai K, Mizutani U., Structural Evidence For The Amorphization Of Mechanically Alloyed Cu-Ta Powders Studied By Neutron-Diffraction And Exafs, Materials Science Forum 1992;88-90:399-406.
- [68] Sakurai K, Lee CH, Kuroda N, Fukunaga T, Mizutani U., Nitrogen Effect In Mechanical Alloying Of Immiscible Cu-V - Extended X-Ray-Absorption Fine-Structure Study, Journal of Applied Physics, 1994;75:7752-5.
- [69] Harringa JL, Cook BA, Beaudry BJ., Effects Of Vial Shape On The Rate Of Mechanical Alloying In Si<sub>80</sub>Ge<sub>20</sub>, Journal of Materials Science 1992;27:801-4.
- [70] Kaloshkin SD, Tomlin IA, Andrianov GA, Baldokhin UV, Shelekhov EV., Phase Transformations And Hyperfine Interactions In Mechanically Alloyed Fe-Cu Solid Solutions, Materials Science Forum 1997;235-238:565-70.
- [71] Kuhrt C, Schropf H, Schultz L, Arzt E., Mechanical Alloying For Structural Applications, Materials Park, 1993, 269-73.
- [72] Suryanarayana C., Does A Disordered Gamma-TiAl Phase Exist In Mechanically Alloyed Ti-Al Powders, Intermetallics 1995;3:153-60.
- [73] Chu B-L, Chen C-C, Perng T-P., Amorphization Of Ti<sub>1</sub>-XMX Binary-Alloys By Mechanical Alloying, Metallurgical Transactions A-Physical Metallurgy And Materials Science, 1992;A23:2105-10.
- [74] Larson JM, Luhman TS, Merrick HF., Manufacture of Superconducting Materials, Materials Park, 1977, 155-63.
- [75] Biswas A, Dey GK, Haq AJ, Bose DK, Banerjee S., A study of solid-state amorphization in Zr-30 at% Al by mechanical attrition, J Mater Res 1996;11:599-607.
- [76] Katamura J, Yamamoto T, Qi X, Sakuma T., Mechanical alloying in the system ZrO<sub>2</sub>-ZrN, Journal of Materials Science Letters 1996;15:36-7.
- [77] Ohtani T, Maruyama K, Ohshima K., Synthesis of copper, silver, and samarium chalcogenides by mechanical alloying, Mater Res Bull 1997;32:343-50.
- [78] El-Eskandarany MS., Cyclic Solid-State Transformations During Ball Milling Of Aluminum Zirconium Powder And The Effect Of Milling Speed, Metallurgical And

Materials Transactions A-Physical Metallurgy And Materials Science, 1996, A27, 2374-82.

[79]Yen BK, Aizawa T, Kihara J., Synthesis and formation mechanisms of molybdenum silicides by mechanical alloying, Mater Sci and Engng 1996;A 220:8-14.

[80]Yen BK, Aizawa T, Kihara J., Mechanical alloying behavior in molybdenum-silicon system, Mater Sci Forum 1997;235- 38:157-62.

[81]El-Eskandarany MS, Sumiyama K, Aoki K, Masumoto T, Suzuki K., Cyclic Crystalline-Amorphous Transformations By Mechanical Alloying, Journal of Materials Research, 1994, 9, 2891-8.

[82]Abe O, Suzuki Y., Mechanochemically assisted preparation of BaTiO<sub>3</sub> powder, Mater Sci Forum 1996;225-227:563-8.

[83]Sakurai K, Lee CH, Kuroda N, Fukunaga T, Mizutani U., Nitrogen Effect In Mechanical Alloying Of Immiscible Cu-V - Extended X-Ray-Absorption Fine-Structure Study, J Appl Phys 1994;75:7752-5.

[84] Lai MO, Lu L., Mechanical alloying, Kluwer Academic Publishers, 1998.

[85]Guo W, Iasonna A, Magini M, Martelli S, Padella F., Synthesis Of Amorphous And Metastable Ti<sub>40</sub>Al<sub>60</sub> Alloys By Mechanical Alloying Of Elemental Powders, Journal of Materials Science, 1994;29:2436-44.

[86]Gerasimov KB, Gusev AA, Ivanov EY, Boldyrev VV., Tribochemical equilibrium in mechanical alloying of metals, J Mater Sci 1991;26:2495-500.

[87]Liu L, Casadio S, Magini M, Nannetti CA, Qin Y, Zheng K., Solid state reactions of V<sub>75</sub>Si<sub>25</sub> driven by mechanical alloying, Mater Sci Forum 1997;235-238:163-8.

[88]Atzmon M., Insitu Thermal Observation Of Explosive Compound-Formation Reaction During Mechanical Alloying, Phys Rev Lett 1990;64:487-90.

[89] Gavrilov D, Vinogradov O, Shaw WJD., Process of Inter. Conf. on Composite Materials, Woodhead Publishing, 1995, 3, 11.

[90] Takacs L., Processing and properties of nanocrystalline materials, TMS, 1996, 453-64.

[91]Chin Z-H, Perng T-P., : Instant formation of TiN by reactive milling of Ti in nitrogen, Mater Sci Forum 1997;235-238:121-6.

[92] Kis-Varga, Beke DL., Mechanical alloying and magnetic properties of Fe<sub>90</sub>Sb<sub>10</sub> and Fe<sub>15</sub>Sb<sub>85</sub> systems, Materials Science Forum 1996;225-227:465-70.

[93] Suryanarayana C, Chen GH, Froes FH., Milling Maps For Phase Identification During Mechanical Alloying, Scripta Metall Mater 1992;26:1727-32.

[94] Gerasimov KB, Gusev AA, Ivanov EY, Boldyrev VV., Tribochemical equilibrium in mechanical alloying of metals, Journal of Materials Science, 1991;26:2495-500.

[95] Goodwin PS, Mukhopadhyay DK, Suryanarayana C, Froes FH, Ward-Close CM., Titanium '95, London: Institute of Materials, 1996, 3, 2626-33.

- [96] Miki M, Yamasaki T, Ogino Y., Preparation Of Nanocrystalline NbN And (Nb, Al)N Powders By Mechanical Alloying Under Nitrogen Atmosphere, *Mater Trans Japan Inst Metals* 1992;33:839-44.
- [97] Calka A, Williams JS., Synthesis Of Silicon-Nitride By Mechanical Alloying, *Mater Sci Forum* 1992;88-90:787-94.
- [98] Chen Y, Williams JS., Formation, structure and stability of iron nitrides made by reactive ball milling, *Mater Sci Forum* 1996;225-227:881-8.
- [99] Ogino Y, Yamasaki T, Maruyama S, Sakai R., Nonequilibrium Phases Formed By Mechanical Alloying Of Cr-Cu Alloys, *J Non-Cryst Solids* 1990;117/118:737-40.
- [100] Lee PY, Koch CC., The Formation And Thermal-Stability Of Amorphous Ni-Nb Alloy Powder Synthesized By Mechanical Alloying, *J Non-Cryst Solids* 1987;94:88-100.
- [101] Suryanarayana, C.; Mechanical alloying and milling, *Progress in Materials Science* 46 (2001) 1-184
- [102] Frazier WE, Koczak MJ., Mechanical And Thermal-Stability Of Powder-Metallurgy Aluminum Titanium-Alloys, *Scripta Metall* 1987;21:129-34.
- [103] Gaffet E, Harmelin M, Faudot F., Far-From-Equilibrium Phase-Transition Induced By Mechanical Alloying In The Cu-Fe System, *J Alloys and Compounds* 1993;194:23-30.
- [104] Enayati MH, Chang ITH, Schumacher P, Cantor B., Mechanical alloying of Ni-Nb alloys, *Mater Sci Forum* 1997;235-238:85-90.
- [105] Ivison PK, Soletta I, Cowlam N, Cocco G, Enzo S, Battezzati L., The Effect Of Absorbed Hydrogen On The Amorphization Of CuTi Alloys, *J Phys C: Condens Matter* 1992;4:5239-48.
- [106] Lee W, Kwun SI., The effects of process control agents on mechanical alloying mechanisms in the Ti-Al system, *J Alloys and Compounds*, 1996;240:193-9.
- [107] Lai MO, Lu L., Mechanical alloying, Kluwer Academic Publishers, 1998.
- [108] Weber JH., Solid state powder processing, Warrendale, TMS, 1990, 227-39.
- [109] Hong LB, Bansal C, Fultz B., Phases And Phase Stabilities Of Fe(3)X Alloys (X=Al, As, Ge, In, Sb, Si, Sn, Zn) Prepared By Mechanical Alloying, *Nanostructured Mater* 1994; 4:949-56.
- [110] Qin Y, Chen L, Shen H., In-Situ X-Ray Diffraction Examination Of Nanocrystalline Ag<sub>37</sub>Cu<sub>63</sub> Powders Synthesized By Mechanical Alloying, *J Alloys and Compounds* 1997;256:230-3.
- [111] Klassen T, Herr U, Averbach RS., Ball Milling Of Systems With Positive Heat Of Mixing: Effect Of Temperature In Ag-Cu, *Acta Mater* 1997;45:2921-30.
- [112] Fu Z, Johnson WL., Nanophase Zr-Al Solid-Solutions By Mechanical Alloying At Elevated-Temperatures, *Nanostructured Mater* 1993;3:175-80.
- [113] Mishurda JC, University of Idaho, Moscow, ID, unpublished results, 1993.

- [114] K. Machida, M. Enyo, G. Adachi, J. Shiokawa, The hydrogen electrode reaction characteristics of thin film electrodes of Ni-based hydrogen storage alloys, *Electrochimica Acta*, **29**, 807 (1984).
- [115] R. Griessen, T. Riesteter, Topics in Applied Physics-Hydrogen in intermetallic compounds I, Springer, Berlin, Chapter 6 (1988).
- [116] P.W. Atkins, Physical Chemistry, Oxford University Press, Oxford, 258, 1998
- [117] M. Pourbaix, Atlas of electrochemical equilibria in aqueous solutions, 2nd ed. (National Association of Corrosion Engineers, Houston, 1974) p. 425
- [118] M. Pourbaix, Atlas of electrochemical equilibria in aqueous solutions, 2nd ed. (National Association of Corrosion Engineers, Houston, 1974) p. 97
- [119] J.R. MacDonald, Impedance Spectroscopy, John Wiley & Sons NY (1987)
- [120] Reilly, J. J.; Wiswall, R. H. Reaction of hydrogen with alloys of magnesium and nickel and the formation of  $\text{Mg}_2\text{NiH}_4$ . *Inorg. Chem.* **1968**, 7(11), 2254-2256.
- [121] Janot, R.; Aymard, L.; Rougier, A.; Nazri, G.; Tarascon, J. Enhanced hydrogen sorption capacities and kinetics of  $\text{Mg}_2\text{Ni}$  alloys by ball-milling with carbon and Pd coating. *J. Mater. Res.* **2003**, 18(08), 1749-1752.
- [122] Zhang, S. G.; Hara, Y.; Suda, S.; Morikawa, T.; Inoue, H.; Iwakura, C. Physicochemical and electrochemical hydriding-dehydriding characteristics of amorphous  $\text{MgNi}_x$  ( $x = 1.0, 1.5, 2.0$ ) alloys prepared by mechanical alloying. *J. Solid State Electr.* **2001**, 5(1), 23-28.
- [123] Niessen, R. A. H.; Notten, P. H. L. Hydrogen storage in thin film magnesium-scandium alloys. *J Alloy Compd.* **2005**, 404-406, 457-460.
- [124] Kalisvaart, W. P.; Niessen, R. A. H.; Notten, P. H. L. Electrochemical hydrogen storage in MgSc alloys: A comparative study between thin films and bulk materials. *J Alloy Compd.* **2006**, 417(1-2), 280-291.
- [125] Latroche, M.; Kalisvaart, P.; Notten, P.H.L. Crystal structure of  $\text{Mg}_{0.65}\text{Sc}_{0.35}\text{D}_x$  deuterides studied by X-ray and neutron powder diffraction. *J Solid State Chem.* **2006**, 179(10), 3024-3032.
- [126] Kalisvaart, W. P.; Latroche, M.; Cuevas, F.; Notten, P. H. L. *In situ* neutron diffraction study on Pd-doped  $\text{Mg}_{0.65}\text{Sc}_{0.35}$  electrode material. *J Solid State Chem.* **2008**, 181(5), 1141-1148.
- [127] Conradi, M. S.; Mendenhall, M. P.; Ivancic, T. M.; Carl, E. A.; Browning, C. D.; Notten, P. H. L.; Kalisvaart, W. P. NMR to determine rates of motion and structures in metal-hydrides. *J. Alloy Compd.* **2007**, 446-447, 499-503.
- [128] Pauw, B. R.; Kalisvaart, W. P.; Tao, S. X.; Koper, M. T. M.; Jansen, A. P. J.; Notten, P. H. L. Cubic  $\text{MgH}_2$  stabilized by alloying with transition metals: A density functional theory study. *Acta Mater.* **2008**, 56(13), 2948-2954.
- [129] Vermeulen, P.; Niessen, R. A. H.; Notten, P. H. L. Hydrogen storage in metastable  $\text{Mg}_y\text{Ti}_{(1-y)}$  thin films. *Electrochem. Commun.* **2006**, 8(1), 27-32.
- [130] Vermeulen, P.; Wondergem, H. J.; Graat, P. C. J.; Borsa, D. M.; Schreuders, H.; Dam, B.; Griessen, R. In situ electrochemical XRD study of (de)hydrogenation of  $\text{Mg}_y\text{Ti}_{(1-y)}$  thin films. *J Mater Chem.* **2008**, 18(31), 3680-3687.



- [131] Rousselot, S.; Bichat, M. P.; Guay, D.; Roué, L. Structure and electrochemical behaviour of metastable  $\text{Mg}_{50}\text{Ti}_{50}$  alloy prepared by ball milling. *J. Power Sources*. **2008**, 175(1), 621-624.
- [132] Kalisvaart, W. P.; Notten, P. H. L. Mechanical alloying and electrochemical hydrogen storage of Mg-based systems. *J. Mater. Res.* **2011**, 23(08), 2179-2187.
- [133] Kalisvaart, W. P.; Wondergem, H. J.; Bakker, F.; Notten, P. H. L. Mg–Ti based materials for electrochemical hydrogen storage. *J. Mater. Res.* **2011**, 22(06), 1640-1649.
- [134] Kyoi, D. A new ternary magnesium-titanium hydride  $\text{Mg}_7\text{TiH}_x$  with hydrogen desorption properties better than both binary magnesium and titanium hydrides. *J Alloy Compd.* **2004**, 372(1-2), 213-217.
- [135] de Boer, F. R.; Boom, R.; Mattens, W. C. M.; Miedema, A. R.; Niessen, A. K. *Cohesion in Metals*. North-Holland, Amsterdam, **1988**, 127.
- [136] Liang, G.; Schulz, R. Synthesis of Mg-Ti alloy by mechanical alloying. *J. Mater. Sci.* **2003**, 8, 1179-1184.
- [137] Srinivasan, S.; Magusin, P. C. M. M.; Kalisvaart, W. P.; Notten, P. H. L.; Cuevas, F.; Latroche, M.; van Santen, R. A. Nanostructures of  $\text{Mg}_{0.65}\text{Ti}_{0.35}\text{D}_x$  studied with x-ray diffraction, neutron diffraction, and magic-angle-spinning  $^2\text{H}$  NMR spectroscopy. *Phys. Rev. B*. **2010**, 81(5), 1-10.
- [138] Miedema, A. Cohesion in Metals – fundamentals of a Semi-empirical model. *Physica B&C*. **1980**, 100, 1-28.
- [139] Miedema, A. R. The electronegativity parameter for transition metals: Heat of formation and charge transfer of alloys. *J. Less-Common Met.* **1973**, 32, 117- 136.
- [140] Vermeulen, P.; van Thiel, E. F. M. J.; Notten, P. H. L. Ternary  $\text{MgTiX}$ -alloys: a promising route towards low-temperature, high-capacity, hydrogen-storage materials. *Chem. Eur. J.* **2007**, 13(35), 9892-9898.
- [141] R.A.H. Niessen, P.H.L. Notten, Reference electrode induced surface poisoning of thin film electrodes, *J. Electrochem. Soc.*, **152**, A2051 (2005)
- [142] Garcia, J.; Nunez, M.; Munoz, B.; Synthesis of the  $\text{Mg}_2\text{Ni}$  Alloy prepared by Mechanical Alloying Using a High Energy Ball Mill. *J. Mex. Chem. Soc.*, 2010, 54(1), 46-50.
- [143] Brett, C.; Dias, L.; Trindade, B.; Fischer, R.; Mies, S.; Characterisation by EIS of ternary Mg alloys synthesized by mechanical alloying. *Electrochimica Acta* 51.2005, 51(2006), 1752-1760.
- [144] Munoz-Palos, J.; Cristina, M.; Adeva, P.; Synthesis of  $\text{Mg}_2\text{Si}$  powder by mechanical alloying and its consolidation. *Materials Transactions, JIM*, Vol.37, No.10 (1996), pp 1602-1606.



## **CURRICULUM VITAE**

**Merve ILIKSU**

merve\_iliksu@yahoo.com.tr

### **PERSONAL INFORMATION:**

Nationality: Turkish Citizen

Place of birth/ Date of birth: Istanbul / 15.09.1988

### **EDUCATIONAL BACKGROUND:**

2011-2012 Technische Universiteit Eindhoven, Master degree, exchange student, Mg based hydrogen storage materials project

2010-2011 Istanbul Technical University, Chemical Engineering, Master degree

2005-2010 Kocaeli University, Chemical Engineering

2002-2005 Haydarpasa Anatolian High School

### **INTERNSHIPS:**

2009 Bilim Pharmaceuticals, Bachelor project, Cephalosporin production

2009 Mustafa Nevzat Pharmaceuticals, Bachelor project, Cephalosporin production

2008 InterkordSA Mühlhausen/Thüringen- GmbH in Germany, R&D internship. Humidity effects on adhesion

2007 Pfizer Pharmaceuticals Ltd. Sti. Istanbul-Turkey, Laboratory internship, Solubility of the pills in the stomach and bowel medium

2007 KordSA Global Industrial Yarn and Tire Cord Industry and Trade Co., Ltd. Kocaeli - Turkey, R & D internship, Adhesion test methods